Implantable Electrode Structures and their RF Effects in MRI Machines

A thesis by publication
submitted in fulfilment
of the requirements for the degree
of
Doctor of Philosophy
in Electronic Engineering
at
The University of Waikato
by

Steven Owen McCabe

THE UNIVERSITY OF
WAIKATO
Te Whare Wānanga o Waikato

2019

Submitted for examination on 30 July 2018

Hard-bound submission on 08 April 2019

Abstract

Medical implants incorporating long insulated conductors can generate a serious heating hazard to a patient undergoing a Magnetic Resonance Imaging (MRI) scan. Under the high-power RF field from an MRI machine, the conductors can behave as antennas and concentrate energy into small regions of body tissue, leading to excessive joule heating. Neurostimulator implants that employ long electrode leads such as those for Deep Brain Stimulation (DBS) and Spinal Cord Stimulation (SCS), are highly susceptible to this RF hazard. Patients with these implants are generally contraindicated from MRI.

This thesis examines the heating phenomenon and identifies a variety of methods to mitigate the hazard and gain implant leads MRI safety. Techniques such as thin insulation, surface roughening, and auxiliary decoy filars are explored, with the latter shown to be especially effective at providing safety. Designs are first modelled with electromagnetic simulation software then experimentally proven inside of a gelled saline phantom within a 3 T MRI machine. A lab-based measurement method is also established to enable rapid low-cost testing of prototype lead designs.

Acknowledgements

I would like to thank everyone who supported me over my PhD studies and offered their assistance in one way or another. In particular I would like to acknowledge my primary supervisor and friend Professor Jonathan Scott for making this research possible. He provided his wealth of knowledge and expertise throughout and was a constant source of encouragement. One could not ask for a better supervisor.

I would like to thank Waikato University and WaikatoLink for funding and support, and especially Nidhie Kumar and Roz Murray, whose enthusiasm and hard work from beginning to end helped commercialise the work. I also would like to acknowledge Saluda Medical for their valuable collaboration and expertise.

A big thank you to Stephen Butler of Midland MRI for lending his evenings operating the MRI machine and assisting with measurements on which this thesis relies on. They were the most enjoyable physics experiments I have experienced. Thanks also to Joseph Haystead and my secondary supervisors Marcus Wilson and Michael Cree for their support and assistance with measurements, as well as Graham Saunders for his time preparing roughened wire samples. I would also like to acknowledge Mark Jones for his friendship during the course of our studies together and his willingness to offer help when needed.

Last but not least I would like to thank my parents, Owen and Pauline, and my fiancée Melody, for their loving encouragement and support throughout. They never let me forget that there would be light at the end of the tunnel.

Dedication

This thesis is dedicated to my good friend, Neil Askew, who left this world along the way. Neil was a truly talented man with a deep understanding of electronics and mathematics. He taught me electronics from an early age and inspired me to pursue electronic engineering at university. Much of what I know is thanks to Neil.

Contents

List of Figures

List of Tables

Chapter 1

Introduction

This research is presented as a "thesis by publication". It comprises a total of six published articles, two filed patents, and an accompaniment of various unpublished results and findings, which address the serious RF heating hazard that can occur when Magnetic Resonance Imaging (MRI) is used to scan a patient with a conductive lead implanted in their body.

Implants that provide Deep Brain Stimulation (DBS) to treat disorders such as Parkinson's Disease and Essential Tremor employ long insulated leads containing multiple conductive *filars*. These filars supply controlled therapeutic electrical stimulus from an impulse generator, typically implanted just above the pectorial region, to neural tissue deep within the patient's brain via small metallic electrodes located at the distal end of the lead. Spinal Cord Stimulation (SCS) implants for treating chronic back pain disorders are essentially identical in design, employing long leads with distal electrodes to stimulate specific regions of the spinal cord. While these systems are an effective treatment option for these debilitating disorders, they also contraindicate patients from having MRI scans.

Implant leads range up to several hundred millimeters in length and become resonant like antennas at the RF frequency of the MRI machine. In a 3 T machine the RF excitation field can deliver up to 30 kW in peak power at 128 MHz. Energy induced by the lead can transfer to the most distal electrodes and dissipate as heat in the surrounding neural tissue. Heating can

easily exceed the 1–2 °C safety threshold recommended by the International Commission on Non-Ionizing Radiation Protection (ICNIRP) and cause irreversible tissue damage. With the exception of just a couple of SCS products by Medtronic [1] and Boston Scientific [2], that are rated for conditional use only in 1.5 T MRI machines, DBS and SCS implants are generally unsafe for MRI. There are currently no products available that offer compatibility with higher strength 3 T MRI machines.

This research investigates a variety of new and existing techniques to circumvent this RF heating problem with the aim of providing both SCS and DBS implants compatibility in 3 T MRI machines. As a result of this work, two patents have been filed to date. These have led to a partnership between the University of Waikato and Saluda Medical, a medical implant company based out of Sydney, who intend to adopt the technology within the next iteration of their neurostimulator products for MRI compatibility.

The structure of this thesis as summarised in figure 1.1 comprises various published manuscripts ordered as follows:

The first research paper in the series investigates the RF heating phenomenon and presents electromagnetic models for simulating the behaviour of simple test leads in the RF field from 3 T MRI. Basic strategies to mitigate the heating such as increasing the ac resistance of the filar and modifying the insulation properties are explored.

Validation of the electromagnetic model and simulated results are provided in the second research paper. Using fiber-optic thermometry, temperature measurements of various test leads are performed in a gelled saline phantom within a 3 T MRI machine. Predicted results are reconciled against measurements.

The third research paper presents an alternative method for testing prototype lead designs without requiring access to an MRI machine. A simple dipole radiator driven by Continuous Wave (CW) power amplifier provides a convenient and low-cost method for obtaining rapid measurements in the laboratory.

A complementary measurement technique is described in the fourth research paper. Time Domain Reflectometry (TDR) is used to ascertain the resonant

length of an implant lead under test, such that the total number of tests required to determine the length for peak heating is minimised.

The remaining two research papers present the "Decoy" invention, a simple yet effective modification that dramatically improve the RF safety of ordinary implant leads in MRI machines. Tested not only on simple test leads with single filars, the work extends to leads with multiple filars, highlighting the effects of mutual coupling between filars and the sharing of surface area for heating when there is more than one electrode.

All aforementioned papers were published in various journal and conference proceedings. They are reproduced in chapters 2–7 but presented in a style that match the format of this thesis. Figure and table numbering have been amended to avoid duplicates and individual bibliographies have been removed and compiled within a full bibliography at the end of this thesis. Supplementary sections follow at the end of each manuscript, providing additional details of methods, results, and discussion that were otherwise not included in the published version. Excerpts from the Decoy and Surface-Roughened Filar international patents can be found in chapter 8, with full copies available online [3], [4].

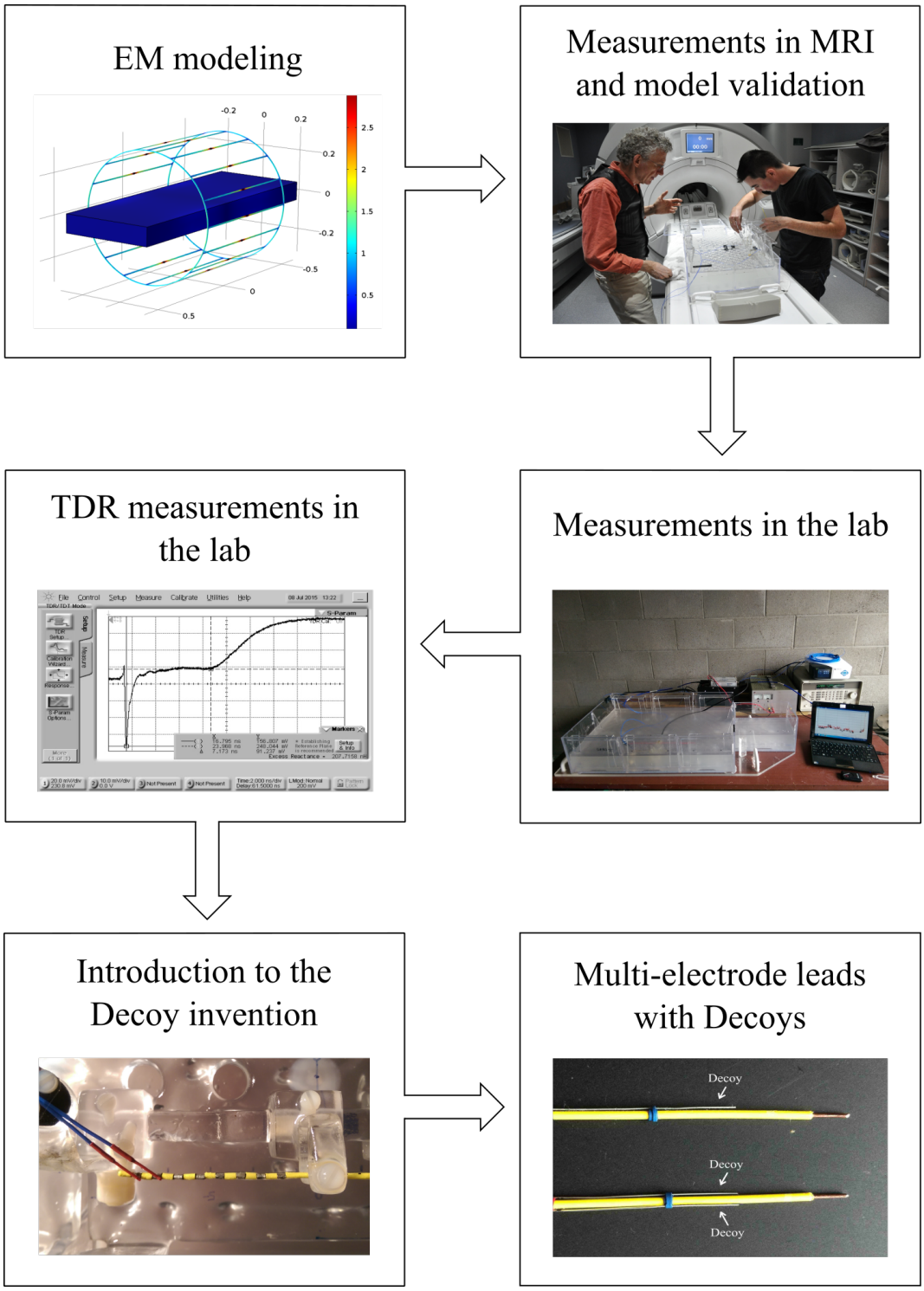

Figure 1.1: *Thesis structure showing the order of published manuscripts.*

Chapter 2

Investigation by Simulations

The manuscript in this chapter provides an opening to the RF problem that affects implant wearers when undergoing MRI. It covers research completed over the first quarter of the doctoral degree. First, simplified electromagnetic (EM) models are constructed in COMSOL Multiphysics software to simulate the RF environment of an MRI machine and its effect on embedded metallic implant structures. The model includes a homogeneous torso phantom with properties corresponding to that of neural tissue. COMSOL Multiphysics employs the Finite Element Method (FEM) to predict EM behaviour and is well suited for modeling these complex geometries when considerable computing power is available. Next, analysis of the results provide insight into the resonant phenomenon and reveal the seriousness of the heating hazard. Simple mitigation techniques through modifications of the implant lead are explored.

2.1 "Cause and Amelioration of MRI-Induced Heating Through Medical Implant Lead Wires"

Steven McCabe and Jonathan Scott
Department of Engineering, The University of Waikato, Hamilton, New Zealand

Published in the *Proceedings of the 21st Electronics New Zealand Conference (ENZCON 2014)*, Hamilton, 20-21 Nov. 2014, pp. 34–40.

The co-authorship form is provided in appendix A.

2.1.1 Abstract

The RF fields present in magnetic resonance imaging (MRI) scanners can induce hazardous heating in patients wearing medical implants. The inherent design and locale of deep brain stimulators (DBS) and spinal cord stimulators (SCS) make them particularly susceptible. We apply antenna concepts and use electromagnetic (EM) simulation to explain the phenomenon and anticipate its sensitivity to lead wire length. We anticipate that a DC resistance of less than $50\,\Omega$/m and an RF impedance of more than $1.23\,\mathrm{k}\Omega$/m would be required for a safe electrode for SCS use. We investigate the possibility of manipulating wire conductivity and diameter in order to use the skin depth effect to achieve a safe electrode. The effect of the thickness and permittivity of insulation surrounding the wires is explored.

2.1.2 Introduction

Around 14,000 Spinal Cord Stimulation (SCS) systems are implanted in patients every year. Pacemakers and cochlear implants represent a more mature technology with some 3-million pacemakers and 300,000 cochlear implants in service in the world today. The newest implant technology is Deep Brain Stimulation (DBS), already approved for the treatment of Parkinson's dis-

ease, essential tremor, dystonia, epilepsy, and Obsessive-Compulsive Disorder (OCD) [5]. The number of implants can be expected to increase. Most of the patients wearing these technologies are contraindicated for MRI scans.

Most scientists are aware of the strong static magnetic field associated with an MRI machine. In actual fact, an MRI machine presents a hazard through three mechanisms, the static magnetic field; the low-frequency magnetic fields; and the enormous RF field [6]. The RF field produced in the older-generation 1.5 T MRI scanners has a frequency of 64 MHz, whereas 3 T machines operate at 128 MHz. A typical scan sequence can have RF pulses of up to 20 kW in power[7]. This can lead to significant heating of RF absorbers.

The International Commission on Non-Ionizing Radiation Protection (ICNIRP) recommends localised temperatures should remain below 38 °C in the head, 39 °C in the torso, and 40 °C in the limbs [8]. In an MRI machine, the dielectric heating of a patient is monitored by the Specific Absorption Rate (SAR), the power absorption per unit mass of tissue. The SAR is typically averaged over the whole-body, whole-head, or 10 g of mass. There are claims in the literature that the measure is too coarse for detecting the power absorption near implants [9]. Highly concentrated electric fields near the small implant electrode can go undetected, leading to a higher than normal level of heating in this region.

Pacemakers are implanted close to the heart and have relatively short lead wires. This is also true of cochlear implants. SCS and DBS systems, on the other hand, have leads placed in the epidural cavity of the spine or deep in the skull, while the impulse generator and battery unit are normally placed in the chest cavity. In these systems, leads can easily exceed 600 mm in length. The leads are typically made of platinum wires running inside plastic polymer sheaths. Serious and fatal experience has shown that the RF heating risk rises with these longer leads [6], [9]. The MRI safety of implants has become a global issue and sites such as Shellock [10] are consulted throughout the world by MRI radiologists.

A spate of patents have appeared in the last decade supposedly addressing the issue of providing an MRI-safe electrode [7], [11]–[15]. Many seem to be conspicuously speculative in nature. Only one product has appeared [16]. It

is rated for use only in 1.5T machines, and only with a restricted scanning protocol. The original patent appeared in 2010 [17].

In this work, we use Finite Element Method (FEM) simulation software to model the localised electric fields and temperature changes at the distal electrode of an implant lead wire as a function of length, in a 3 T MRI environment. We then explore various techniques that aim to reduce the level of RF heating. The first approach exploits the skin effect to maximise the AC resistance at RF, while maintaining a sufficiently lower resistance at the normal operational frequency of the neurostimulator. The second approach involves selection of suitable values for the insulation permittivity and thickness to reduce the characteristic impedance of the implant lead wire at RF. Verification of the improvements are provided by simulated results.

2.1.3 Simulation Models

The model, implemented in both two and three dimensions; is comprised of an insulated platinum wire (of variable length), embedded within a conductive phantom, inside of an RF antenna. The antenna operates at 128 MHz, the RF frequency of a 3 T MRI machine. The three-dimensional model offers a more accurate representation of the MRI birdcage and rectangular phantom, and is used to assess the hazardous heating phenomenon. When the highest accuracy is not of critical importance, the computationally less demanding two-dimensional axisymmetric model is used.

Three-Dimensional Model

A list of the design parameters for the following components can be found in the appendix.

1) RF Birdcage Antenna Modeled as a 16-rung birdcage antenna with a 0.6 m bore as shown in figure 2.1. The antenna generates circularly polarised electromagnetic (EM) waves with a free-space wavelength λ_0 of 2.34 m.

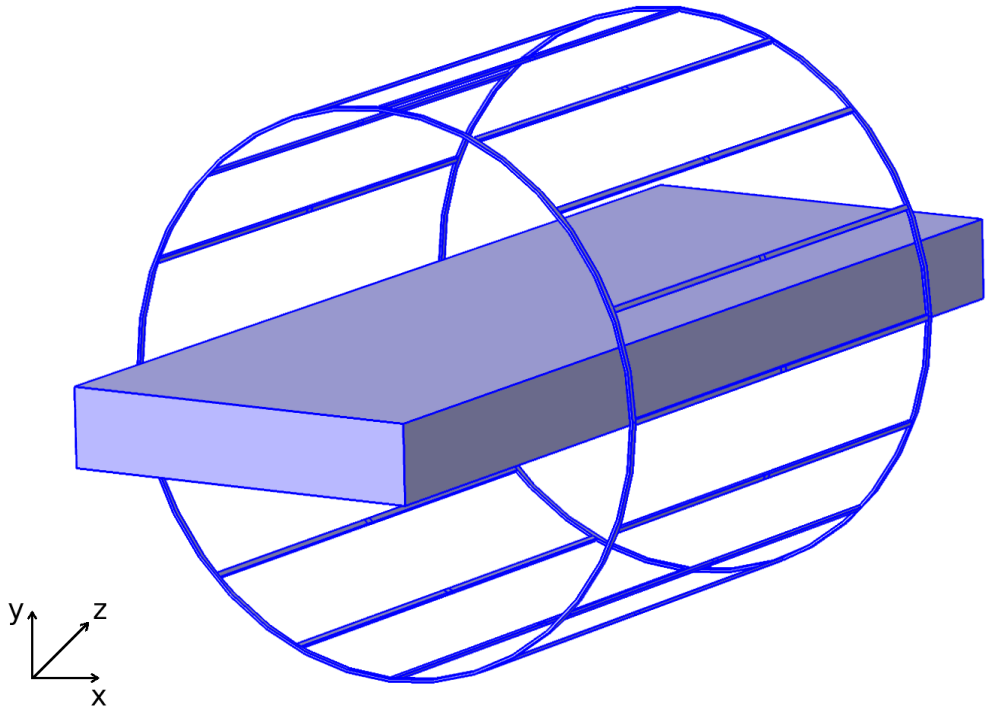

Figure 2.1: *Conductive phantom surrounded by a 16-rung RF birdcage antenna. A spherical perfectly matched layer surrounds the antenna (not shown).*

Each rung is centre-driven by a sinusoidal signal[1]; differing by 22.5 ° in phase between adjacent rungs, with a total phase variation of 360 ° around the circumference of the antenna. All outgoing radiation is absorbed by a spherical perfectly matched layer (PML) surrounding the antenna.

2) Phantom The parameters for the headless phantom model are set according to the ASTM F2182-11a international test standard [19] with the exception of the length parameter, which is doubled from 0.6 m to 1.2 m, to accommodate the testing of longer length wires. Blood perfusion is optional.

3) Implant Modeled as a 700 µm platinum wire with polyurethane insulation as shown in figure 2.2. A small portion of the insulation is missing from one end, to imitate a distal electrode. A virtual cylindrical domain surrounding the distal electrode provides an enclosed boundary for subsequent extraction

[1]Practical birdcage antennas are typically fed between two points and require a multitude of tuning capacitors. For simulation purposes, simplification can be achieved by feeding an appropriate signal phase to the centre of each rung directly, eliminating the need for tuning capacitors [18].

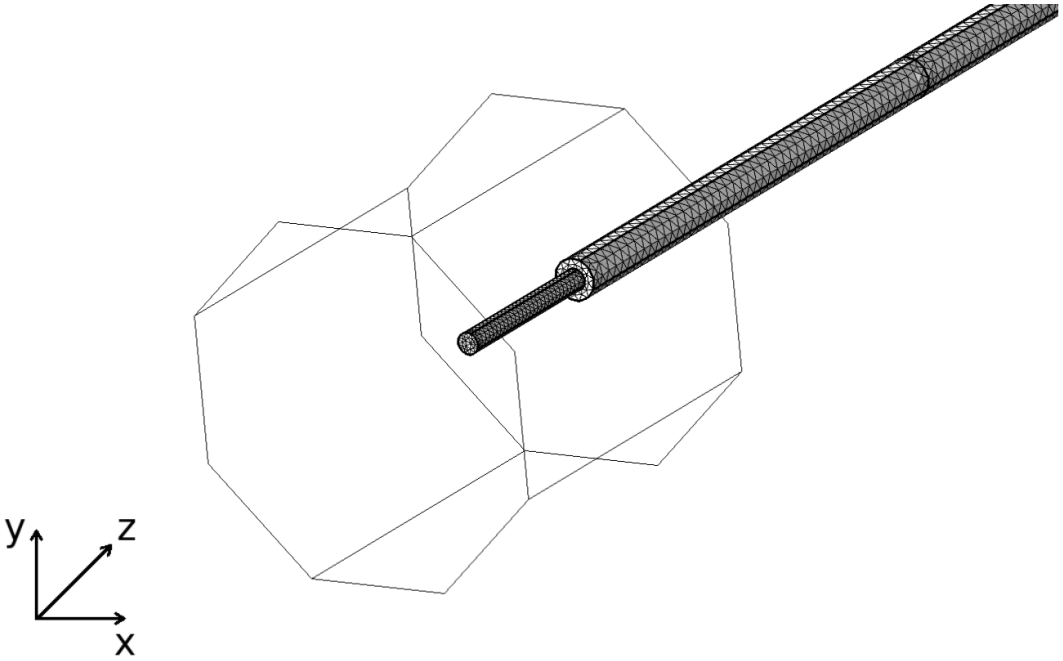

Figure 2.2: *The wire implant is comprised of a platinum conductor,* 700 µm *in diameter, surrounded by polyurethane insulation.* 6 mm *of insulation is missing from one end, representing the implant electrode.*

of the peak temperature. The opposite end of the wire is capped off with the polyurethane insulating material.

This is a simplified model of a more complex lead wire composed of multiple conductors, electrodes, and dielectrics.

Two-Dimensional Axisymmetric Model

Simulation times are significantly reduced for two-dimensional axisymmetric models (hours instead of days); however, only rotationally symmetric ones can be constructed in this space. A magnified view of the model showing the distal electrode is in figure 2.3. The MRI antenna (not shown) is simulated as a cylinder with a uniform current distribution. The radius and length are set to the same values as used in the three-dimensional model. Similarly, the phantom is modified to be cylindrical, with a radius of 0.21 m and a length of 1.2 m. The remaining relevant parameters are set to the same values listed for the three-dimensional model in the appendix.

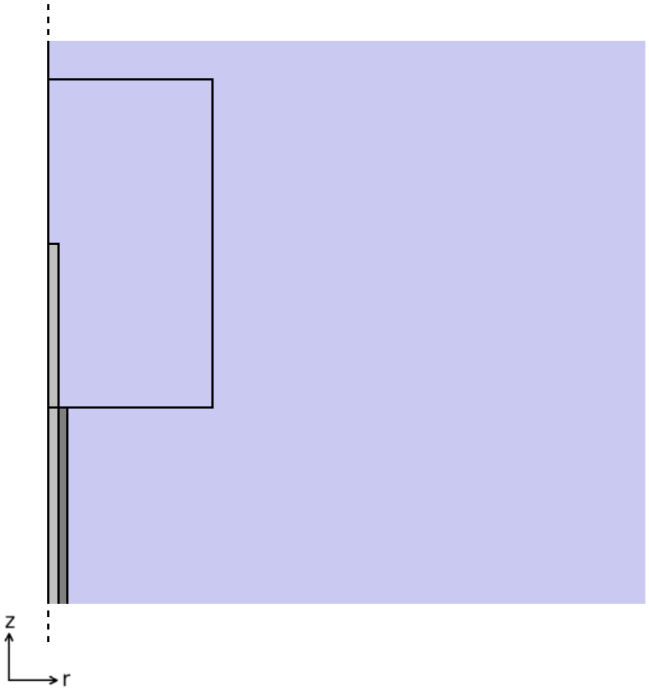

Figure 2.3: *Magnified view of the two-dimensional axisymmetric wire implant model with a virtual domain surrounding the distal electrode. The dashed lines represent the rotational axis.*

Simulation Settings

For the subsequent simulations, the background Specific Absorption Rate[2] (SAR) was calibrated to a relatively modest level of 1 W/kg. The end time for temperature extraction was set to $t = 15\,\text{min}$, the typical scan-time for MRI. Initial temperatures of the phantom and implant at $t = 0$ were 37 °C. Simulations were performed using the COMSOL Multiphysics 4.4 commercial software package.

2.1.4 Resonant Length

An implanted lead wire acts as a dipole antenna when exposed to the RF field from MRI. In this section, we explore the resonance phenomenon for the simple case of an uninsulated wire in a lossless medium, and then again for a lossy

[2]The average SAR in the volume of the phantom, in the absence of the implant. Note that a non-conductive medium ($\sigma_P = 0$) will not absorb RF energy, and so the background SAR will consequently be zero. For the purpose of simulations, we apply the same signal amplitude to the antenna as we do for the lossy version.

medium. Insulation is then added to the wire to replicate an implant lead wire and its effect is shown. The results are shown in terms of the average (mean) of the electric field enclosed within the virtual domain surrounding the distal end/electrode of the wire.

Dipole Resonance

In a lossless medium ($\sigma = 0$), an ordinary dipole antenna will resonate when excited by an RF field when its length is approximately equal to an odd integer multiple of the half-wavelength: 0.5λ, 1.5λ, 2.5λ, $\cdots$. The wavelength of an EM wave in a lossless medium can be computed from

$$\lambda = \frac{2\pi}{\omega\sqrt{\mu\epsilon}} \tag{2.1}$$

where ω is the angular frequency, and μ and ϵ are the permeability and permittivity of the medium, respectively.

If the medium is conductive, the wave will compress. According to [20] the wavelength can be calculated from:

$$\lambda = \sqrt{\frac{8\pi^2}{\omega^2\mu\epsilon}} \cdot \left[\sqrt{1 + \left(\frac{\sigma}{\omega\epsilon}\right)^2} + 1\right]^{-1/2} \tag{2.2}$$

Furthermore, the induced antenna currents are not confined by the ends of the wire and are free to extend into the medium [21]. The antenna is effectively lengthened by the medium itself.

Lossless Phantom, Bare Wire

Suppose the phantom described in section 2.1.3 is the medium, but with zero conductivity ($\sigma_P = 0$), such that it is lossless. From equation 2.1, the wavelength inside of the phantom would be $\lambda_{P0} = 0.26\,\text{m}$. A conductive wire within this region would be expected to resonate strongly when the length meets the aforementioned condition for resonance.

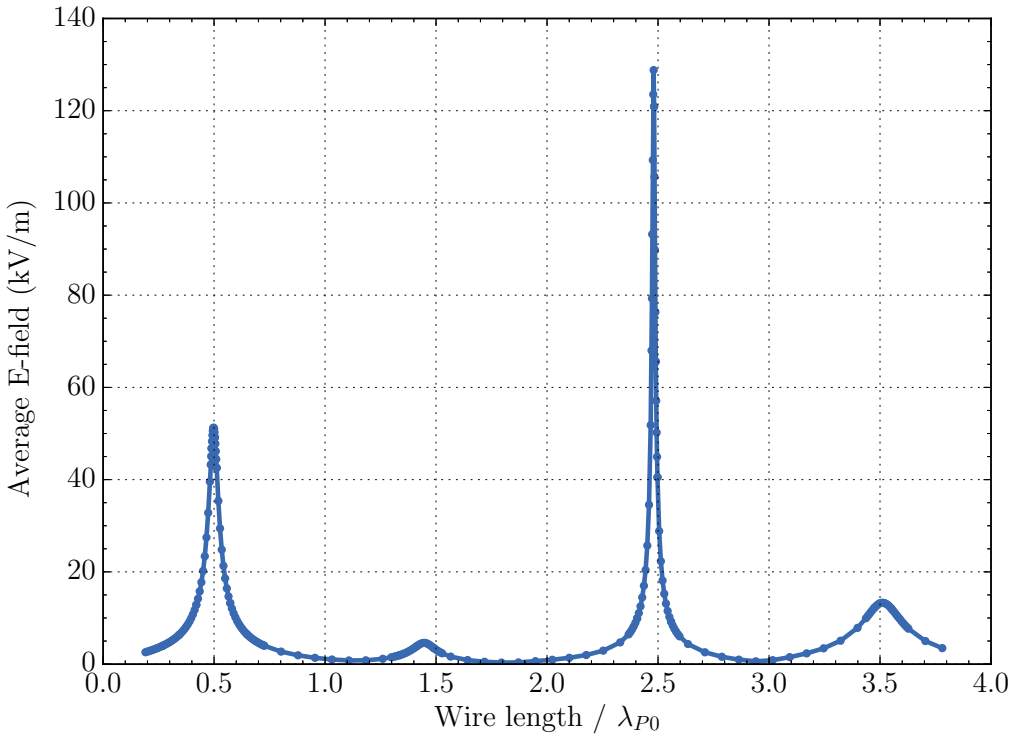

Figure 2.4: *Average E-field at one end of a* 700 µm *diameter bare wire for various lengths when the phantom is lossless* ($\sigma = 0$).

To verify this dipole antenna behavior, the two-dimensional axisymmetric model was simulated but with $\sigma_P = 0$ and no insulation on the platinum wire. The average electric field surrounding one end of the wire was extracted as a function of wire length. The location of the resonant frequencies correspond to that of a dipole antenna as is shown in figure 2.4. The average electric field in the space around the end of the wire maximises at resonance, the point when the end-to-end voltage on the dipole would be at maximum. Variation in the magnitude of each resonant peak can be attributed to the change in antenna impedance as the length is varied.

Lossy Phantom, Bare Wire

When the phantom has a finite conductivity of $\sigma = 0.47\,\mathrm{S/m}$, the international standard for MRI phantoms [19], the wavelength will shorten to $\lambda_P = 0.24\,\mathrm{m}$, according to equation 2.2. Simulation confirms a strong resonance at $0.41\lambda_P$, just shy of the half-wavelength as is shown in figure 2.5. Unlike the previous

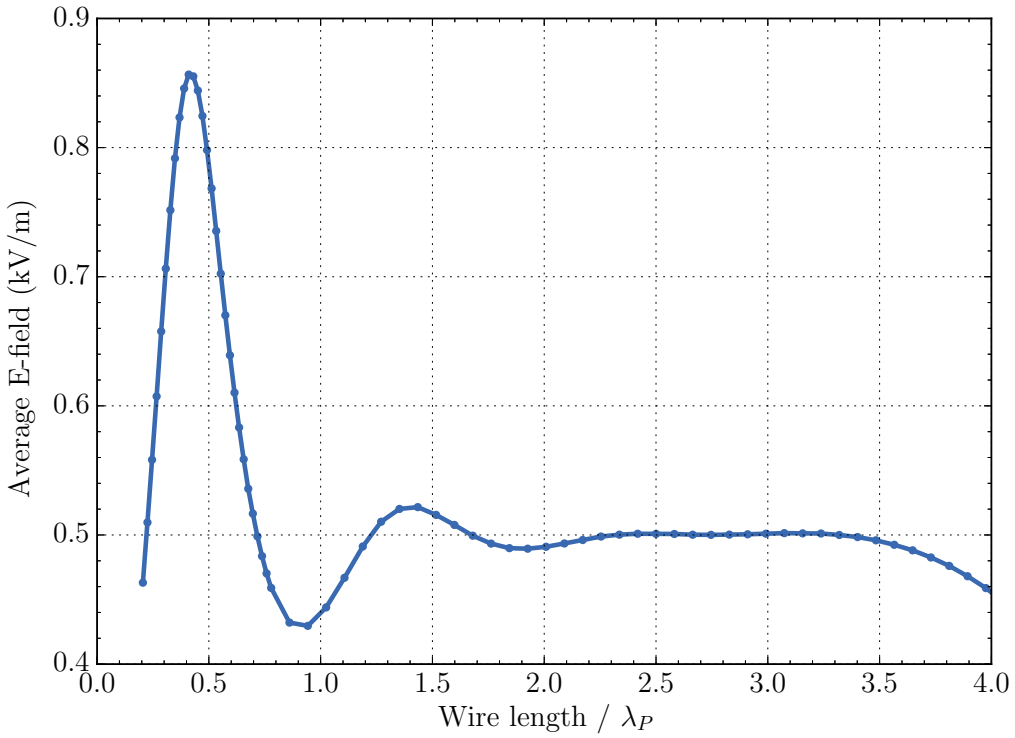

Figure 2.5: *Average E-field at one end of a* 700 µm *diameter bare wire for various lengths when the phantom is lossy* ($\sigma = 0.47\,\mathrm{S/m}$).

simulation where the phantom was non-conductive, induced currents have now entered the phantom from each end of the wire, changing its resonant behavior.

Lossy Phantom, Mostly-Insulated Wire

Simulation of the wire with insulation covering all but one end (the distal electrode) was performed. The average electric field near the distal electrode at various wire lengths is in figure 2.6. The length is normalised to

$$\lambda_{Pn} = 0.59\,\mathrm{m}$$

such that the first resonant peak occurs at $0.41\lambda_{Pn}$. Not only has the insulation shifted the resonant frequency but it has also increased the electric field intensity at the first resonant peak threefold.

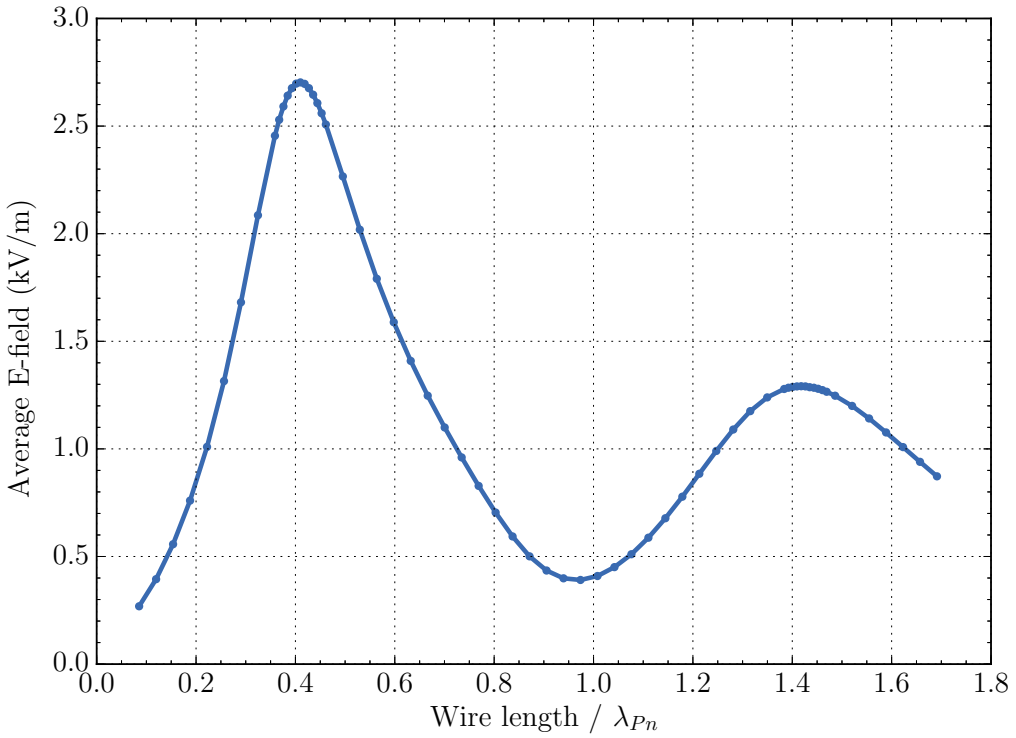

Figure 2.6: *Average E-field at the distal electrode of an insulated wire in a lossy phantom ($\sigma = 0.47\,\mathrm{S/m}$). The insulation covering the* 700 µm *diameter wire is* 315 µm *thick. The wire length is normalised to a wavelength of* 0.59 m.

2.1.5 RF Heating

The change in temperature ($T - 37\,^{\circ}\mathrm{C}$) at the distal electrode of the insulated wire after 15 min of MRI scanning, was simulated using the three-dimensional model from section 2.1.3. The result is shown in figure 2.7. The x-axis is normalised to the wavelength of the electric field within the phantom, λ_{Pn}.

The exclusion of blood perfusion from the model provides an approximation of a worst-case scenario. At $0.41\lambda_{Pn}$ (0.24 m), normal body temperature is exceeded by almost 32 °C, well over the 2 °C limit for SCS. The peak temperature declines at longer wire lengths, similar to that of typical SCS and DBS lead wires, however, still exceeds specifications. A two-dimensional slice of the temperature T in the x-z plane at $y = 0$ is shown in figure 2.8, for when the wire length is $0.41\lambda_{Pn}$.

The model with blood perfusion offers more realistic values for temperature

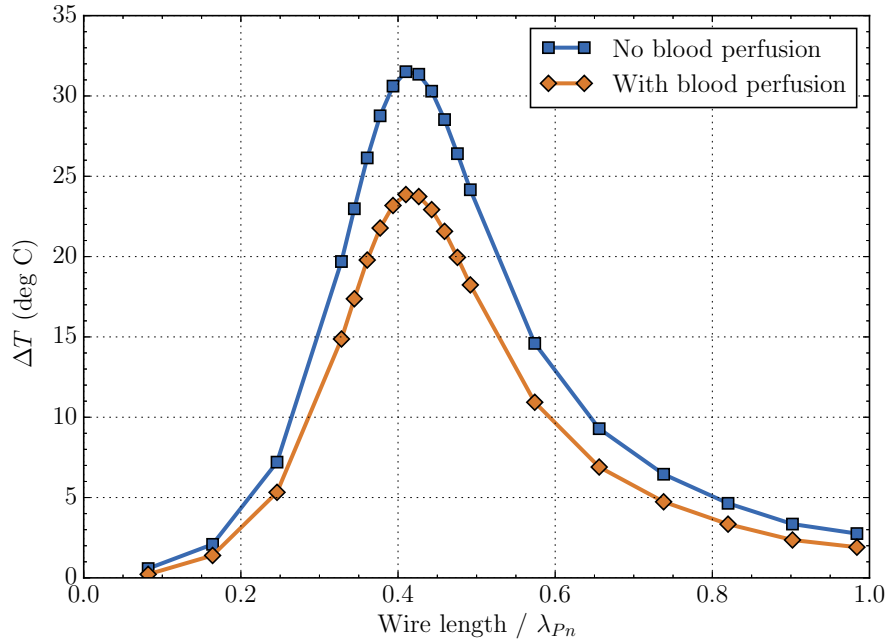

Figure 2.7: *The change in temperature* ΔT *near the distal electrode of the insulated wire after 15 minutes of simulated scanning. The insulation covering the* 700 µm *diameter wire is* 315 µm *thick. The length of the wire is normalised to a wavelength of* 0.59 m.

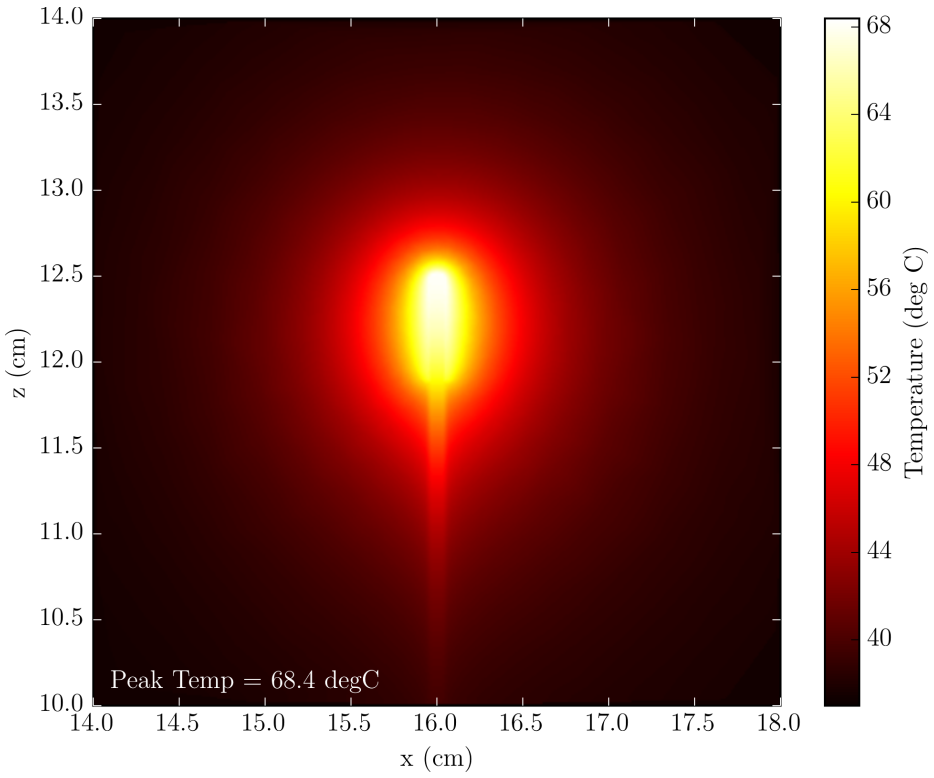

Figure 2.8: *The worst-case* $T(x, z)$ *at the distal electrode after 15 minutes of simulated scanning. The wire length was* $0.41\lambda_{Pn}$ *and blood perfusion was omitted. The initial temperature was* 37 °C.

when there is sufficient blood flow around the distal electrode. Nevertheless, even with this heat loss, the peak temperatures reached are alarming. An implant comprising of an insulated wire(s) similar to the one simulated here, should be considered absolutely unsafe for MRI.

2.1.6 Method 1: Increase R_{AC}

A reduction in the heating of the tissue near the distal electrode could be achieved with the addition of a uniformly distributed AC resistance into the implant wire. The resistance would act to impede the flow of induced current (Ohm's law), leading to a reduction in power dissipation within the surrounding tissue of the distal electrode.

The proposed method for increasing the AC resistance of the wire is to select appropriate values for the radius r_w and resistivity ρ_w of the wire conductor such that the skin effect is maximised (see figure 2.9). In this section, we first determine the amount of AC resistance needed to reduce the heating to safe levels. Next, we discuss the skin effect and present equations for computing the AC resistance. Lastly, we determine values for r_w and ρ_w that will best reduce the heating effect.

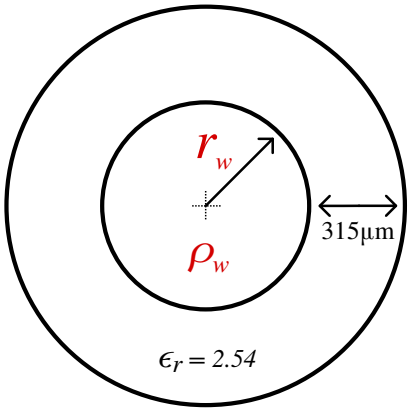

Figure 2.9: *The AC resistance of a conductive wire is a function of its radius and resistivity.*

Minimum R_{AC} Needed

To approximate the level of resistance necessary in the lead conductors of DBS and SCS systems, three-dimensional simulations of a hollowed out version of the implant wire were performed. The resistance was varied by controlling the resistivity of the metal. To ensure current uniformity, the resistivity was constrained to values such that the skin depth exceeded the thickness of the metal by at least 10 times. The AC resistance and the temperature change after 15 min as a function of the metal resistivity is shown in figure 2.10.

With 2 °C being the maximum level of heating allowed in the torso, it is apparent an SCS system would require at least 1.23 kΩ/m of AC resistance. Similarly, a maximum temperature change of 1 °C in the head, corresponds to a minimum AC resistance of 2.22 kΩ/m in DBS lead wires. Typically, neurostimulators are required to have no more than 50 Ω/m of DC resistance, such that the stimulation amplitude levels and battery life are not impaired.

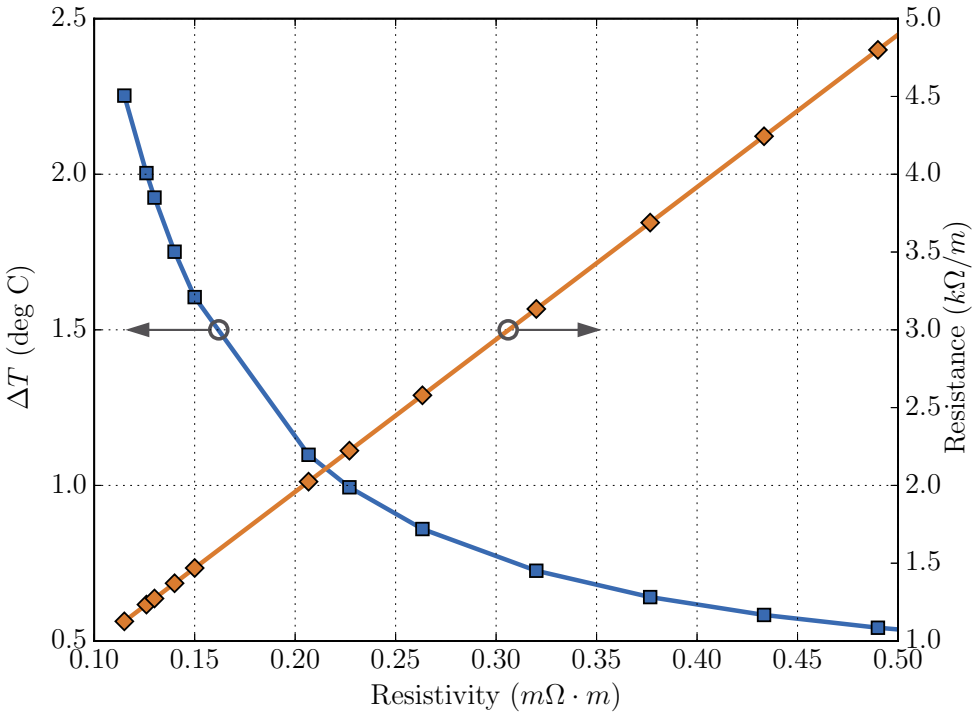

Figure 2.10: *The change in temperature ΔT near the distal electrode after* 15 min *of simulated scanning for a selected amount of uniform wire resistance. The linearity between the resistance and resistivity confirms that the skin depth is sufficiently larger than the metal thickness, such that the current is uniform.*

Skin Effect

The AC current density J in a wire decays exponentially as a function of depth from the surface:

$$J = J_S e^{-d/\delta} \tag{2.3}$$

where J_S is the current density at the surface, d is the depth from the surface, and δ is the skin depth. The skin depth is defined as the point where the current density has fallen to $e^{-1} \approx 37\%$. For highly conductive materials at RF, the skin depth can be sufficiently approximated to

$$\delta \approx \sqrt{\frac{2\rho}{\omega\mu}} \tag{2.4}$$

where ρ and μ are the resistivity and permeability of the conductor, respectively [22].

Resistance

A solid wire with uniform cross-sectional area, composed of a single homogenous material, has a resistance given by Pouillet's law:

$$R = \frac{\rho l}{A_{\mathit{eff}}} \tag{2.5}$$

where l is the length of the wire and A_{eff} is the effective cross-sectional area of the wire. For a cylindrical wire at DC, the current distribution is uniform and so $A_{\mathit{eff}} = \pi r^2$, where r is the radius of the wire. For AC, the current density is modified by the skin effect, where $A_{\mathit{eff}} \approx 2\pi r\delta$ for $r \gg \delta$.

To estimate the AC resistance when the wire radius is in the order of skin depths, a better approximation for the effective area is needed. The Modified Lorentzian Method [23] is a more accurate approximation even for conductors with radii much less than the skin depth. The effective area is calculated from

$$A_{\mathit{eff}} = \pi(2r\delta' - \delta'^2)(1 + y) \tag{2.6}$$

where

$$\delta' = \delta(1 - e^{-r/\delta})$$

$$y = \frac{0.189774}{(1 + 0.272481[z^{1.82938} - z^{-0.99457}]^2)^{1.0941}}$$

$$z = \frac{0.62006r}{\delta}$$

With equations 2.5 and 2.6, the AC and DC resistance was computed for a platinum wire ($\rho_w = 1.06 \times 10^{-7}\Omega m$) over a range of radii as shown in figure 2.11. Higher values of AC resistance are evident when the radius is small. However, the skin effect becomes less effective at smaller radii and the difference between the AC and DC resistance approaches zero. At the DC resistance limit of 50 Ω/m, the AC resistance is 59.2 Ω/m, with a radius of 26 µm. Through extrapolation of the simulated results in figure 2.10, this level of AC resistance will reduce ΔT to 27.6 °C at the worst-case length, an improvement of 14%.

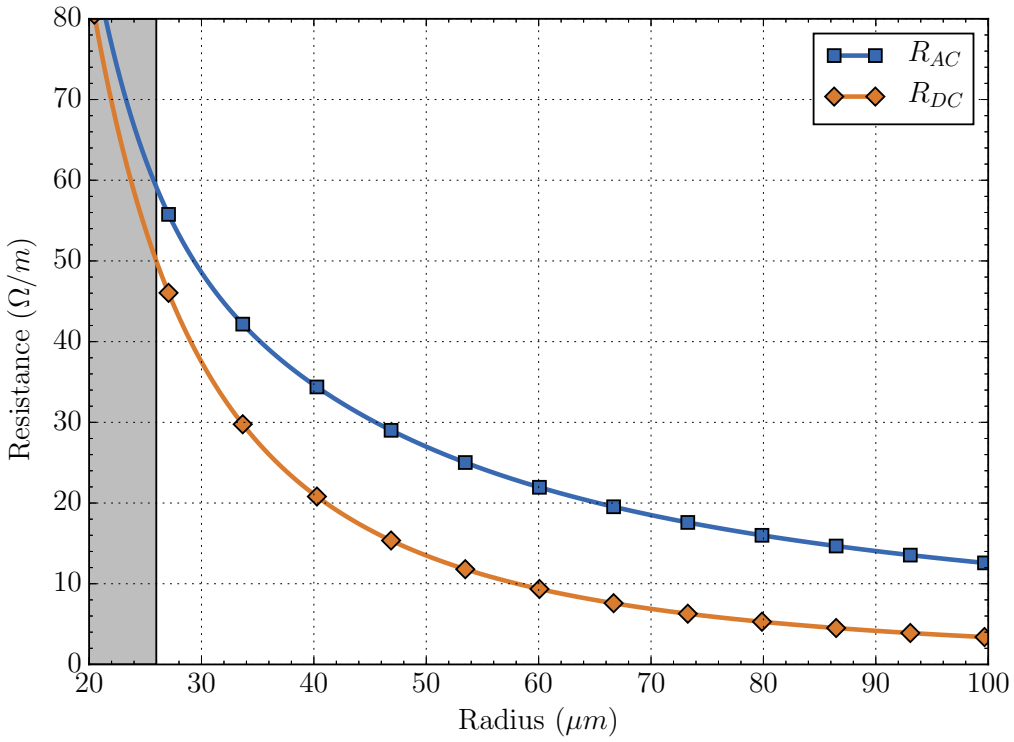

Figure 2.11: *The AC and DC resistance for a platinum wire over a range of radii. The shaded region is where the DC resistance exceeds the* 50 Ω/m *limit.*

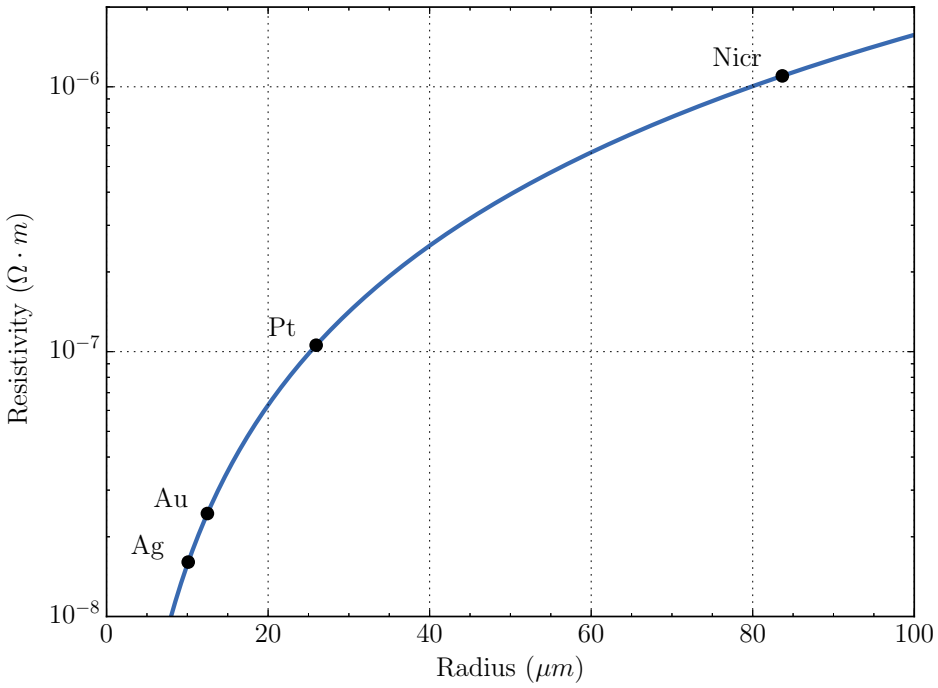

Figure 2.12: *Relationship between the wire resistivity and radius for a constant DC resistance of* 50 Ω/m. *The AC resistance is constant at* 59.2 Ω/m *over the entire range. Labels are shown for Silver (Ag), Gold (Au), Platinum (Pt), and Nichrome (Nicr).*

For mechanical reliability, the radius of the wire may need to be larger than 26 µm. To achieve this without compromising on the AC resistance, the resistivity of the wire must be increased. The relationship between the radius and resistivity for a DC resistance of 50 Ω/m is shown in figure 2.12. The AC resistance is constant at 59.2 Ω/m over the entire range.

It is clear that at the specified RF frequency and DC resistance, the skin effect alone will not generate enough AC resistance to reduce heating to safe levels.

2.1.7 Method 2: Tune Wire Insulation Parameters

In section 2.1.4, the insulation on the wire was shown to have an effect on the intensity of the electric field at the distal electrode. In this section we liken the implant lead wire to an RF transmission line and assess the electric field and heating of the distal electrode when the insulation's permittivity in figure 2.13a and thickness in figure 2.13b is varied.

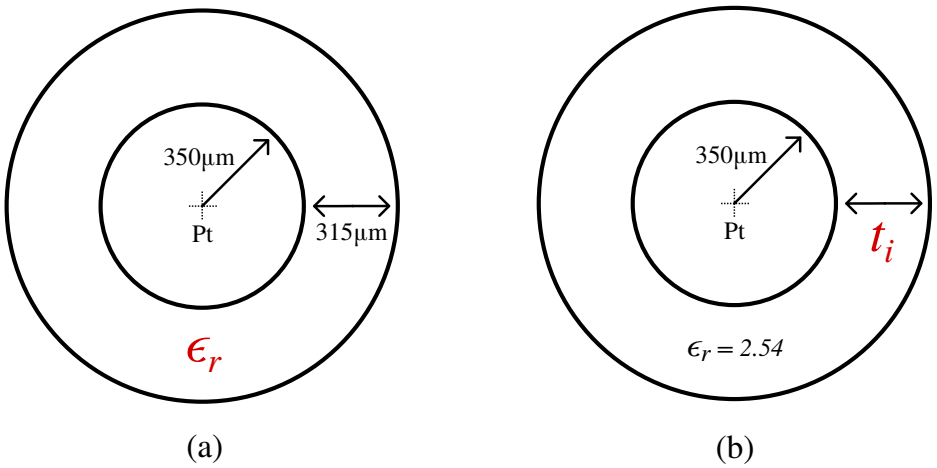

Figure 2.13: *The electric field and the heating at the distal electrode is a function of the insulation's (a) permittivity (b) and thickness.*

Neglecting series resistance and shunt conductance, the characteristic impedance of a uniform coaxial transmission line can be calculated from

$$Z_0 = \frac{1}{2\pi}\sqrt{\frac{\mu}{\epsilon}} \cdot \ln\left(\frac{r_2}{r_1}\right) \tag{2.7}$$

where r_1 is the radius of the inner conductor, r_2 is the radius of the outer conductor, and μ and ϵ are the absolute permeability and permittivity of the dielectric material, respectively.

To some approximation, an implanted lead wire resembles a coaxial transmission line but with conductive tissue representing the outer cylindrical conductor [24]. Modification of the permittivity and thickness $(r_2 - r_1)$ of the wire insulation will have a direct impact on its Z_0, and therefore, the amount of RF energy that is coupled to the implant lead wire.

Permittivity

Simulations of the two-dimensional model over a range of insulation permittivities yielded the result in figure 2.14. The wavelength in each sweep is normalised to:

$$\lambda_{P\epsilon_r} = \begin{cases} 0.59\,\text{m}, & \epsilon_r = 2.54 \\ 0.46\,\text{m}, & \epsilon_r = 5 \\ 0.37\,\text{m}, & \epsilon_r = 10 \\ 0.26\,\text{m}, & \epsilon_r = 80 \end{cases}$$

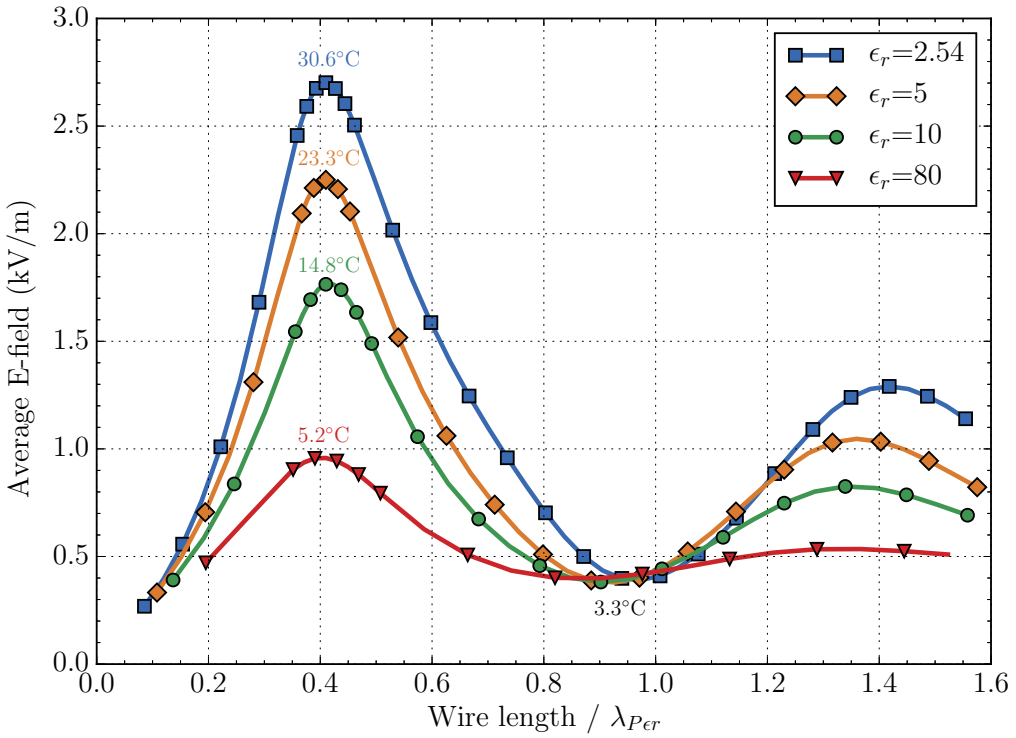

Figure 2.14: *Average E-field at the distal electrode for various insulation permittivities when $t_i = 315\,\mu\text{m}$. The overlaid values for ΔT were derived using the three-dimensional model. The length of the wire is normalised to stated values.*

Due to long computation times, three-dimensional simulations of ΔT near the distal electrode at $t = 15\,\text{min}$ were performed only at the worst and best-case wire lengths. The values are overlaid on the same figure. Despite the considerable reduction in heating at higher permittivity values, the improvement is still not quite enough, even when ϵ_r has an impractical value of 80.

Thickness

A similar result can be found when sweeping the insulation thickness as shown in figure 2.15. The wavelength in each sweep is normalised to:

$$\lambda_{Pt_i} = \begin{cases} 0.28\,\text{m}, & t_i = 10\,\mu\text{m} \\ 0.40\,\text{m}, & t_i = 75\,\mu\text{m} \\ 0.48\,\text{m}, & t_i = 150\,\mu\text{m} \\ 0.59\,\text{m}, & t_i = 315\,\mu\text{m} \end{cases}$$

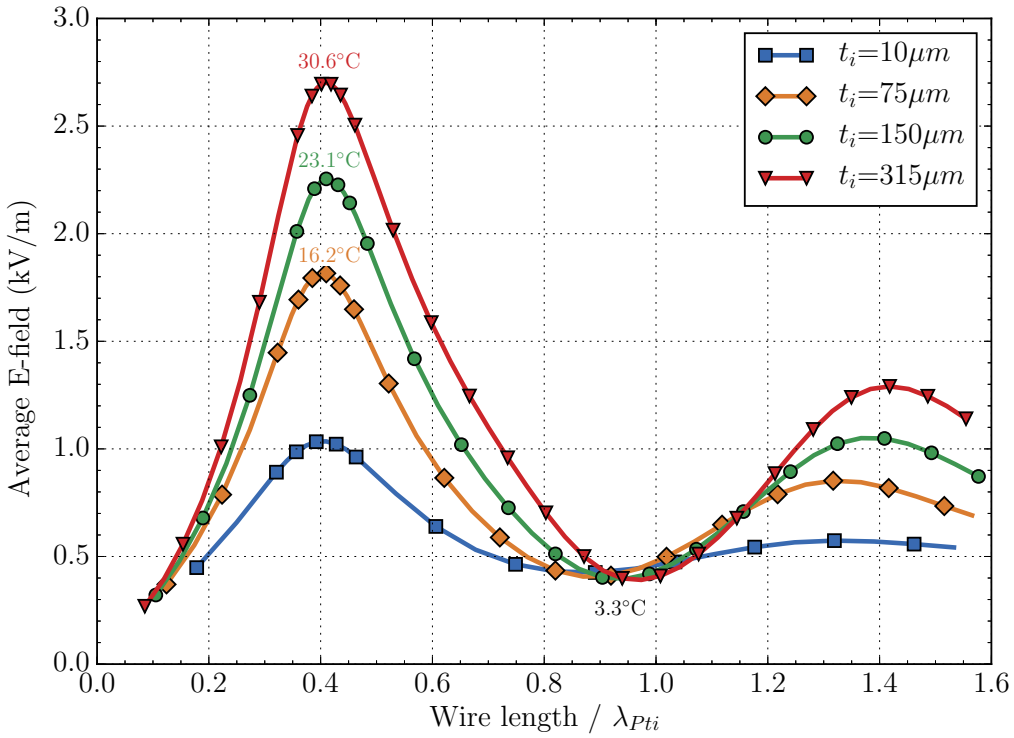

Figure 2.15: *Average E-field at the distal electrode for various thickness of insulation when* $\epsilon_r = 2.54$. *The overlaid values for* ΔT *were derived using the three-dimensional model. The length of the wire is normalised to stated values.*

It can be seen that by decreasing the thickness of the insulation, heating can be reduced significantly. Again, modifying the thickness parameter alone is unlikely to reduce the heating to safe levels, especially when the thickness becomes impractically small.

2.1.8 Conclusion

When an insulated wire of sufficient length is embedded within conductive tissue and subject to MRI, it essentially becomes a dipole antenna, absorbing RF energy and heating the distal electrode and surrounding tissue to unacceptable levels. We have shown that a resistance of 1.23 kΩ/m is sufficient to reduce distal heating to a safe level for SCS, where implant manufacturers would like a resistance of less than 50 Ω/m for power consumption reasons. We have also shown that it is impractical to rely on the skin effect to give this combination of resistances in a 3 T machine. Either a thin or very high dielectric insulation

could significantly reduce distal heating but may not be viable through considerations of reliability and patient safety. It may be possible that a combination of these design solutions could achieve an MRI-safe neurostimulator lead wire.

2.1.9 Acknowledgement

We would like to thank the Waikato Medical Research Foundation (WMRF) for funding. We also acknowledge WaikatoLink and KiwiNet for their valuable support. Thanks are due to the University of Waikato for their research scholarship.

2.1.10 Appendix

Table 2.1: *3D model parameters.*

	Parameter	Assignment
Birdcage antenna [18]	r_b	0.3 m
	l_b	0.6 m
	Material	PEC
	N_{rung}	16
	w_{rung}	6 mm
	f	128 MHz
	$\Delta\phi$	22.5 °
Phantom [19], [25]	w_p	0.42 m
	l_p	1.2 m
	h_p	0.09 m
	(x_p, y_p, z_p)	Centered within antenna
	ϵ_{rp}	80
	μ_{rp}	1
	σ_p (optional)	0.47 S/m
	ρ_p	1000 kg/m^3
	C_{pp}	4150 J/(kg K)
	k_p	0.6 W/mK
Blood perfusion (optional) [26]	T_b	37 °C
	C_b	4180 J/(kg K)
	ω_b	6.4×10^{-3} (1/s)
	ρ_b	1000 kg/m^3
	Q_{met}	0 W/m^3
Implant wire[3] **(Platinum)** [6]	r_w	0.35 mm
	l_w	Variable
	(x_w, y_w, z_w)	(0.16 m, 0, 0)
	Bound. mesh t_{bw}	$\delta_{Pt}/4$
	Bound. mesh N_{bw}	20
Implant insulation (optional) [6], [27]	t_i	0.315 mm
	l_i	$l_w - 6$ mm
	ϵ_{ri}	2.54
	μ_{ri}	1
	σ_i	4.7×10^{-4} S/m
	c_{pi}	1760 J/(kg K)
Virtual domain	r_v	6 mm
	l_v	12 mm
	(x_v, y_v, z_v)	Centered about tip face
Perfectly matched layer (PML) [28]	Inner radius	$2.0\lambda_0/4$
	Outer radius	$2.5\lambda_0/4$

[3] The skin depth of platinum at 128 MHz is 14.4 µm.

2.2 Further Results and Discussion (Unpublished)

2.2.1 Resonant Heating

Resonant heating near implant lead electrodes has a strong dependence on lead length as was depicted in figure 2.7. While it may seem tempting to claim MRI safety of lead lengths that are distant from the resonant peak, it would be misleading to do so. Regardless, it is not uncommon in studies for consideration to be given only to single conductor lengths [29]–[34].

Aside from the lead construction and its material properties, there are numerous other factors that can influence the resonant length and peak temperature. For example, variation in the tissue type and its properties, location of the implanted lead with respect to the patient and the MRI fields, the orientation of the implanted lead, and presence of bends and loops in the lead, can all strongly influence the resonant behaviour [6], [9], [35]–[38]. In addition, figures 2.4–2.6 shows resonant modes can exist beyond one half-wavelength[4]. When designing leads it is therefore important to characterise distal heating over a wide range of lead lengths, to better assess its MRI safety.

2.2.2 AC Resistance of High Permeability Filars

In section 2.1.6 the manipulation of filar conductivity and diameter was proven insufficient for providing the necessary level of AC resistance required without demanding high DC resistance and impractically thin wire. The skin effect at 128 MHz just doesn't provide the amount of loss to that which is expected when dealing with microwave energy. However, it is important to note that only materials with $\mu_r = 1.00$ were included in the study.

Implants constructed from ferromagnetic materials generally contraindicate patients from MRI. Induced forces on the implant from the static and gra-

[4]A strong near-field interaction between the implant lead and the centre-driven rungs of the birdcage antenna prevent modes occurring at even integer multiples of the half-wavelength. This is also true for simple dipole antennas, unless the driving port is matched with a high input impedance or offset by 1/4 of the total dipole length.

dient magnetic fields can present a hazard to the patient [6]. Furthermore, distortion of the MRI fields from these materials can lead to artifacts that significantly obscure the MRI image [39]. Nevertheless, materials with moderate relative permeabilities of $\mu_r > 1$ may be tolerable, particularly in the fields from machines with smaller magnets.

With equations 2.4 and 2.5 and with the approximation $A_{eff} \approx 2\pi r\delta$ when $r \gg \delta$, the AC resistance of a solid cylindrical wire can be expressed as:

$$R_{AC} = \frac{l}{\pi r}\sqrt{\frac{\rho\omega\mu}{8}} \tag{2.8}$$

Unlike AC resistance, the DC resistance has no dependence on the permeability of a material:

$$R_{DC} = \frac{\rho l}{\pi r^2} \tag{2.9}$$

Therefore, high loss at AC can be achieved at the same time as maintaining low loss at DC. A metal such as Nickel can have $\mu_r = 600$ with $\rho_w = 7.0 \times 10^{-8}\,\Omega$m. Its skin depth is just 0.5 µm at 128 MHz. Substitution of these parameters into equations 2.8 and 2.9 yields the plot in figure 2.16. In comparison to the resistive losses of non-ferrous metals that were presented in figures 2.11 and 2.12, a significantly greater margin between the AC and DC resistance values is possible even for wire diameters in the range of 100–200 μm, dimensions typical of filars employed in commercially available implant leads. Further work is needed to determine if such filars would reach a state of magnetic saturation and become ineffective within the strong magnetic field of an MRI machine.

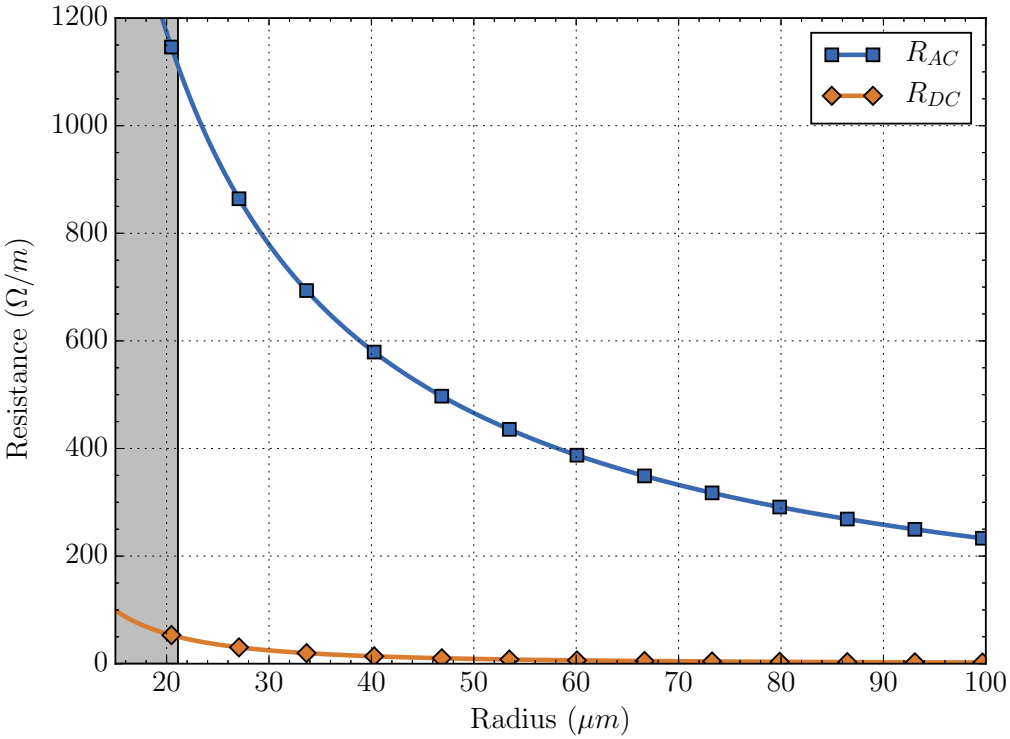

Figure 2.16: *The AC and DC resistance for a solid Nickel wire over a range of radii. The skin depth at* 128 MHz *is* 0.48 µm*. The shaded region is where the DC resistance exceeds the* 50 Ω/m *limit.*

Chapter 3

Validation by Measurements in an MRI Machine

The following manuscript builds upon previously simulated findings and provides thermometry measurements of test leads undergoing scans in a commercial 3 T MRI machine. Simulations were repeated with revised dimensions to match those of the leads under test. Consequently, validation of the simulation model could be carried out. Thin lead insulation is then put to the test.

3.1 "Electromagnetic Techniques to Minimize the Risk of Hazardous Local Heating around Medical Implant Electrodes during MRI Scanning"

Steven McCabe[1], Jonathan Scott[1], and Stephen Butler[2]
[1]Department of Engineering, The University of Waikato, Hamilton, New Zealand
[2]Midland MRI, Hamilton, New Zealand

Published in the *Proceedings of the European Microwave Conference (EUMC 2015)*, Paris, 7–10 Sep. 2015, pp. 702–705.

The co-authorship form is provided in appendix A.

3.1.1 Abstract

Magnetic Resonance Imaging (MRI) scans are contraindicated for many patients with medical implants. We establish the circumstances that cause, and the resistances required to ameliorate and to eliminate dangerous levels of MRI-induced heating that occur at the exposed, distal end of an electrical lead implanted in tissue. Simulated predictions are compared with measurements made at 128 MHz in a 3-Tesla MRI machine. A low resistance at kilohertz frequencies is sought by implant makers, in contrast with the high resistance demanded for safety. The practicality of presently-developed strategies to prevent tissue damage is brought into question. We examine the extent to which skin-depth and transmission-line properties can be manipulated to improve safety.

3.1.2 Introduction

The strong magnetic field present in a Magnetic Resonance Imaging (MRI) machine presents a hazard, as most people know. Nevertheless, it is the energy

delivered by the high-power RF field that is of greater concern for the patient. A 3-Tesla (3 T) MRI machine can deliver peak pulses in the order of 30 kW at 128 MHz. [40] This can lead to significant heating of the patient. The International Commission on Non-Ionizing Radiation Protection (ICNIRP) recommends maximum localized temperatures of 38 °C in the head and 39 °C in the torso, representing 1–2 °C of heating. [8] The dielectric heating of a patient is monitored by the Specific Absorption Rate (SAR), the power absorption per unit mass. The SAR is typically averaged over the whole-body, whole-head, or 10 g of mass.

The leads associated with medical implants can behave as antennas and concentrate the RF field. [6] We will show that this phenomenon is worst when the lead is just short of one-half wavelength long, about 250 mm for a typical lead in standard saline in a 3 T machine. There are claims in the literature that 10 g is too coarse near implants [9], and we confirm and exemplify this. While pacemakers have short leads, Spinal-Cord Stimulation (SCS) and Deep-Brain Stimulation (DBS) systems have leads that can exceed 600 mm in length because the implant is situated in the abdomen or chest cavity, far from the distal end of the electrode.

The MRI safety of implants has become a global issue and sites such as "Shellock" [10] are consulted throughout the world by MRI radiologists. Many implant-wearers are contraindicated for MRI scans. There is a growing need to address this problem. A spate of patents appeared in the last decade supposedly addressing the issue [7], [11]–[14], [17]. Only one product has appeared and it is rated for use only in 1.5 T machines, and only with a restricted scanning protocol. [16]

3.1.3 Impact of a Bare Wire

An implant lead wire acts as an "antenna in saline". In a lossless medium (conductivity $\sigma = 0$), an ordinary dipole antenna will resonate when excited by an RF field when its length is approximately equal to an odd integer multiple of the half-wavelength: 0.5λ, 1.5λ, 2.5λ, $\cdots$. In the conductive saline medium,

the wave will compress and the wavelength becomes [20]:

$$\lambda = \sqrt{\frac{8\pi^2}{\omega^2 \mu \epsilon}} \cdot \left[\sqrt{1 + \left(\frac{\sigma}{\omega \epsilon} \right)^2} + 1 \right]^{-1/2} \tag{3.1}$$

where ω is the angular frequency, and μ and ϵ are the permeability and permittivity of the medium, respectively. Furthermore, the induced antenna currents are not confined by the ends of the wire and are free to extend into the medium. [21] The antenna will be effectively lengthened by the medium itself.

This situation leads us to expect heating to occur at the ends of a wire when stimulated at a frequency slightly below that at which the lead wire is one-half wavelength long. To confirm this expectation we simulate using COMSOL Multiphysics 4.4 with a phantom model set according to ASTM F2182-11a [19] with the exception of the length parameter, which is doubled from 0.6 m to 1.2 m, to accommodate the testing of longer length wires. For simulation details refer to [41].

Fig. 3.1 shows the simulated field at the end of a bare wire embedded in a human-body phantom and exposed to a calibrated SAR of 1 W/kg against

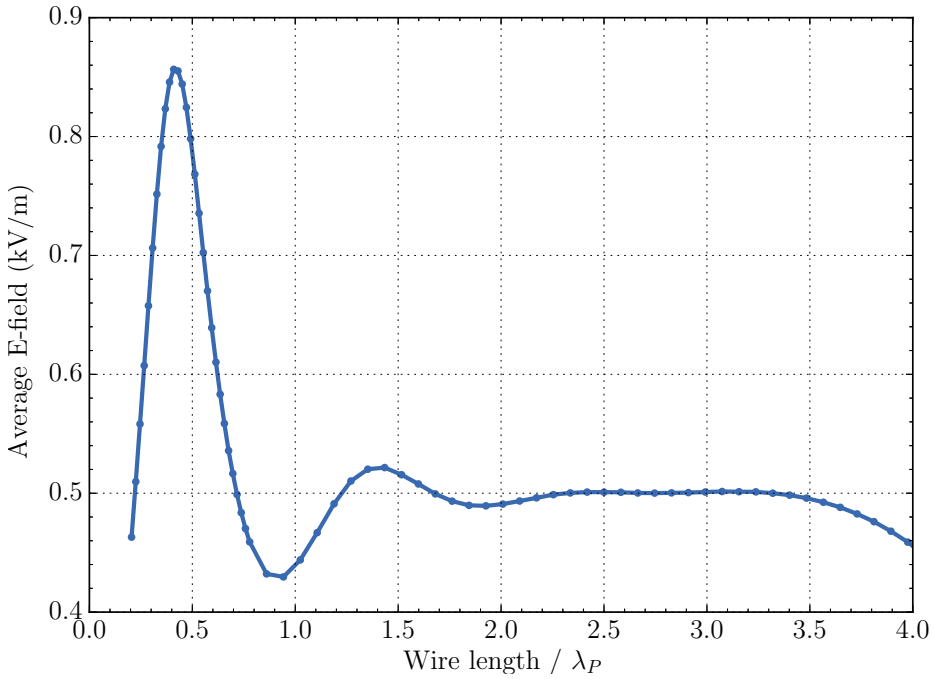

Figure 3.1: *Average E-field at one end of a* 800 µm *diameter bare wire for various lengths in a lossy phantom* ($\sigma = 0.47\,\mathrm{S/m}$) *to model a human body. The wire length is normalized to a wavelength of* 0.24 m.

length normalized to the wavelength via (3.1). Simulation confirms a strong resonance at $0.41\lambda_P$, confirming theoretical expectation.

3.1.4 Impact of Insulated Wire with Distal End Exposed

Now we consider a wire with insulation covering all but one end, representing an implant's distal electrode. The average electric field near the distal electrode at various wire lengths is in Fig. 3.2. The length is normalized to $\lambda_{Pn} = 0.61\,\mathrm{m}$ and the first resonant peak occurs at $0.41\lambda_{Pn}$. The insulation shifted the resonant frequency and it has also increased the electric field intensity at the first resonant peak threefold.

The change in temperature ($T - 37\,^\circ\mathrm{C}$) at the distal electrode of the insulated wire after 5 min of MRI scanning is considered next. The result with and

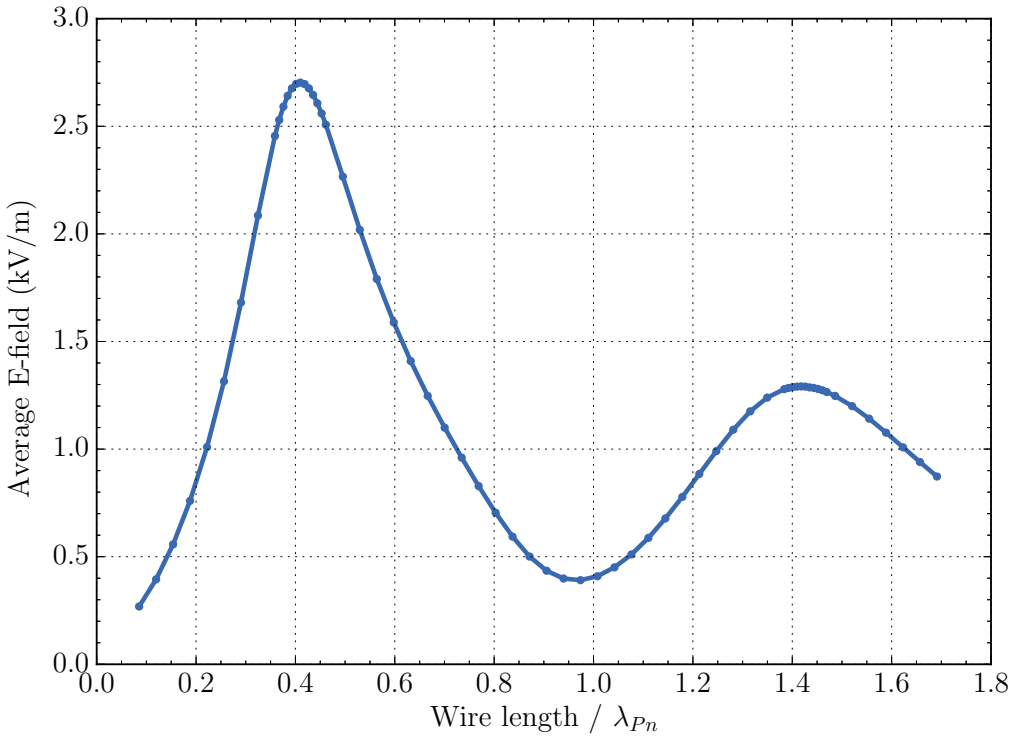

Figure 3.2: *Average E-field at the distal electrode of an insulated wire in a lossy phantom ($\sigma = 0.47\,\mathrm{S/m}$). The insulation covering the 800 µm diameter wire is 350 µm thick. The wire length is normalized to a wavelength of 0.61 m.*

without blood perfusion is shown in Fig. 3.3, again with the x-axis normalized to the wavelength of the electric field within the phantom, λ_{Pn}.

The inclusion of blood perfusion provides an approximation to living human tissue, reducing the heating by 18% at the worst-case length. At $0.41\lambda_{Pn}$ (0.25 m), normal body temperature is exceeded by almost 22 °C, well over the 2 °C limit for SCS. The peak temperature declines at longer wire lengths but still mostly exceeds safety limits. A two-dimensional slice of the temperature T in the x-z plane at $y = 0$ is shown in Fig. 3.4, for a wire length of $0.41\lambda_{Pn}$. This figure makes it clear that a sample size of 10 g is indeed too coarse for estimating SAR—10 g is a sphere of one inch diameter, large compared to the hot region of the plot.

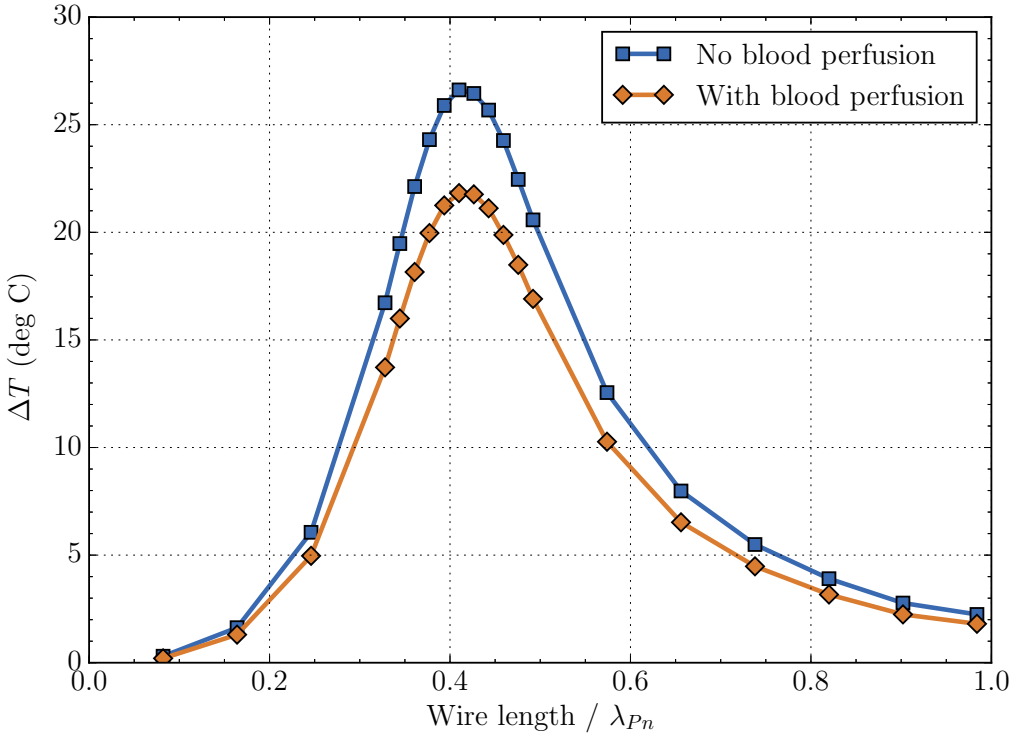

Figure 3.3: *The change in temperature ΔT near the distal electrode of the insulated wire after 5 minutes of simulated scanning. The insulation covering the* 800 µm *diameter wire is* 350 µm *thick. The length of the wire is normalized to a wavelength of* 0.61 m.

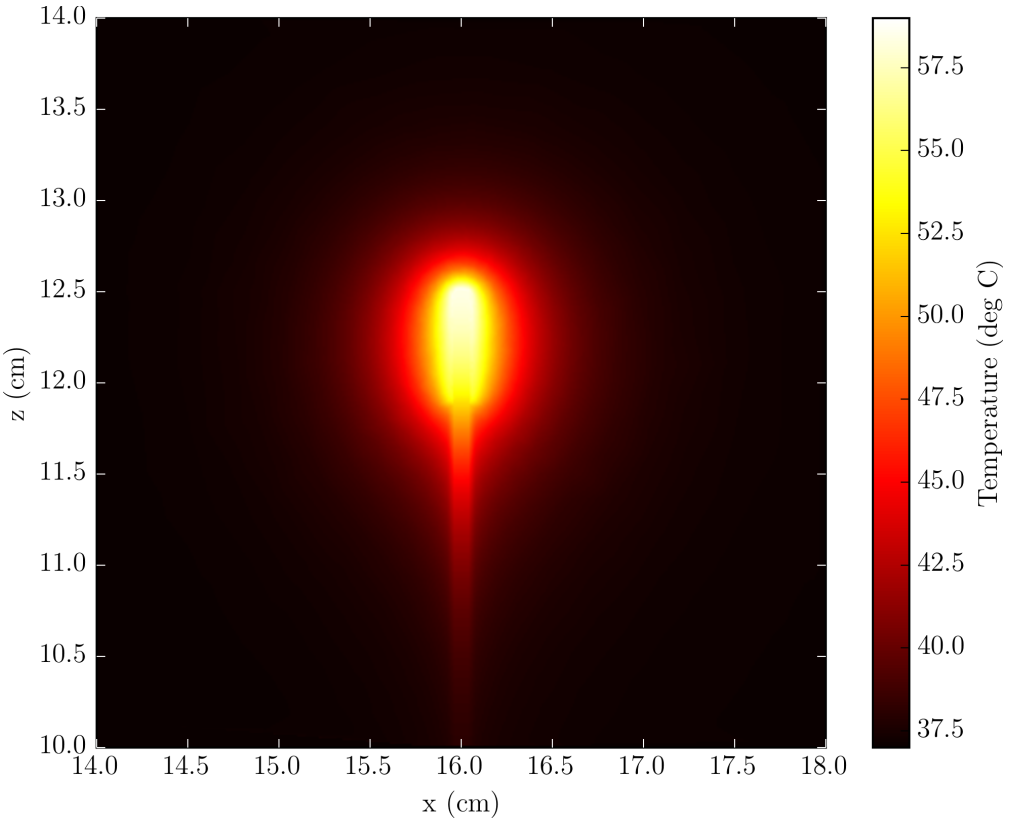

Figure 3.4: *The worst-case $T(x, z)$ at the distal electrode after 5 minutes of simulated scanning. The wire length was $0.41\lambda_{Pn}$ and blood perfusion was included. The initial temperature was* 37 °C.

3.1.5 Comparison with Measured Values

In order to have confidence in our simulations, a torso-and-head phantom after [19] was built in clear acrylic and filled with 28 L of saline gel with a conductivity of 0.47 S/m. The ratio of NaCl and polyacrylic acid (PAA) to distilled water was 1.32 g/L and 10 g/L, respectively. Wire samples in the phantom were tested within a commercial 3T MRI scanner. Fig. 3.5 shows the phantom on the MRI machine bed.

Temperature was measured using an Optocon Fotemp GaAs-based fiber-optic system with TS2 probes. Fig. 3.6 depicts a temperature sensor tip aligned with the exposed tip of an 800 µm Cu wire of length 0.41λ, coated with 350 µm of plastic insulation.[5]

[5]Optocon say that the "final few millimeters" of the probe is the active sensing region. Our experience suggests that the temperature of the last 1 mm of the probe tip contributes to the reading. We have chosen to align the probe and sample wire, as shown in figure 3.6, such that the sensitivity is optimised.

Figure 3.5: *Clear acrylic phantom on the bed of the MRI machine with operator.*

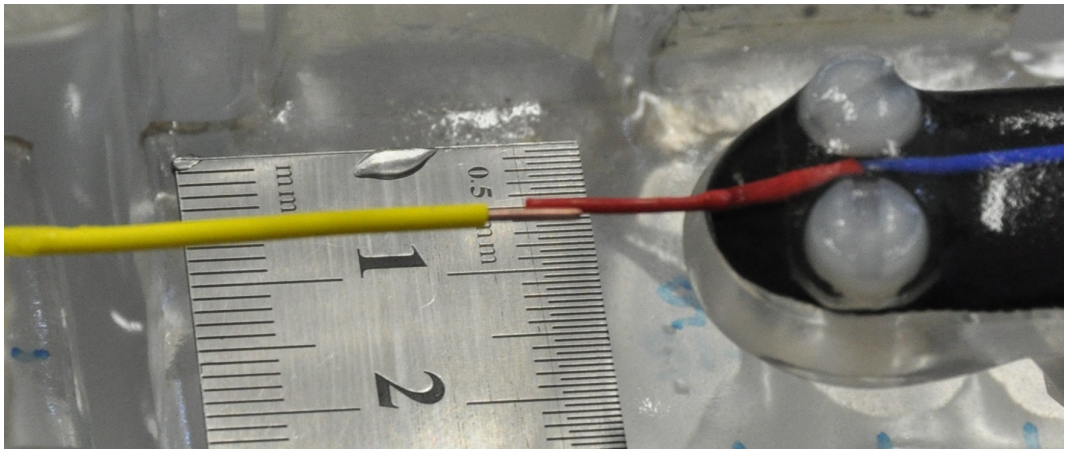

Figure 3.6: *Photograph of the Optocon TS2 probe (red) aligned alongside the bared end of the insulated wire sample (yellow). Scale is in centimeters. An adjustable mechanism supports the TS2 probe and holds it in position.*

The temperature rise after 5 minutes of MRI scanning was recorded for various lengths of insulated wire. The insulation was 350 µm thick, but thinner and thicker variants were also tested. The measurements are shown in Fig. 3.7 with simulated data overlaid. We measure a temperature rise of 7.9 °C near the worst-case length, with an estimated whole-body SAR of 2.7 W/kg. We scale our measurements by 2.7 times to account for the conservative SAR estimate reported by the MRI machine. This corresponds to a rise of 21.3 °C

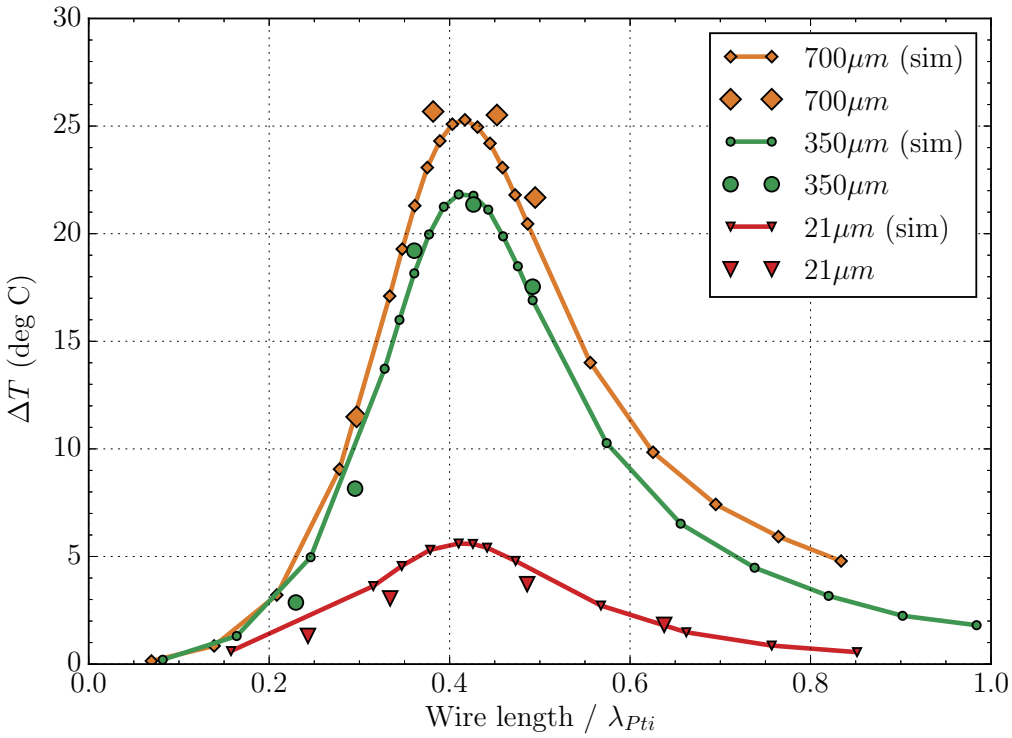

Figure 3.7: *The change in temperature ΔT near the distal electrode for three types of insulated wires, varying by insulation thickness, after 5 minutes scanning. Simulated data is verified by several measurements about the resonant peaks. The x-axis is normalized individually for each insulation type, such that the peaks occur at $0.41\lambda_{Pti}$. The respective wavelengths are $\lambda_{P700} = 0.72\,\mathrm{m}$, $\lambda_{P350} = 0.61\,\mathrm{m}$, and $\lambda_{P21} = 0.32\,\mathrm{m}$.*

for a whole-body SAR of 1 W/kg. Similar wire with double the thickness of insulation produces almost 25.7 °C, while just 21 µm of insulation produces only 3.7 °C, consistent with our expectations in section 3.1.8.

3.1.6 Impact of Wire Resistance

Implant manufacturers seek a low resistance connection to the electrodes to minimize the voltage required to deliver therapeutic current and maximize battery life. An SCS implant typically delivers a maximum current of 10 mA. A resistance of 50 Ω/m is desirable, double that barely comfortable.

A reduction in the heating of the tissue near the distal electrode could be achieved with uniformly distributed resistance in the implant wire. Three-

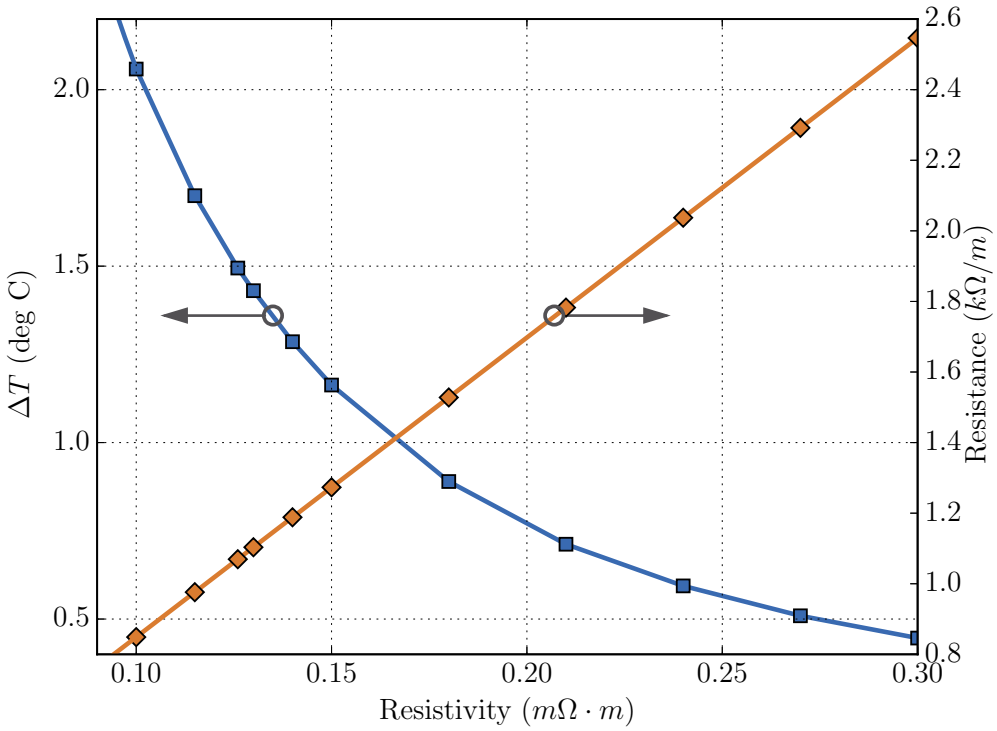

Figure 3.8: *The change in temperature ΔT near the distal electrode after* 5 min *of simulated scanning for various amounts of uniform wire resistance. The insulation is* 350 µm *thick. The linearity between the resistance and resistivity confirms that the skin depth is sufficiently larger than the metal thickness, such that the current is uniform.*

dimensional simulations of a hollowed out version of the implant wire with 350 µm of insulation were performed. The resistance was varied by controlling the resistivity of the metal. To ensure current uniformity, the resistivity was constrained to values such that the skin depth exceeded the thickness of the metal by at least 10 times. The resistance at 128 MHz and the temperature change after 5 min as a function of the metal resistivity is shown in Fig. 3.8. A 2 °C limit would require >850 Ω/m of resistance. The significant benefit of a factor of two would require >200 Ω/m.

3.1.7 Impact of Skin Effect

Is it possible to select values for the radius r and resistivity ρ of the wire such that the skin effect provides high enough resistance at 128 MHz and low enough at dc? Skin depth $\delta \approx \sqrt{2\rho/\omega\mu}$ [22], about 14.5 µm for Pt. Resistance

of a wire $R = \rho/A\ \Omega/\mathrm{m}$, where A is effective cross-sectional area. For dc, $A = \pi r^2$, but smaller for increasing frequency, and approximated as $2\pi r\delta$ if $r \gg \delta$. It is clear that dc resistance is inversely proportional to r^2 and to first order ac resistance to r. Thus larger r will give a larger ratio of ac to dc resistance, but falling total resistance. To have no more than $R_{dc} = 50\,\Omega/\mathrm{m}$ in Pt requires $r \gtrapprox 26\,\mu\mathrm{m}$. Simple approximations for the effective area fail since r is comparable to δ, but the Modified Lorentzian Method of [23] yields $R_{ac} = 59\,\Omega/\mathrm{m}$. Results are the same for all metals (ratio does not scale with ρ). Long before ac exceeds dc resistance sufficiently, both become quite small. [41] Skin depth may help, but it cannot deliver the required ratio.

3.1.8 Impact of Insulation Properties

Varying the thickness, t_i, and the dielectric constant, ϵ_r, of the insulation leads to the results shown in Fig. 3.7 and Fig. 3.9. These results can be understood by realizing that an implanted lead wire resembles a coaxial transmission line

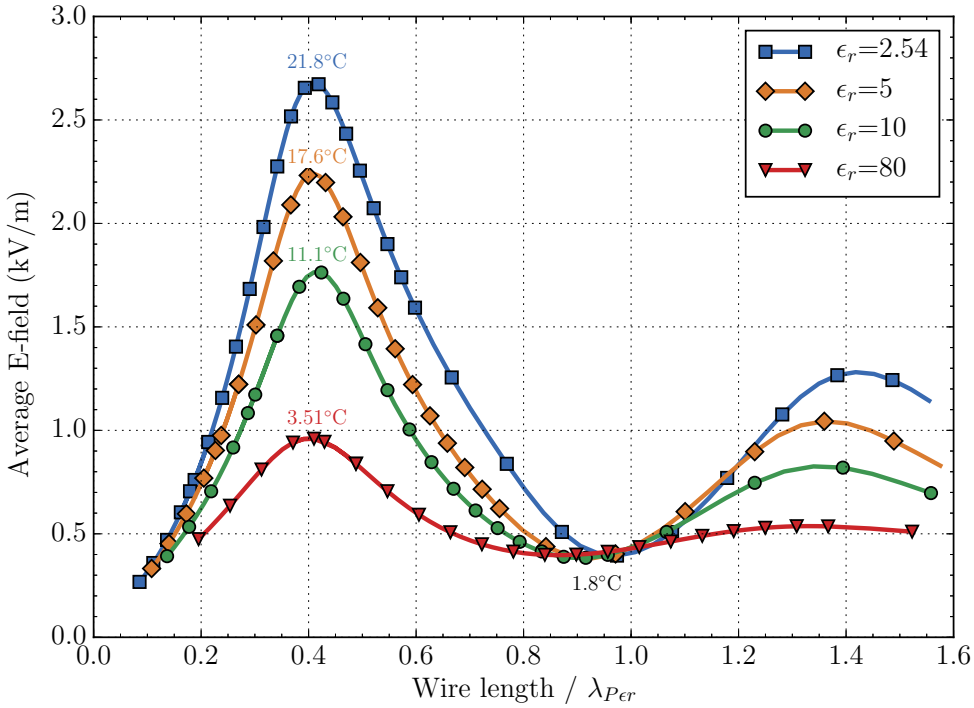

Figure 3.9: *Average E-field at the distal electrode for various insulation permittivities when $t_i = 350\,\mu\mathrm{m}$. Several values for ΔT (simulated) are overlaid. The x-axis is normalized individually for the different traces.*

but with conductive tissue representing the outer cylindrical conductor. [24] The ideal characteristic impedance of a uniform coaxial transmission line is

$$Z_0 = \frac{1}{2\pi}\sqrt{\frac{\mu}{\epsilon}} \cdot \ln\left(\frac{r_2}{r_1}\right) \tag{3.2}$$

where r_1 and r_2 are the radii of the inner and outer conductors, and μ and ϵ are the absolute permeability and permittivity of the dielectric material, respectively. Its Z_0 affects the amount of RF energy that is coupled to the implant lead wire. It is clear that thin insulation, while potentially not practical for reasons of durability, offers a significant advantage. An insulation with a high dielectric constant will also help.

3.1.9 Conclusion

We explain the mechanism behind the hazard presented by implant electrodes, and confirm that 10 g is too coarse a sample over which to average exposure. Simulated and measured results agree. We have established lead resistance values required to reduce or eliminate the heating hazard at 128 MHz, and to preserve SCS implant battery life for low-frequency signals. We show that the skin effect alone is unable to provide the impedance difference. We show that manipulation of the insulation properties can lower peak distal heating by a large extent. In combination with other techniques that we are not free to disclose at this time [42], can be expected to lead to an MRI-safe electrode design.

3.1.10 Acknowledgement

We would like to thank the Waikato Medical Research Foundation (WMRF) for funding. We also acknowledge WaikatoLink and KiwiNet for their valuable support.

3.2 Further Results and Discussion (Unpublished)

3.2.1 Specific Absorption Rate

The absorption of RF energy into a patient undergoing an MRI scan is monitored by the Specific Absorption Rate (SAR), an amount averaged over the whole-body or localised regions for a specified time, expressed in W/kg [43]. Control of this parameter is necessary for minimising tissue heating, a concern even for non-implant wearing patients. Induced eddy currents form in the conductive tissue and exhibit ohmic loss[6] [43]–[45]. Regulatory agencies [8], [46], [47] recommend the whole-body SAR be limited to less than 3–4 W/kg depending on circumstance and a local SAR of no more than 10 W/kg, to minimise the likelihood of neural tissue being subjected to heating higher than 1–2 °C over a specified time period[7].

Estimation of the whole-body SAR is based on the amount of power delivered in the volume of the transmit coil to the patient of a given weight. On the other hand, estimation of the local SAR is usually based on a sample size of 10 g and is therefore less straightforward to measure. It relies on complex computational models that accurately represent the anatomy of the patient as well as the highly inhomogeneous RF fields distributed within the patient's body from MRI. For this reason, local SAR is rarely monitored during a patient scan.

As medical implants can generate highly concentrated SARs during MRI, hot spots can go undetected. This was shown by the simulation in section 3.1.4 where the whole-body SAR was set to a moderate 1 W/kg, and yet localised heating occurred and greatly exceeded safety limits within a 5 minute scan. The size of the hot spot was less than a centimeter in diameter or 0.5 g of mass, as approximated using the formula for the volume of a sphere and $V = m/\rho$:

$$m = \frac{4}{3}\pi r^3 \rho \tag{3.3}$$

[6]The term "dielectric heating" was incorrectly referred to in the EuMC paper to describe what is in fact Joule heating.

[7]Some leeway may be given to peripheral regions of the body and other tissue types, where heating can acceptably reach higher limits for short durations.

Since accurate detection of SAR over such miniature volumes is not possible, only implants that have been rigorously tested and rated safe or conditionally safe for MRI, either by the implant manufacturer and/or a recognized medical institute such as [10], can be safely scanned.

3.2.2 Measured Heating

The average heating of a test phantom in the absence of an implant can be estimated by:

$$\Delta T = \frac{\mathrm{SAR}\,\Delta t}{C} \tag{3.4}$$

where $C = 4150\,\mathrm{J/(kg\,K)}$, the specific heat capacity of the phantom material. With a whole-body SAR $= 1\,\mathrm{W/kg}$ and $t = 300\,\mathrm{s}$, an average temperature rise of less than $0.1\,^{\circ}\mathrm{C}$ is expected. This is consistent with measurements made in a 3T MRI machine as is depicted in figure 3.10. This background temperature rise can be considered negligible when compared to the measured distal electrode heating of a long test lead as is shown in the same figure. Refer to appendix B for details of the MRI machine and thermometry apparatus.

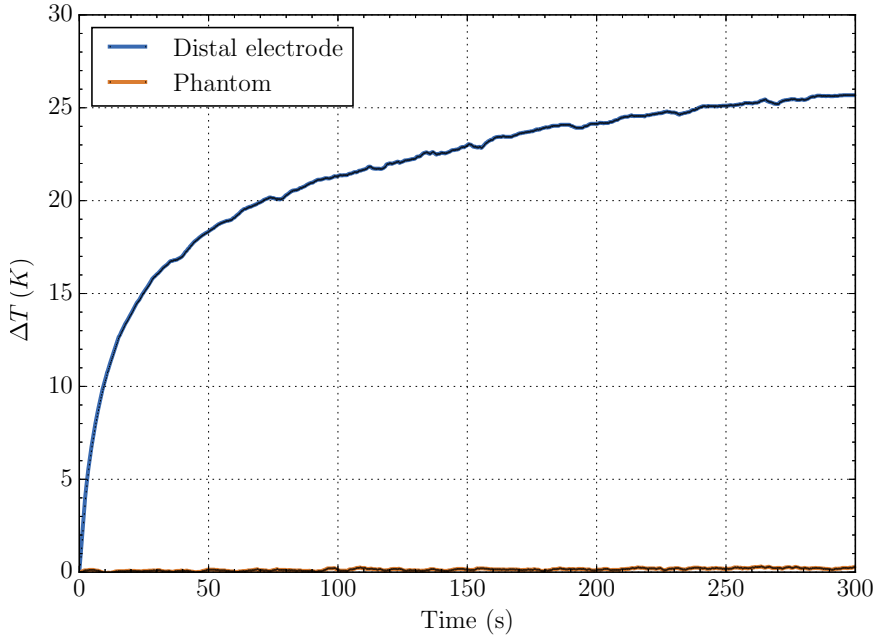

Figure 3.10: *The change in temperature ΔT measured during a 3T MRI scan at the distal electrode of an insulated wire* 27 cm *in length, with* 700 μm *of insulation. The ambient temperature of the phantom was monitored with a temperature probe located on the opposite side of the phantom. Temperature readings were acquired with a sample rate of* 4 Hz *and averaging set to 20 times.*

3.2.3 Thinsulation

Implant leads incorporating filars with thin insulation of a few tens of microns in thickness, hereinafter referred to as *Thinsulation*, experience less distal heating than those with thick insulation as was shown in section 3.1.5. This is because thinner insulation has a lower impedance between the filar and the surrounding tissue and therefore reduces the filar's ability to store and transfer charge to the distal electrode. Increasing the insulating material's permittivity has an equivalent effect.

Calculation of the capacitive reactance of simple single-core test leads can be approximated using $|X_C| = 1/\omega C$ and the formula for the capacitance of a coaxial cable:

$$C = \frac{2\pi\epsilon l}{\ln(r_2/r_1)} \tag{3.5}$$

A 1 m long wire with 21 µm of insulation will have twelve times less capacitive reactance than the amount for the same wire having 350 µm of insulation as is shown in table 3.1. While helpful in shunting MRI-induced RF currents, Thinsulation will also shunt normal neurostimulation currents in the kilohertz range. For example, a typical pulse generated by an SCS neurostimulator is 8 V at 10 mA ($Z = 800\,\Omega$) [48]. An insulation thickness of just 21 µm or less will start to alter the shape and amplitude of the pulse and therefore impact the effectiveness of the stimulation therapy. One workaround would be to use a combination of filars with thin and thick insulation, a concept that is described in detail in chapter 9.

Table 3.1: *Estimated capacitive reactance of the test wires from section 3.1.5.*

	1.5 kHz	**10 kHz**	**128 MHz**
21 µm	38 kΩm	5.8 kΩm	0.45 Ωm
350 µm	470 kΩm	71 kΩm	5.5 Ωm
700 µm	760 kΩm	110 kΩm	8.9 Ωm

3.2.4 Surface-Roughened Filars

Conductors with rough surfaces exhibit greater RF loss than those with smooth surfaces [49]–[51]. It was alluded to in section 3.1.9 by reference to the patent

in [42], that purposely roughened filars may gain substantially higher AC resistance than is possible with regular filars of equivalent dimensions. A distribution of deep pits or fissures, one to several skin depths in magnitude along the filar length, is most desirable for maximising loss [50].

Microscopic roughening of a metal surface can be achieved using various methods. These include abrasion from sandpaper [52], mechanical manipulation to induce cracking from fatigue [53], chemical etching [54], [55], degradation from electrolysis [56], corrosion [57], and the application of an additional porous conduction layer through electrodeposition [50]. An example of a chemically roughened 20 μm gold wire is in figure 3.11. Formations of small 1 μm valleys traversing along the length of the wire are visible.

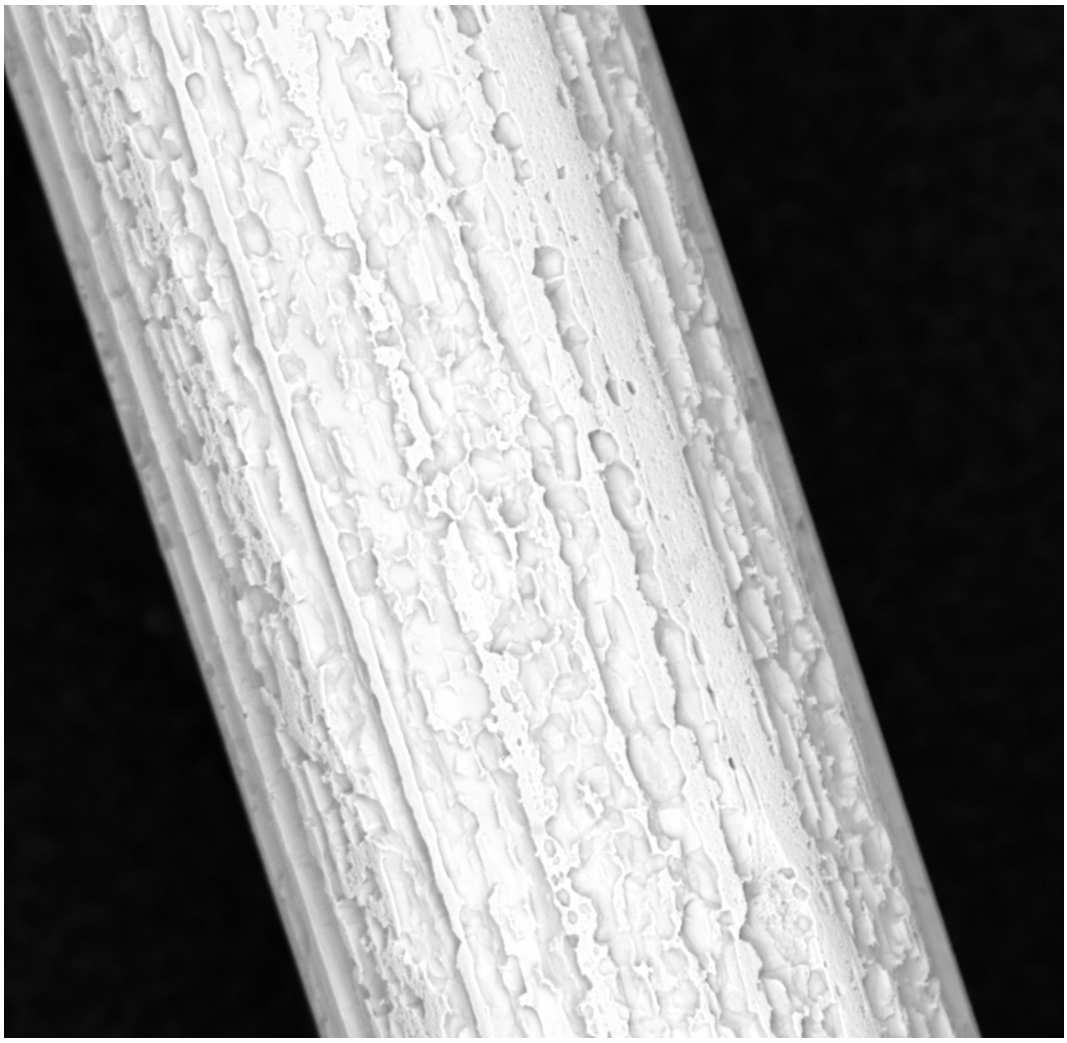

Figure 3.11: *View of a chemically etched 20 μm Au wire, captured with an electron microscope. Etching was performed with the process described in [55] using iodine and potassium iodide.*

Modeling the electromagnetic behaviour of a roughened implant filar in an MRI machine is difficult. The microscopic structure of the roughness in relation to the birdcage antenna demands excessively high numbers of meshing elements in order to define the geometry sufficiently. Hence, the amount of computing power and time required becomes impractical. For this reason, investigation by measurement is the preferred method.

As a proof of concept, measurements of insertion loss at 128 MHz were made on the wire from figure 3.11 using the apparatus in figure 3.12 and a network analyser. The skin depth of gold δ_{Au} at this frequency is about 6.9 μm. No measurable loss attributable to the roughened surface was observed when comparing to that of an equivalent non-roughened wire. This is expected since the skin depth is large relative to the roughness and is comparable to the radius of the wire.

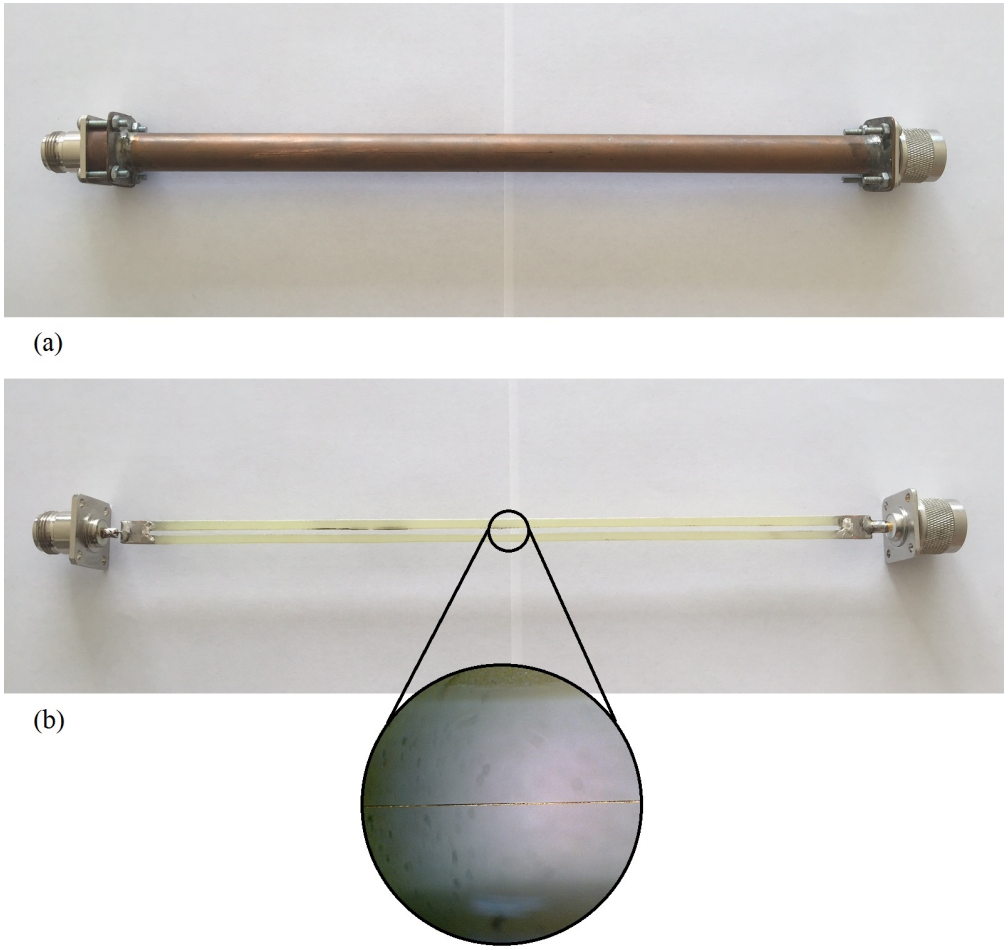

Figure 3.12: *(a) Two-port coaxial waveguide. (b) Copper tube removed to show wire sample suspended between N-type connectors. Insertion loss is measured with a network analyser.*

Recent work in [58] used a similar configuration to test the insertion loss presented by smooth and roughened 4.8 mm diameter copper rods. Mechanical roughening of depths up to $2.5\delta_{Cu}$ was applied with sandpaper. Similarly, little increase in the insertion loss was apparent, concluding that little improvement to the RF safety from MRI was likely to be gained by roughening implant filars.

So far testing has been limited to the insertion loss of single bare conductors suspended within coaxial waveguides. Further work is needed to determine the impact of wire diameter with respect to the skin depth, the geometry and depth of the roughened surface, and the presence of a dielectric with $\epsilon_r > 1$. Roughened magnetic wire may offer some benefit, according to equation 2.8. For example, wire made from Nickel would have a skin depth of just 0.5 μm at 128 MHz, enabling electrolysis methods of roughening such as Ottenisation [56], where such processes can only generate small fissures of about 1–2 μm in depth [59]. Surface roughening also has the effect of increasing the effective surface area of a conductor, a property which could improve the performance of decoy filars, a topic that is discussed in more detail in chapter 6. Lastly, measurements should be performed under MRI conditions and in a phantom. The static magnetic field from the MRI machine may have a significant influence on the skin effect that is otherwise unnoticed when testing plain low impedance lead filars. Refer to section 8.3 for patent details.

Chapter 4

Measurements in the Laboratory

A lab-based technique was devised for measuring the peak heating of implant leads without requiring an MRI machine for excitation. This enabled rapid prototyping of implant lead designs. The following manuscript describes the technique and compares measurements with those previously obtained in the 3T MRI machine.

4.1 "Technique to Assess the Compatibility of Medical Implants to the RF Field in MRI"

Steven McCabe and Jonathan Scott
Department of Engineering, The University of Waikato, Hamilton, New Zealand

Published in the *Proceedings of the Asia-Pacific Microwave Conference (APMC 2015)*. Nanjing, 6–9 Dec. 2015, pp. 1–3.

The co-authorship form is provided in appendix A.

4.1.1 Abstract

The standard technique for determining the compatibility of medical implants to the magnetic and RF fields present in Magnetic Resonance Imaging (MRI), requires access to an MRI machine. For implants comprising metals of mostly the non-ferrous kind, it is only the RF field of an MRI machine that is of concern. Implant electrodes can concentrate the RF field in the surrounding tissue and give rise to joule heating. The inherent design of Spinal Cord Stimulators (SCS) and Deep Brain Stimulators (DBS) makes these implants particularly susceptible to hazardous levels of RF heating. We propose a technique that offers a quick and indicative assessment of the compatibility of implant leads to the RF field in 3-Tesla MRI, without needing access to an MRI machine. A dipole antenna, driven by a power amplifier and Continuous Wave (CW), injects RF energy into a gelled saline phantom. The heating in the gel near a test implant electrode is monitored with a fiber optic thermometer. The results are calibrated against measurements made in a 3-Tesla MRI machine.

4.1.2 Introduction

Many implants in the world today contraindicate patients from having Magnetic Resonance Imaging (MRI) scans. Even when comprised of completely non-magnetic materials, an implant can be hazardous to a patient undergoing

an MRI scan. In a 3 T MRI machine, the amount of peak RF power necessary to sufficiently detect hydrogen atoms within the patient can exceed 30 kW at 128 MHz. [40] Normally, a patient free of implants will experience only minimal heating from the generated eddy currents in the tissue. [6] Presence of an implant however, especially one with long lead conductors, can cause significant localised joule heating in excess of 25 °C in the tissue near the distal electrodes. [60] This is well over the 1–2 °C safety threshold recommended by the International Commission on Non-Ionizing Radiation Protection (ICNIRP) in [8]. The long leads used in Spinal Cord Stimulators (SCS) and Deep Brain Stimulators (DBS) make these systems inherently unsafe for MRI. As a result, engineers are developing MRI-safe leads. [42]

The F2182-11a international standard is a test method for assessing the RF safety of medical implant leads in a 1.5 T–3 T MRI machine. [19] Since there is a dependency of heating as a function of lead length, multiple tests are needed to determine the worst-case length. Variation in the insulation thickness, insulation permittivity, or wire diameter, will influence the length at which the resonant effect takes place.

The development of leads becomes difficult when access to an expensive MRI machine is restricted. Computer modeling with electromagnetic simulation software can aid the design process. [41] However, with long simulation times even for overly simplified models, this approach can be impractical when quick indicative assessments are needed. To address this problem, we have developed a simple measurement technique that employs a small dipole antenna in place of the MRI machine to induce heating near the implant under test. Implant leads can be quickly tested and compared in the lab, without the set-up and running costs associated with an MRI machine.

4.1.3 RF Heating

An implanted lead acts as a "receiving antenna in a lossy medium". [6] An ordinary dipole antenna situated within a lossless medium (conductivity $\sigma = 0$), will resonate when excited by an RF field when its physical length is approximately equal to an odd integer multiple of the half-wavelength: 0.5λ, 1.5λ, 2.5λ, $\cdots$. In a conductive medium, the antenna currents are no longer con-

fined to the conductor and are free to flow into the medium. [21] Previous works have shown the resonance to occur when the bare conductor length l is about $0.41\lambda_P$. [41], [60] The wavelength λ_P in the medium is given by [20]:

$$\lambda_P = \sqrt{\frac{8\pi^2}{\omega^2\mu\epsilon}} \cdot \left[\sqrt{1+\left(\frac{\sigma}{\omega\epsilon}\right)^2}+1\right]^{-1/2} \tag{4.1}$$

where ω is the angular frequency, and μ and ϵ are the permeability and permittivity of the medium, respectively. At 128 MHz in human tissue, $\lambda_P \approx 0.24$ m. At the lowest mode of resonance, i.e. $l = 0.41\lambda_P$, peak heating occurs near the ends of the wire. Insulating the conductor with a dielectric material not only concentrates the heating to the tip if left bare, but has the effect of increasing the resonant length. Calculation is possible but limited to simple coaxial-like lead structures. [24] For this reason, the resonant length of an implant lead, $0.41\lambda_{Pn}$, is normally found by measuring the distal heating for various lengths of wire ≥ 0.10 m in an MRI machine, and looking for the peak.

Simulation of the induced MRI heating at the 6 mm bared end of an insulated wire with length $0.41\lambda_{Pn}$, was performed in COMSOL Multiphysics 4.4. The surrounding conductive medium representing human tissue was exposed to a 128 MHz circularly polarised field with a calibrated whole-body Specific Absorption Rate (SAR) of 1 W/kg. A two-dimensional slice of the temperature T in the x-z plane at $y = 0$ is shown in Fig. 4.1. With the heat localised very close to the electrode tip, careful placement of a temperature probe will be necessary to ensure consistency between measurements. For further simulation details refer to [41].

4.1.4 Dipole Experiment

The RF field in an MRI machine is circularly polarised and typically generated from a cylindrical birdcage antenna. [61] A dipole antenna produces only linearly polarised waves. Nevertheless, since the implant leads are rotationally symmetrical, and assuming the output power is calibrated, we expect the polarisation type to make little difference. We will compare our results with measurements in an MRI machine to confirm this expectation.

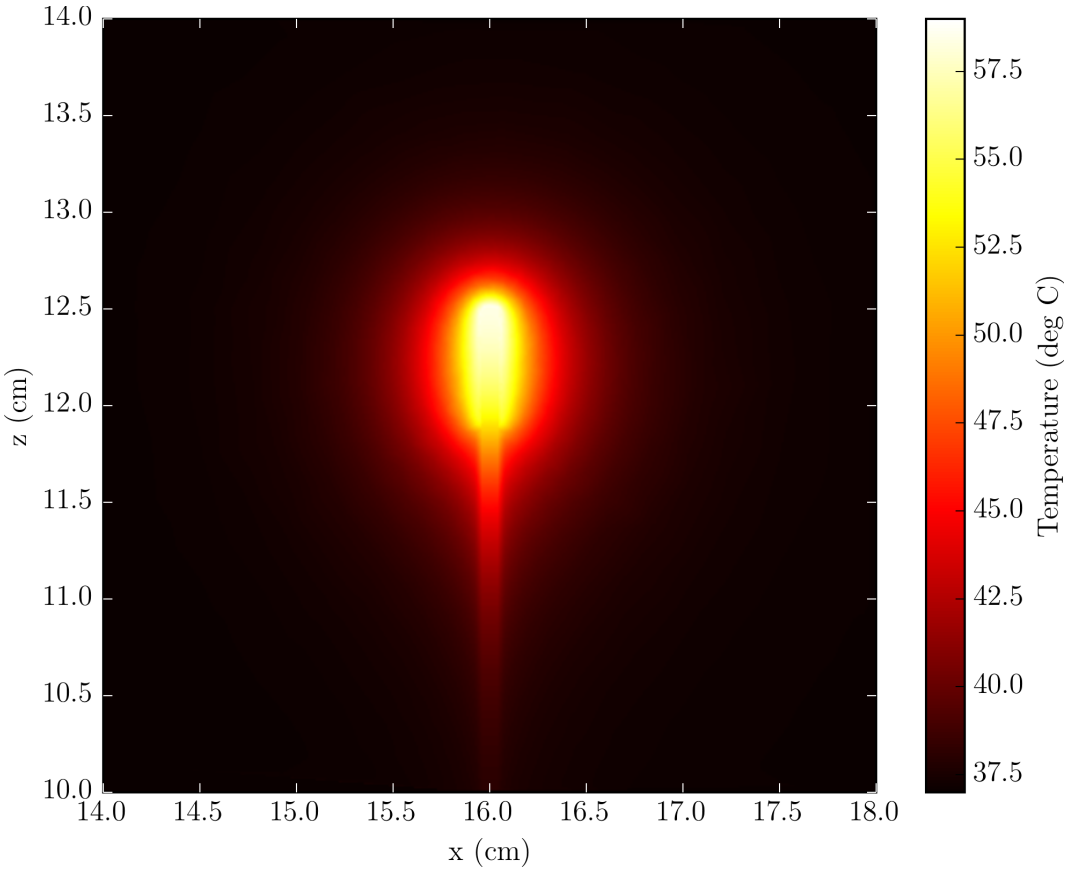

Figure 4.1: *The worst-case $T(x, z)$ at the distal electrode after 5 minutes of simulated MRI scanning. The wire sample had a length of $0.41\lambda_{Pn}$, a copper core diameter of* 800 µm*, and an insulation thickness of* 350 µm*. The phantom, with blood perfusion included in the model, had an initial temperature of* 37 °C*.*

A torso-and-head phantom after [19] was built in clear acrylic and filled with 28 L of gelled saline with a conductivity of 0.47 S/m. The ratio of NaCl and polyacrylic acid (PAA) to distilled water was 1.32 g/L and 10 g/L, respectively. A wire sample is suspended within the phantom alongside a completely insulated dipole antenna 6 cm away. The sample is positioned 5.5 cm from the phantom's left side, but centered longitudinally and vertically within the torso. The dipole of length 0.32 m is comprised of a 2.1 mm diameter copper wire with 350 µm of insulation. The S11 magnitude response as measured with an Agilent E8358A network analyser without the wire sample present, is shown in Fig. 4.2. Its impedance at 128 MHz is $(31.6 - 4.7\mathrm{i})\,\Omega$. A 30 W 50 Ω RF power amplifier with a 128 MHz input sine wave signal drives the antenna directly. An Optocon GaAs-based fiber-optic temperature probe with 0.1 °C resolution was aligned to the bared end of the wire sample as shown in Fig. 4.3.

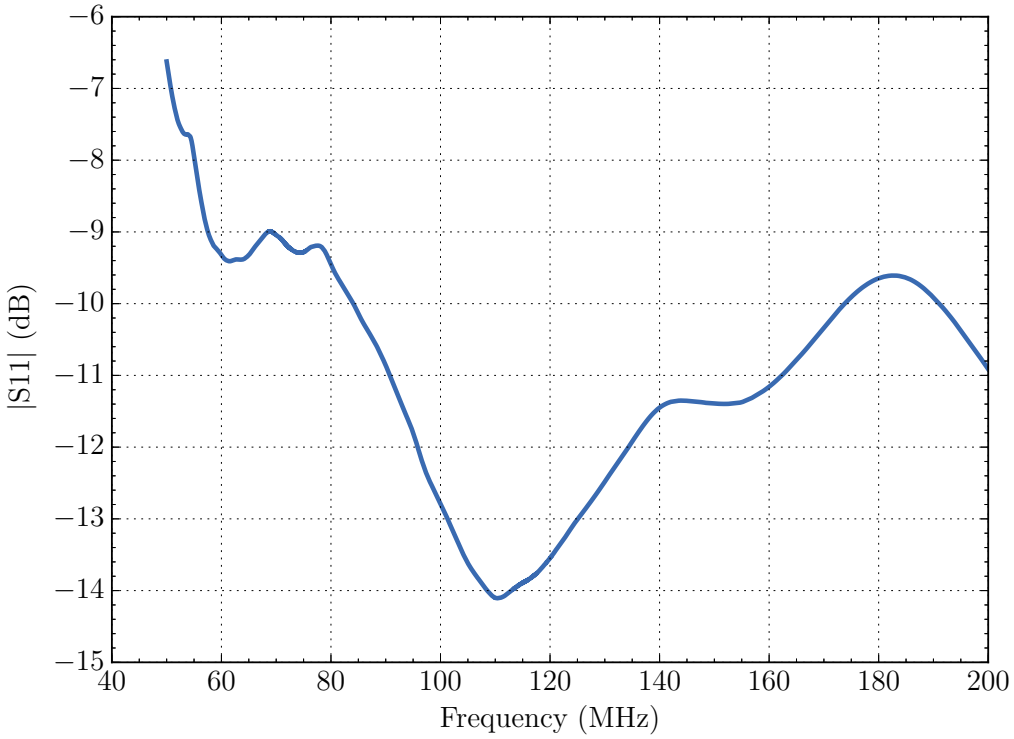

Figure 4.2: *Measured response of the insulated dipole antenna submersed within gelled saline, without the wire sample present. Resonance occurs close to the* 3 T *MRI frequency.*

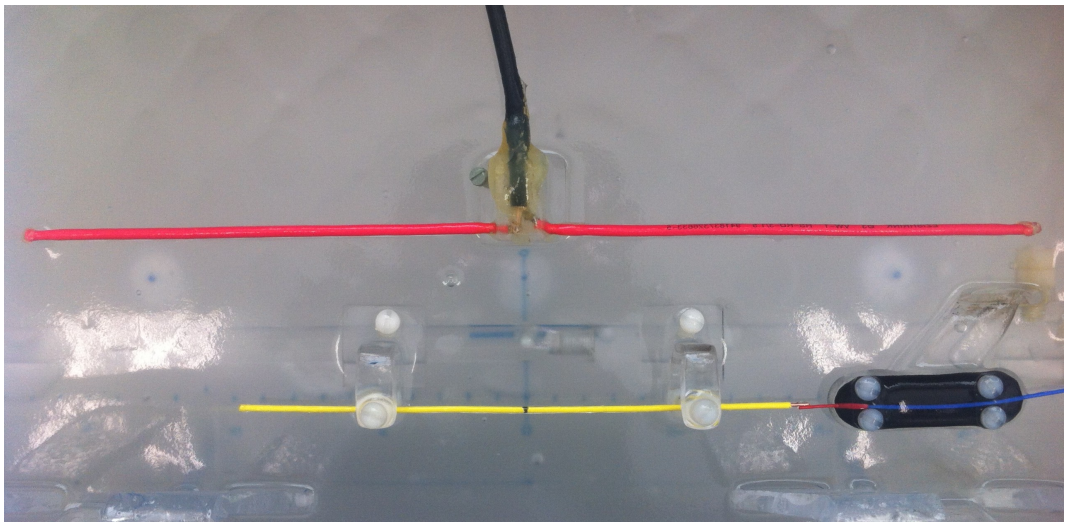

Figure 4.3: *A temperature probe is aligned at the bared end of the wire sample (yellow). The wire sample, held in place by adjustable support mechanisms, is a* 800 µm *diameter copper wire with plastic insulation covering all but the last* 6 mm *of one end. The dipole antenna (red) is situated* 6 cm *from the wire sample.*

4.1.5 Measured Results

Various wire samples were tested ranging by length and insulation thickness. Each sample consisted of a single copper core, 800 µm in diameter, with plastic insulation covering all but 6 mm from one end. Epoxy resin was applied to the opposing end. The change in temperature ΔT after 5-minutes of RF stimulus was recorded for each sample. To calibrate our measurements, we performed tests on 350 µm wire samples in a 3 T MRI machine. Fig. 4.4 shows the phantom on the MRI machine bed. The results for wire samples with 350 µm thick insulation are shown in Fig. 4.5. Simulated results of the wire sample excited by an MRI birdcage antenna are overlaid in the same figure.

We measure a temperature rise of 13.4 °C near the worst-case length when excited by the dipole. We calibrate our experiment by scaling the result by 1.5 times. This corresponds to a temperature rise of 20.1 °C for a whole-body SAR of 1 W/kg. The mutual coupling between the dipole antenna and the wire sample is evident near the resonant length, where there is a slight deviation away from the expected parabolic response. Nevertheless, the result is in agreement with simulations and measurements made in the MRI machine.

Wire samples with thinner insulation were measured in support of a patent being drafted at the time this manuscript became due for submission. The results are shown in Fig. 4.6. The x-axis is normalised for each trace such

Figure 4.4: *Clear acrylic phantom on the bed of the MRI machine with operator.*

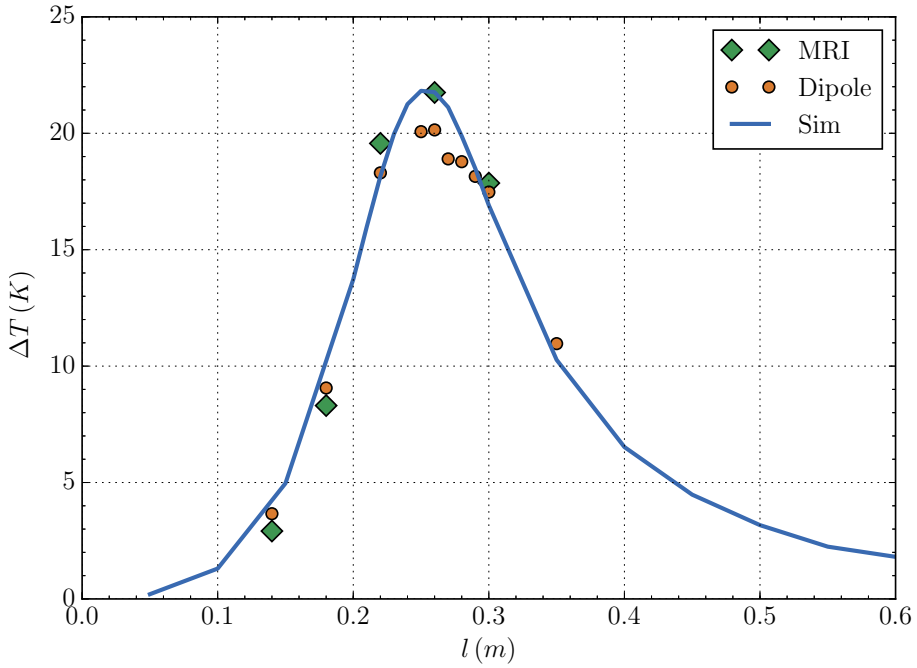

Figure 4.5: *The change in temperature ΔT near the distal electrode of an* 800 µm *copper wire coated with* 350 µm *of insulation, after 5 minutes of excitation. Experimental data is verified by several measurements about the resonant peaks in a 3T MRI machine. Simulated data is also overlaid.*

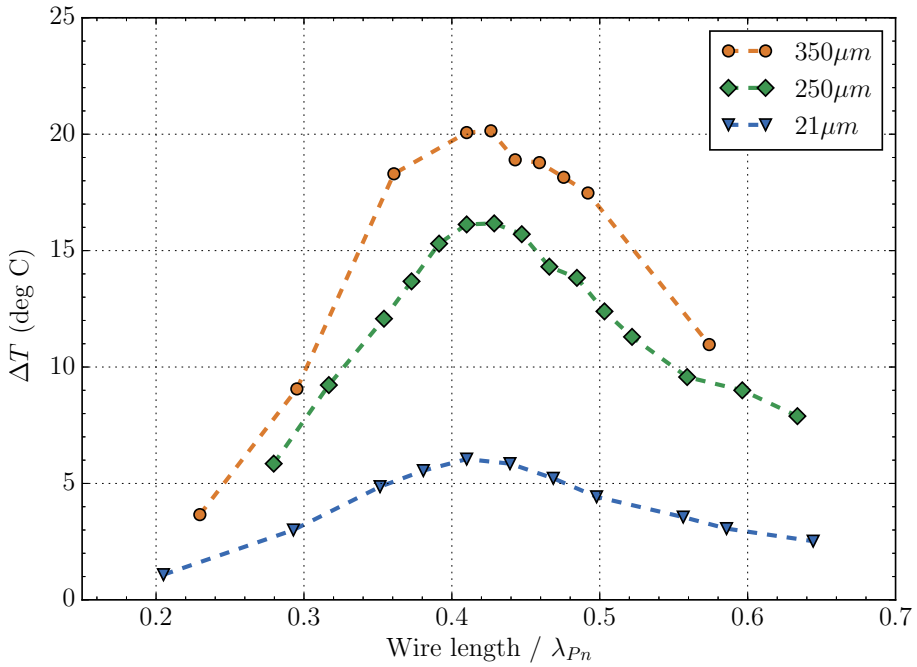

Figure 4.6: *The change in temperature ΔT near the distal electrode of the 350um insulated wire compared with two thinner insulation variants, after 5 minutes of excitation. The x-axis is normalised individually for each insulation type, such that the peaks occur at $0.41\lambda_{Pti}$. The respective wavelengths are $\lambda_{P350} = 0.61\,\mathrm{m}$, $\lambda_{P250} = 0.54\,\mathrm{m}$, and $\lambda_{P21} = 0.33\,\mathrm{m}$.*

that the peaks occur at $0.41\lambda_{Pti}$. As expected, the resonant length shortens for thinner insulation types and produces less peak heating, consistent with [60].

4.1.6 Conclusion

We explain a measurement technique to assess the RF heating of implant leads to MRI, without an MRI machine. We show that a dipole antenna excited with a 128 MHz CW with < 30 W of power, will generate significant heating of implant electrodes in agreement with MRI excitation.

4.1.7 Acknowledgement

We would like to thank the Waikato Medical Research Foundation (WMRF) for funding. We also acknowledge WaikatoLink and KiwiNet for their valuable support. Thanks are due to Midland MRI for support and access to their MRI machine.

4.2 Further Details of Method (Unpublished)

4.2.1 Measurement Set-up

Further details about the set-up used for measurements in the lab is provided below. A description of the measurement procedure is also included.

Phantom

A torso-and-head phantom after [19] comprised a clear acrylic casing and lid containing 28 L of gelled saline with $\sigma = 0.47\,\mathrm{S/m}$. The case dimensions are in figure 4.7. The concentrations of NaCl and polyacrylic acid (PAA) to distilled water were 1.32 g/L and 10 g/L, respectively. A large drill press fitted with a paint stirring blade was used to provide an initial stir, followed by a kitchen blender to remove any remaining lumps of discernable size. The recommended shelf life is 2 months.

An acrylic tray with adjustable holders was built to provide support and easy alignment of the test leads, temperature probes, and dipole antenna. Approximately one hundred 20 mm holes were drilled into the base of the tray to enable easy insertion into/removal from the phantom gel, as well as providing a stirring action upon movement. Figures 4.8 and 4.9 show the set-up.

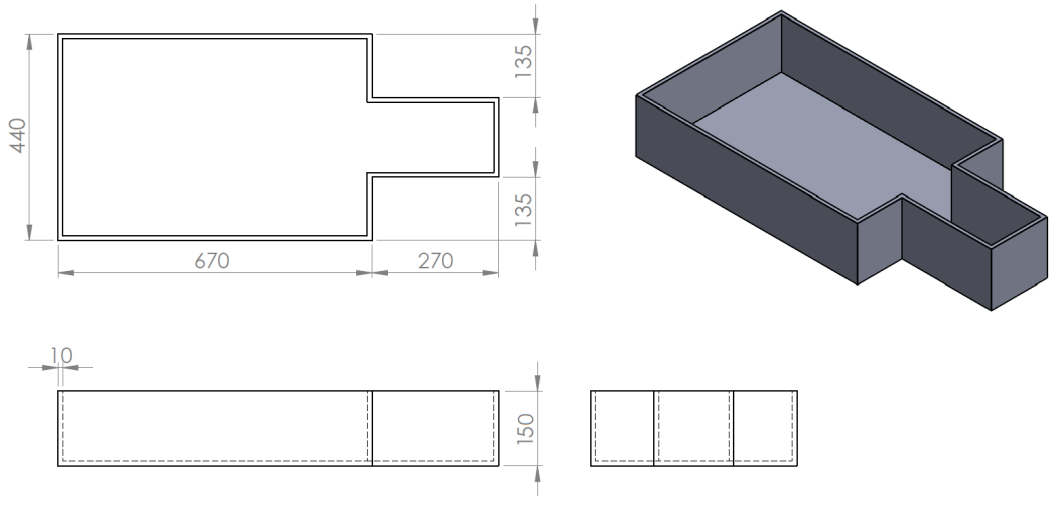

Figure 4.7: *Phantom casing design.*

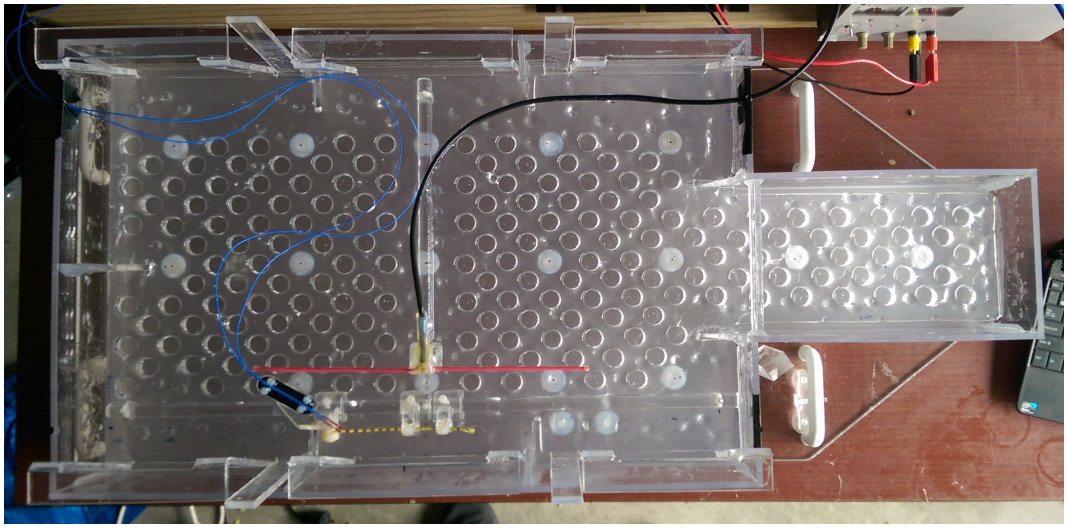

Figure 4.8: *Tray resting on top of the phantom gel. The test lead and temperature probes are aligned and secured with adjustable holders.*

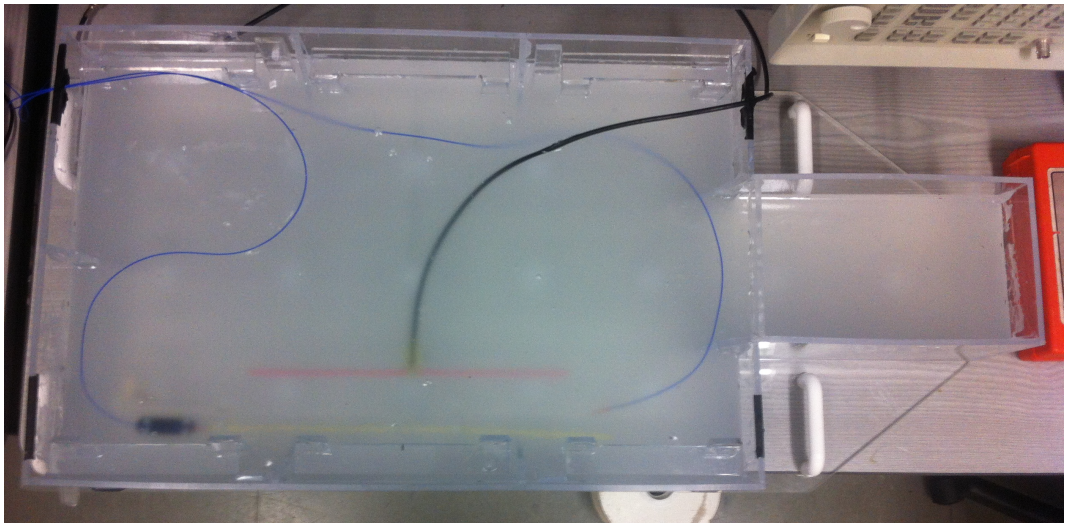

Figure 4.9: *Tray and apparatus immersed within the opaque phantom gel.*

Following immersion into the opaque gel, the alignment of the temperature probe can be checked for disturbance or air bubbles by carefully placing a short length of solid acrylic bar with polished ends into the gel near the distal electrode as is shown in figure 4.10. The first millimeter of the probe should be aligned and in contact with the electrode.

Figure 4.10: *Alignment of the temperature probe with the distal electrode can be viewed through a solid acrylic bar with polished ends.*

Thermometer System

The temperature of the test lead electrode and of the background were monitored using Optocon "TS2" GaAs-based temperature sensors on the ends of long optical fibers [62], [63]. The technique relies on the temperature dependent band gap of the GaAs semiconductor. The band gap alters the optical wavelength at which the sensor turns from transparent to reflective. For GaAs, this threshold is about 850 nm with a temperature dependence of 0.4 nm/K. Measurement is achieved using a miniature spectrometer. Such probes and optical fibers are immune to the effects of magnetic fields and RF radiation, and hence ideal for use within MRI machines.

RF Excitation

Positioning of the test lead close to one side of the phantom was selected according to [19], a region where the electric field is expected to be highest during an MRI scan. Considering the close proximity of the test lead relative to the three sides of the phantom, most of the energy induced in the test lead by the MRI birdcage is delivered by the portion of rungs that experience the least path attenuation within the phantom. In figure 4.11, this corresponds to the right-most rungs. Also, irrespective of where the test lead is positioned within

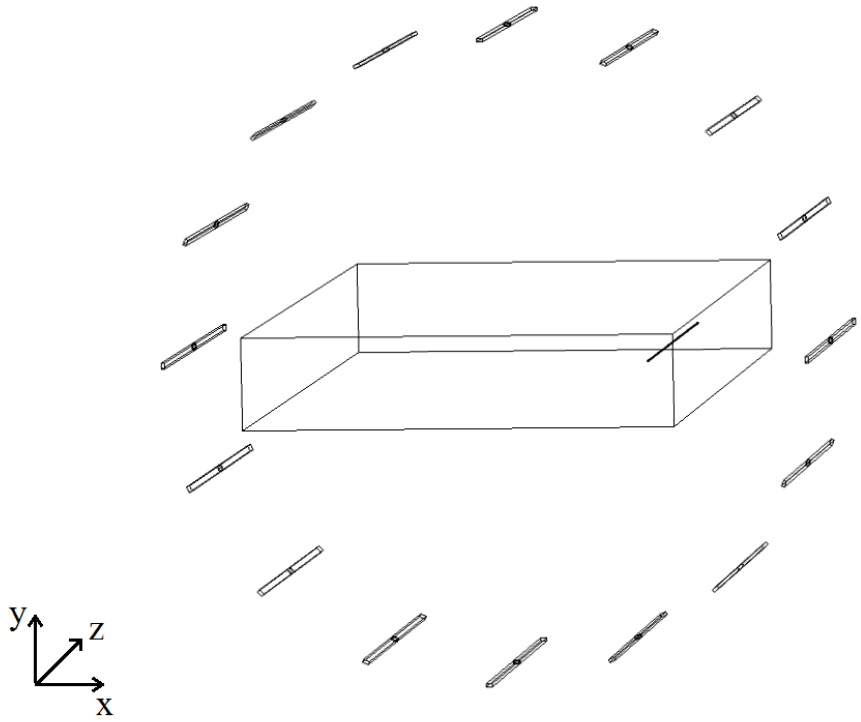

Figure 4.11: *Simplified view of the centre driven rungs of a birdcage antenna surrounding the phantom and test lead.*

the phantom, at 128 MHz the closest rung is no more than 0.3 wavelengths away[8], and is therefore coupled in the near-field.

A single insulated dipole antenna can be a simple substitute for the more complex MRI birdcage. Although only linearly polarised, it was shown in the APMC paper to be sufficient in replicating the excitation of RF currents in simple test leads from MRI. It was positioned adjacent to the test lead, separated by approximately 0.25 wavelengths. Immersing the insulated dipole antenna within the phantom permits the antenna to have smaller physical dimensions and also minimises the energy losses into the environment external from the phantom.

[8]The number of wavelengths is calculated by determining the electrical distance from a lead positioned in the center of the phantom to the nearest rung, with $\lambda_0 = 2.3\,\mathrm{m}$ and $\lambda_P = 0.24\,\mathrm{m}$.

Test Procedure Using the Dipole Radiator

1. Rest the tray on top of the gel phantom.

2. Position and secure the test lead using the adjustable holders such that it is suspended 6 cm from one side of the phantom but centered longitudinally and vertically within the torso.

3. Position the dipole antenna adjacent to and centered with the test lead. The spacing between the pair should be approximately 6 cm.

4. Align the temperature probe(s) to the distal electrode(s) as shown in figures 3.6 and 4.3.

5. Dislodge the tray and slowly immerse into the gelled saline with a slight incline (to prevent the formation of air bubbles from collecting under the tray). Lower the tray until it reaches the bottom of the phantom casing.

6. Ensure the temperature probe is correctly aligned with no air bubbles present (figure 4.10).

7. Enable the thermometer logging software and ensure the temperature remains in a steady state over a 2 minute period [19].

8. Supply a 40–45 dBm sinusoidal signal at 128 MHz to the dipole radiator using an RF generator and a 30 W amplifier [64].

9. Monitor the temperature readings for 5 minutes and then deactivate the RF stimulus.

10. Repeat the experiment with shorter/longer lead lengths to locate the resonant length and level of peak heating.

11. Compare to a reference measurement in an MRI machine and/or simulation, and scale the result accordingly.

Chapter 5

Complementary Measurement Technique

As was previously shown, an implant lead will experience peak distal heating during an MRI scan when its length can sufficiently support half-wave resonance. As the lead geometry and material properties have a significant influence, this resonant length is usually estimated through simulation and/or measurements of many leads varying by length. In the following manuscript, a simple technique for measuring this parameter with Time Domain Reflectometry (TDR) is described. The technique aims to reduce the number of heating measurements that are normally necessary to determine the maximum distal heating.

5.1 "Measurement of Implant Electrode Leads using Time-Domain Reflectometry to Predict the Resonant Length for MRI Heating"

Steven McCabe and Jonathan Scott
Department of Engineering, The University of Waikato, Hamilton, New Zealand

Published in the *Proceedings of the 22nd Electronics New Zealand Conference (ENZCON 2016)*, Wellington, 17-18 Nov. 2016, pp. 90–94.

The co-authorship form is provided in appendix A.

5.1.1 Abstract

Magnetic Resonance Imaging (MRI) machines can generate hazardous RF heating of patients with implanted neurostimulation leads. Consequently, most patients with these implants are contraindicated from having MRI scans. The level of RF heating has a strong dependence on lead length and is most severe when the length is close to a specific resonant length. Recent studies have shown that simple modifications to the lead construction and insulating material can alter the resonant length and significantly ameliorate this heating hazard, achieving MRI safety. We propose a technique using time domain reflectometry (TDR) to find the resonant length of an arbitrary lead such to minimise the amount of MRI machine time needed to find the length of highest heating. The results are compared with temperature measurements made in a 3-Tesla MRI machine and with a CW dipole radiator in the lab.

5.1.2 Introduction

Implant leads such as those found in pacemakers, Spinal Cord Stimulators (SCS), and Deep Brain Stimulators (DBS), can be hazardous to a patient

Figure 5.1: *Distal end of a* 62 cm *SCS "Octrode lead". Eight platinum electrodes, each* 3 mm *long and* 1.3 mm *in diameter, are separated by* 4 mm *insulating spacers. Electrode numbering starts from '1' (left-most electrode) to '8' (right-most electrode).*

undergoing a Magnetic Resonance Imaging (MRI) scan. Fig. 5.1 shows a typical implant lead for SCS. The RF field generated by a 3 T MRI machine can deliver peak pulses exceeding 30 kW in power at 128 MHz. [40] This can induce significant heating of patient tissue at the distal electrodes [6, 60], well beyond the 1–2 °C safety limits recommended by the International Commission on Non-Ionizing Radiation Protection (ICNIRP) in [8]. This has lead engineers to develop implant leads that are insusceptible to RF heating from MRI. [16, 42, 65, 66]

An implant lead is most hazardous at a specific resonant length, l_{res}, a parameter which can be exceedingly difficult to calculate and resource intensive to simulate. Typically it is found through measurement in an MRI machine or in the lab with dipole radiators, where heating tests are made on several implant leads varying by length [67]. We present an alternative approach that employs Time Domain Reflectometry (TDR) to allow simple and rapid extraction of l_{res} from a single measurement.

5.1.3 Distal Heating

An implanted lead can behave as a resonant dipole to the incoming RF field from an MRI machine. [24] Stored energy is transferred along the length of the dipole and can permeate out into the surrounding tissue, especially around the bare electrodes. This gives rise to joule heating and in some circumstances, can reach hazardous levels. Works by [41] and [60] have shown that peak heating occurs when the lead length is about $0.41\lambda_{Pn}$, where λ_{Pn} is the wavelength along the lead, largely determined by the tissue composition and lead design. Calculation of λ_{Pn} is possible but is limited to simple coaxial-like lead structures. [24] Simulation can provide predictions when the complexity is higher but demands considerable resources and impractical computation run times.

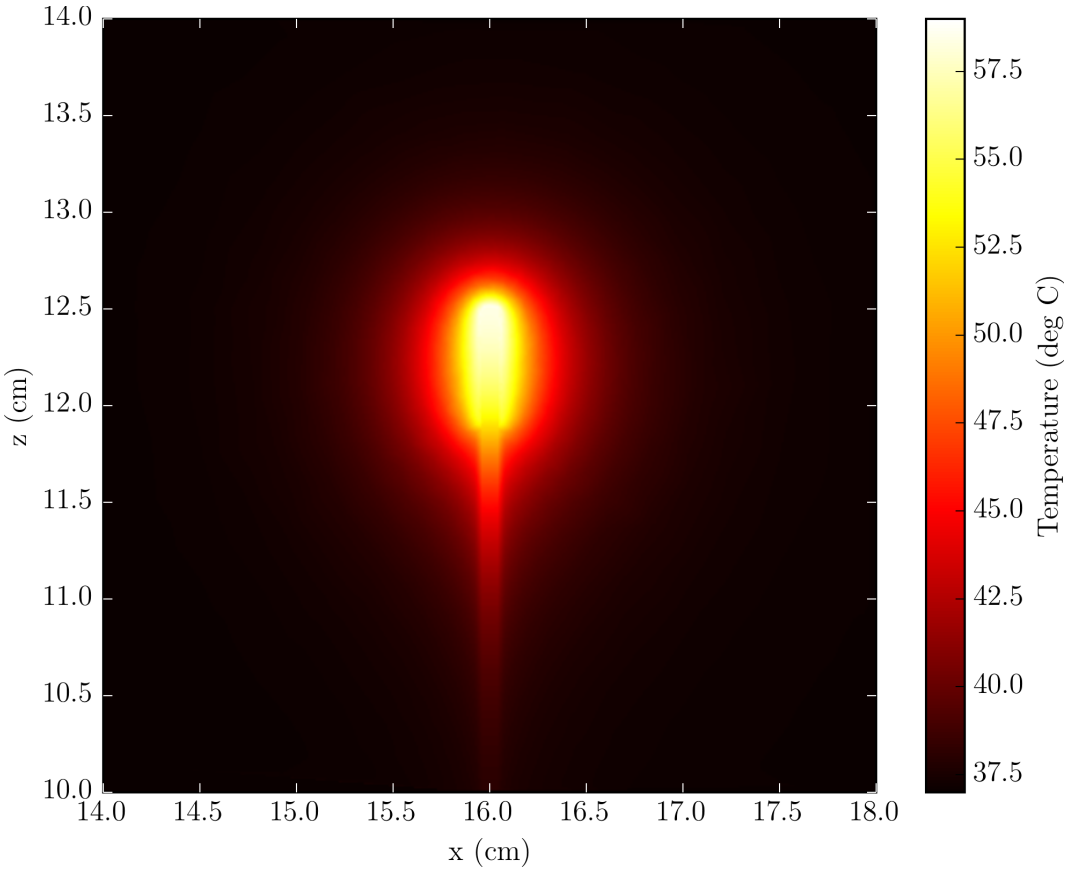

Figure 5.2: *Simulated heating generated at the* 6 mm *bared end of an insulated wire after 5 minutes of excitation from an MRI birdcage antenna. The* 800 µm *diameter wire was* $0.41\lambda_{Pn} = 25\,\text{cm}$ *in length, coated with plastic insulation* 350 µm *thick. Blood perfusion was included in the phantom model.*

Fig. 5.2 shows the simulated heating induced by an implanted wire within an MRI birdcage. The birdcage was calibrated to deliver a whole-body Specific Absorption Rate (SAR) of 1 W/kg. The three-dimensional simulation took 5 hours in COMSOL Multiphysics 4.4 running on a 3.5 GHz quad-core Intel CPU and consumed more than 60 GB of memory. Additional simulations were also needed in order to confirm the worst-case length for highest heating. For further simulation details refer to [41].

Experimental measurements are usually performed within a torso-shaped phantom inside of an MRI machine. Fig. 5.3 shows our phantom on the bed of a 3T MRI machine. The phantom is comprised of saline gel with electrical and thermal properties similar to that of human tissue. [19], [68] An implant lead under test is positioned within the gel and a fiber-optic based thermometer is aligned to the distal electrode where the heating is expected to occur.

Figure 5.3: *Operators preparing a wire sample for testing within a gelled saline phantom in a 3T MRI machine.*

As λ_{Pn} varies significantly with insulation thickness, permittivity, and geometry, its value is often unknown and is usually found by individually measuring the distal heating of several wires differing only in length ($\geq 10\,\text{cm}$), and looking for the length at which maximal heating occurs. A typical test set as shown in Fig. 5.4 contains 10 or more samples for a given lead type. The set-up and scan time to measure a single wire sample can easily exceed 30 minutes.

5.1.4 TDR Technique

In addition to antenna effects, an implanted lead behaves as an unbalanced transmission line to RF currents. [24] The conductive tissue along the surface of the lead jacket forms the return path for currents, like a shield to a coaxial cable, with the tissue surrounding the distal electrode forming the dissipative load.

TDR is a well established technique for measuring the propagation of signals along transmission lines [69]. Similarly, TDR can be applied to implanted electrode leads. The phase velocity v_p for an implant lead of arbitrary length

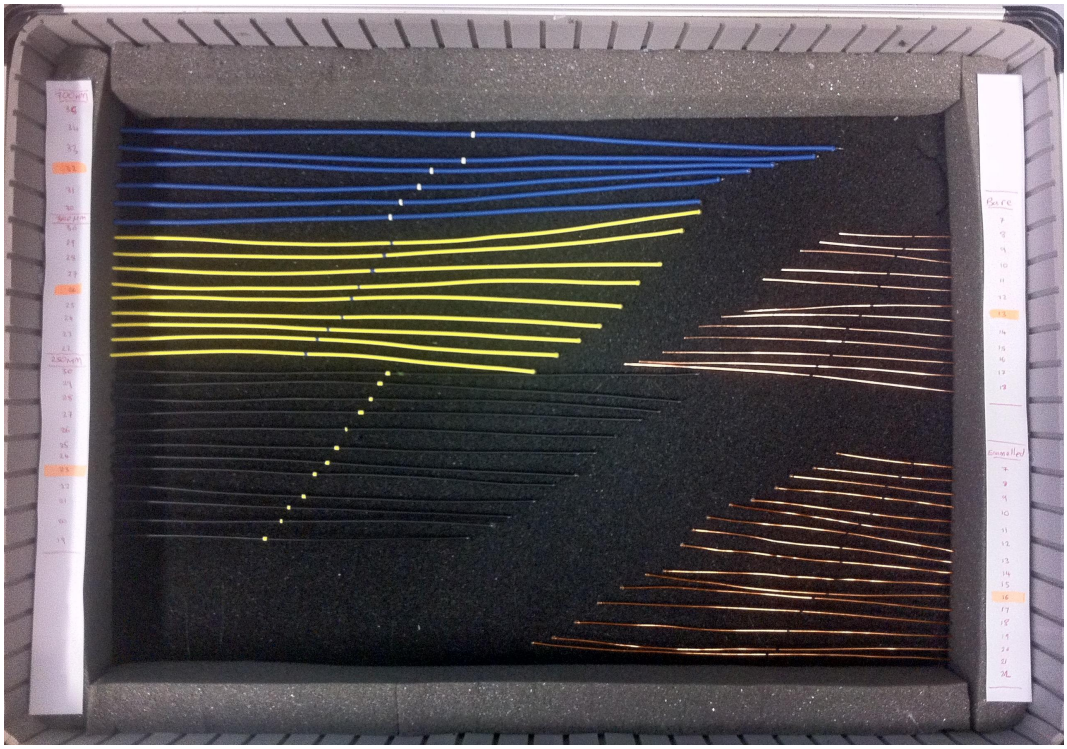

Figure 5.4: *Briefcase containing a range of wire samples to be tested.*

can be determined by measuring the time taken t_D for a voltage pulse to propagate to the end electrode and reflect back again:

$$v_p = \frac{2l_i}{t_D} \tag{5.1}$$

where l_i is the length of the insulated portion of the implant lead conductor. As the phase velocity is independent of length, the resonant length, l_{res}, of an implant lead at the MRI RF frequency f_{MRI} is therefore:

$$l_{res} = 0.41\lambda_{Pn} = 0.41\frac{v_p}{f_{MRI}} \tag{5.2}$$

The RF frequency of MRI is proportional to the strength of the static magnetic field. In a 3 T machine, the RF frequency is 128 MHz. When immersed in a gelled saline phantom from [19], a typical implant lead will have a λ_{Pn} in the order of tens of centimeters [67].

A phantom comprising 28 L of gelled saline in the shape of a torso-and-head was built from clear acrylic after [19]. The ratio of NaCl and polyacrylic acid (PAA) to distilled water was 1.32 g/L and 10 g/L, respectively, with an overall conductivity of 0.47 S/m.

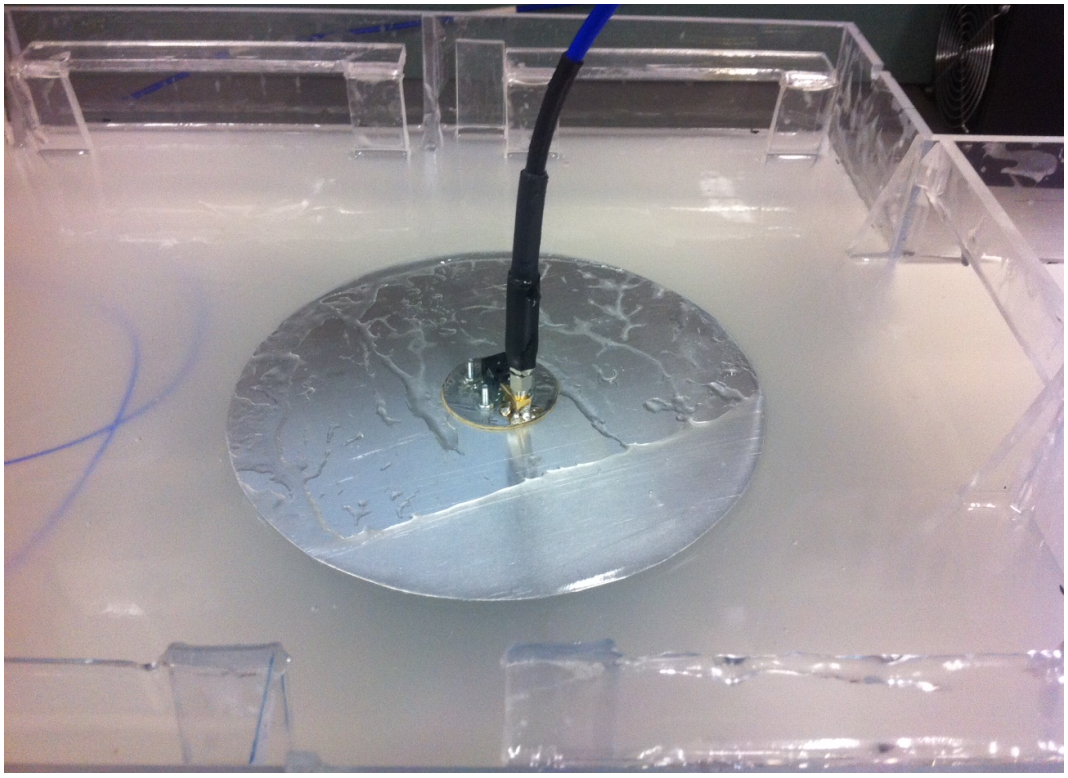

Figure 5.5: *An aluminium disc with a* 20 cm *diameter provides electrical connection from the coax cable shield to the gelled saline. Immersed within the gel, a wire sample is connected to the coax cable inner conductor via a small hole in the center of the disc and secured in place with a screw terminal.*

To facilitate TDR measurements of implant leads, the test fixture in Fig. 5.5 was constructed. A thin aluminium disc rests on the surface of the gelled phantom, providing an electrical path from the shield of the coax cable to the gel. A screw terminal secures the implant lead under test and provides electrical connection to the inner conductor of the coax cable. The implant lead is immersed within the gel, uncoiled, and with the distal electrode unobstructed. Close up views of the fixture are shown in Fig. 5.6.

Measurements of various wire samples representative of implant leads, were captured with an Agilent 54754A TDR with 40 ps system rise time. The reflection produced by a 29 cm wire sample with 6 mm distal electrode is shown in Fig. 5.7. The initial sharp change corresponds to the impedance mismatch between the 50 Ω SMA connector and the characteristic impedance of the wire sample. The reflection from the end of the wire sample can be identified by the second discontinuity, where the electrode comes into contact with the dissipative gel. Inserting a time delay of 7.18 ns into (5.2) yields a resonant length of 25.9 cm. Verification of this result is provided in section 5.1.6.

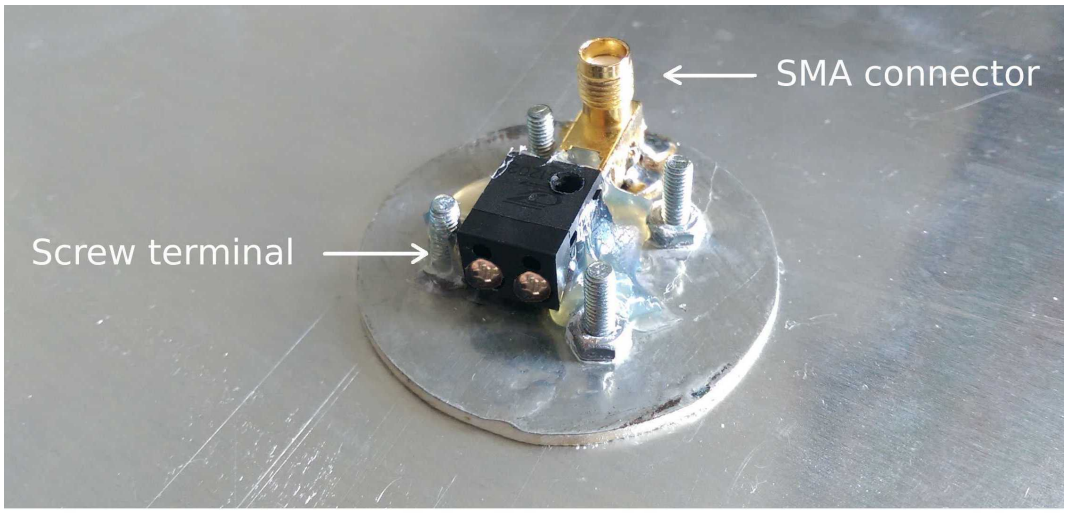

(a)

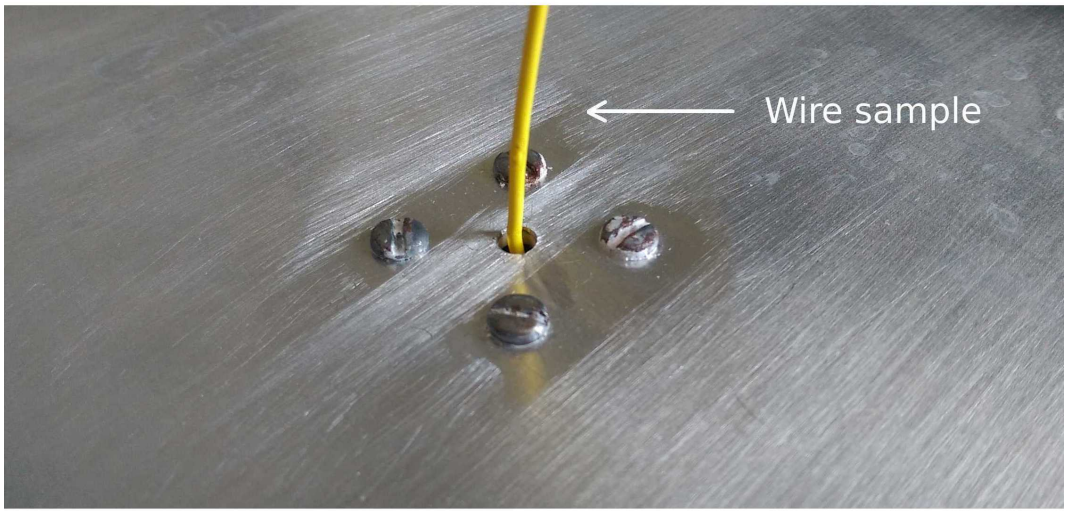

(b)

Figure 5.6: *Close up view of the disc (a) topside (b) underside.*

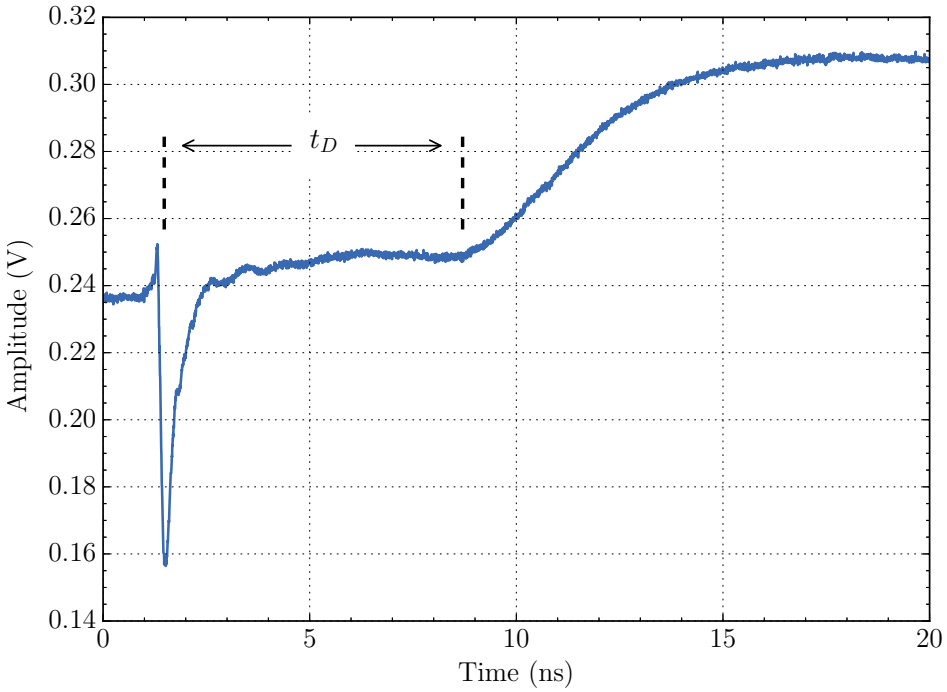

Figure 5.7: *Reflected TDR signal from a wire sample* 29 cm *in length, with insulation* 350 µm *thick. The time delay for a TDR pulse to propagate to and from the distal electrode is* 7.18 ns.

5.1.5 Verification Technique

Recent work in [67] demonstrated a lab technique for predicting the level of RF heating induced by an implant lead from MRI, without requiring high energy RF pulses from an MRI machine. A dipole antenna driven by a low-power CW is used to provide excitation of the implant under test, with a fiber optic probe to monitor the distal temperature.

The same experimental set-up from [67] was used and is shown in Fig. 5.8. A dipole antenna was made from rigid 2.1 mm diameter copper wire with 350 µm of insulation covering the entire 32 cm length. A close up view is shown in Fig. 5.9. A wire sample under test is spaced 6 cm from the dipole antenna and is centered about its midpoint. Temperature of the distal electrode is monitored with a GaAs-based fiber-optic temperature probe with 0.1 °C resolution.

Calibration of the experiment is achieved by scaling the result 1.5 times, such that the reference wire sample generates equivalent heating when exposed to the RF field from the 3 T MRI machine in Fig. 5.3. The reference measurement along with simulated predictions is shown in Fig. 5.10.

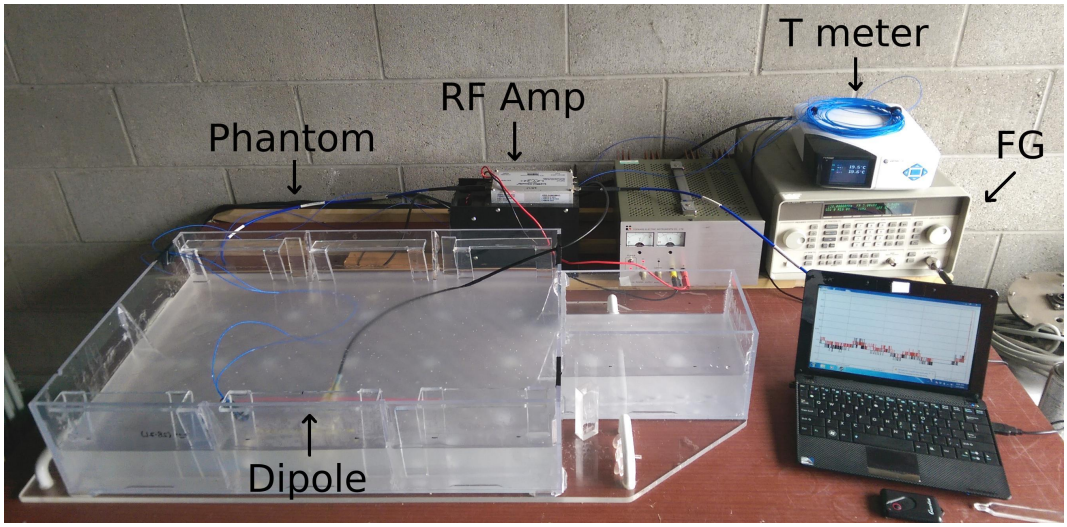

Figure 5.8: *Set-up for testing the RF heating of implant leads in the lab. A dipole antenna is immersed in the phantom alongside the wire sample with a function generator and* 30 W *RF power amplifier supplying excitation. A fiber optic thermometer monitors the temperature of the distal electrode.*

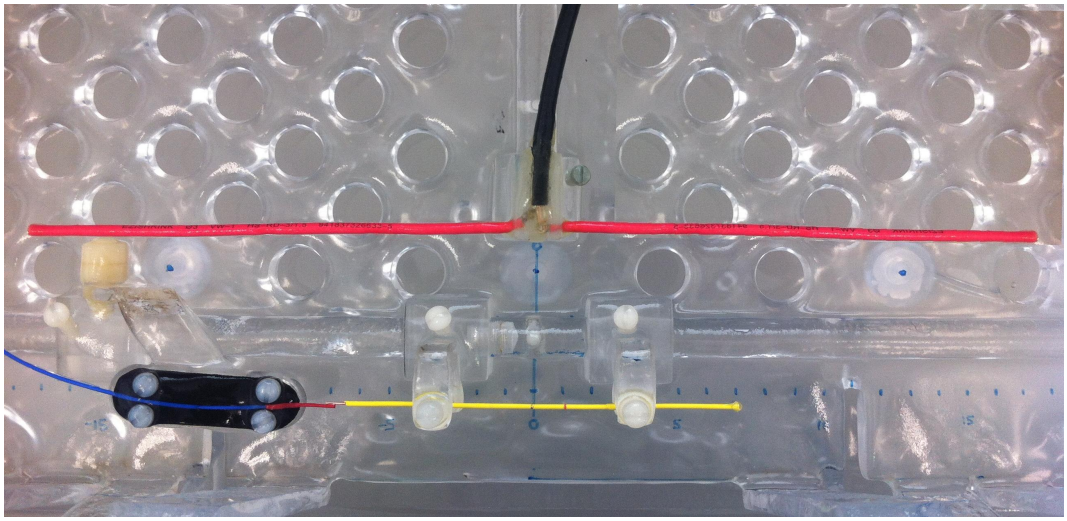

Figure 5.9: *Close-up view of the temperature probe aligned to the bared end of the wire sample (yellow) before immersion within the gelled saline. The dipole antenna (red) is spaced* 6 cm *away from the wire sample.*

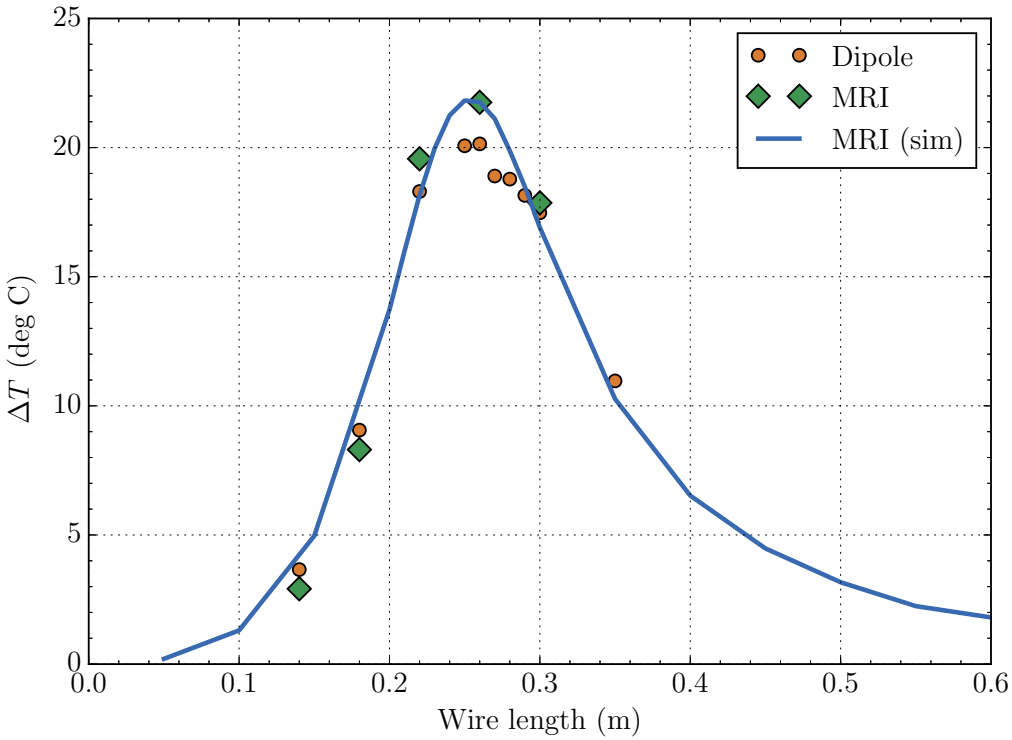

Figure 5.10: *Distal heating generated near the distal electrode of a reference wire sample coated with* 350 µm *of insulation, after 5 minutes of CW excitation from a dipole antenna. Measurements of the same wire sample in a 3T MRI machine are also shown along with simulated predictions.*

5.1.6 Measured Results

A range of wire samples varying in insulation thickness from 21–700 µm were tested. Each sample consisted of an 800 µm diameter copper core, with plastic insulation covering all but 6 mm from one end. Epoxy resin insulated the opposing end. The reflected TDR waveforms were captured for each wire sample using the test fixture in Fig. 5.5. The time delay t_D as measured from each waveform are listed in Table 5.1 along with the associated resonant length l_{res}, calculated using equations 5.1 and 5.2.

Heating tests using the dipole radiator for excitation were performed on each wire sample including several additional lengths. The change in temperature ΔT was recorded for each sample after 5-minutes of applied RF stimulus. The results shown in Fig. 5.11 are consistent with [41] and [60]. The lengths for peak heating as extracted from the same figure are summarised in Table 5.1. The TDR-measured values are within 3% of expected values.

Table 5.1: *Resonant lengths of various implant leads: expected and TDR-measured values.*

Lead Type	Conductor Length (cm)	t_D (ns)	l_{res} from TDR (cm)	l_{res} from ΔT_{pk} (cm)
21 µm	21.2	9.74	13.9	14
250 µm	29.8	8.55	22.3	23
350 µm	29.0	7.18	25.9	26
700 µm	34.3	7.42	29.6	30
Octrode (elec. 1)	61.8	6.68	59.3	-
Octrode (elec. 8)	54.8	7.12	49.3	-

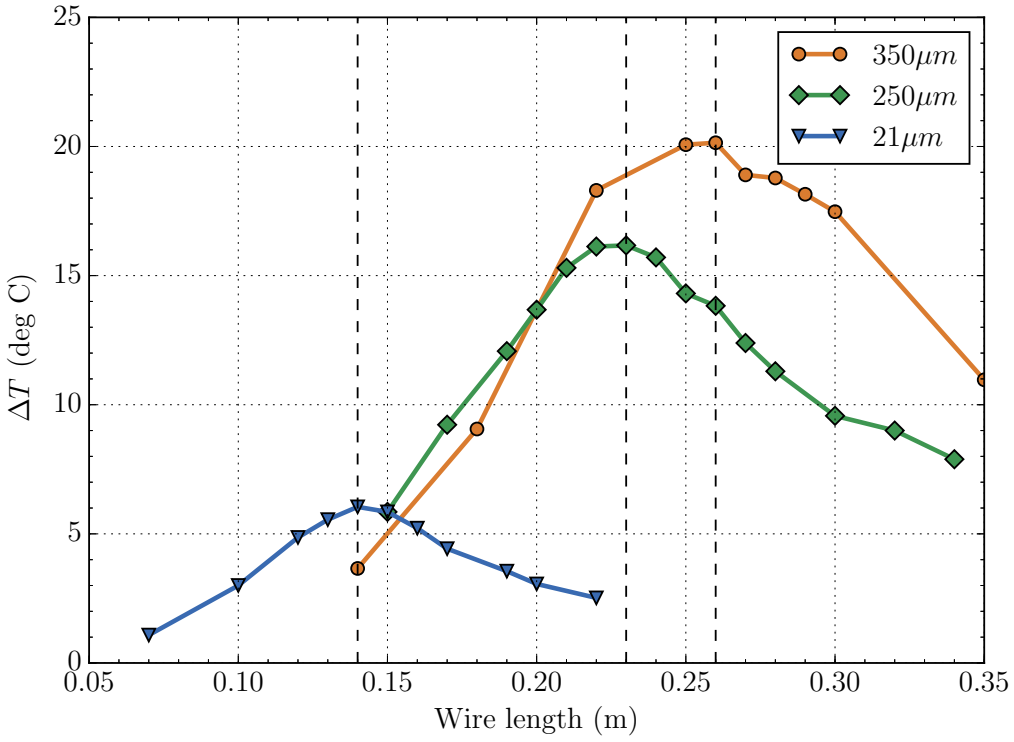

Figure 5.11: *Distal heating generated for wire samples varying by insulation thickness. Extraction of* $0.41\lambda_{Pn}$ *and* ΔT_{pk} *for a given lead type is achieved by measuring several lead lengths.*

TDR measurements were also performed on the electrodes of the SCS lead shown in Fig. 5.1. The predicted resonant length for electrodes 1 and 8 are twice that of the 700 µm and 350 µm wire samples, respectively. This is owing to the much smaller 100 µm diameter filars that comprise the lead. Heating tests on the SCS lead were not performed.

5.1.7 Conclusion

We explain a measurement technique that predicts the length an implanted lead will experience peak heating during MRI, without an MRI machine. We show this is possible through a TDR measurement of a single lead of arbitrary length.

5.1.8 Acknowledgement

The authors would like to thank Stephen Butler of Midland MRI for his kind assistance. They also acknowledge the Waikato Medical Research Foundation (WMRF) for funding, and WaikatoLink and KiwiNet for their valuable support.

5.2 Further Results and Discussion (Unpublished)

5.2.1 Second TDR Measurement

Greater measurement accuracy of the time delay in section 5.1.4 can be achieved by acquiring an additional TDR reflection: the signal reflected when the distal electrode is removed from the gel phantom. The time delay can then be computed by overlaying the two waveforms as is shown in figure 5.12. The time location of the electrode is evident from the point where the two waveforms start to diverge.

This method is particularly useful when the extraction of a well defined time delay is not possible from an evaluation of a single reflection. In the case of the SCS Octrode, the time delay for the "electrode 1" measurement was measured inaccurately and therefore misreported in table 5.1. Corrections of these values using the two-reflection method are presented in table 5.2.

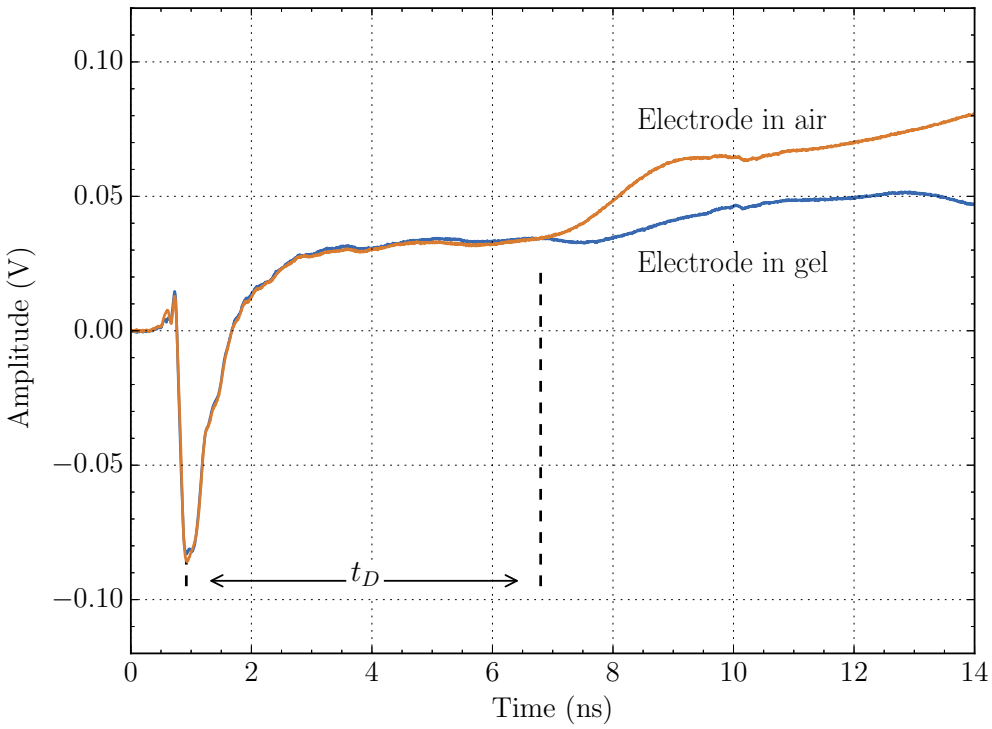

Figure 5.12: *Reflected TDR signals from the most distal electrode (electrode 1) of the SCS Octrode lead. The time delay for a TDR pulse to propagate* 61.8 cm *to the distal electrode is* 5.88 ns.

Table 5.2: *Corrections to previously misreported values.*

Lead Type	Conductor Length (cm)	t_D (ns)	l_{res} from TDR (cm)	l_{res} from ΔT_{pk} (cm)
Octrode (elec. 1)	61.8	5.88	67.3	-

5.2.2 Distal Heating of an SCS Octrode Lead

The distal heating of the SCS Octrode lead from figure 5.1 was measured in the lab with the results presented in figure 5.13. The experiment was calibrated to deliver a whole-body SAR = 1 W/kg. The plot is representative of the heating at a single length only, approximately 5.5 cm short of the resonant length according to the TDR measurement in table 5.2. Identical leads with different lengths were unavailable for testing. The effect of a surgical stylet is also shown and highlights a potential risk of additional heating if mistakenly left in place following surgical implantation. However, referring to section 3.2.3, existence

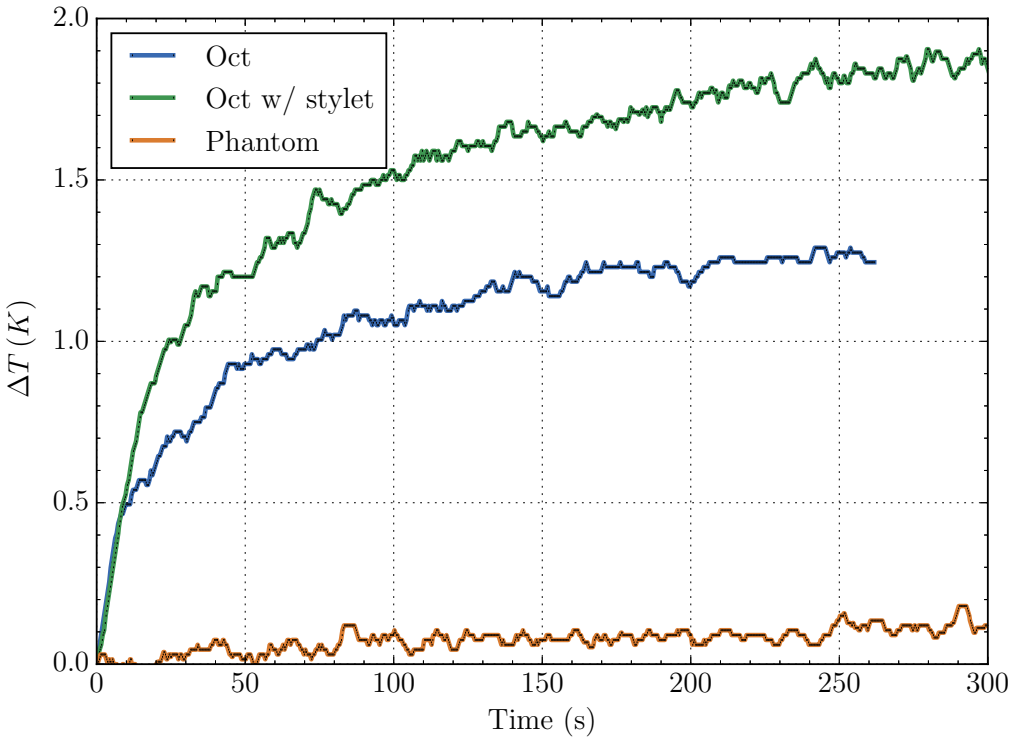

Figure 5.13: *The change in temperature ΔT measured at the most distal electrode (electrode 1) of the SCS Octrode lead with and without a surgical stylet in place. The ambient temperature of the phantom is shown for the latter. Temperature readings were acquired with a sample rate of* 4 Hz *and averaging set to 20 times.*

of a stylet should cause a decrease in the impedance between the filars and the surrounding tissue and therefore reduce peak heating at the resonant length. Further testing on different lead lengths is needed to confirm this expectation.

In comparison to the 350 µm test lead, the resonant length of the SCS lead is almost 2.5 times longer. Worst case distal heating can be expected to reach 6–12 °C, assuming a similar rate of increase to the measurements of test leads in figure 5.11. This suggests that the single electrode model that has been used so far may not be sufficient in accurately representing commercial leads with multiple electrodes. As such, further investigation is provided in chapter 7.

Chapter 6

Introduction to the Decoy Invention

This manuscript introduces an invention that effectively eliminates the distal heating hazard of implant leads in MRI machines. It is the culmination of countless brainstorming sessions, hundreds of hours and gigabytes worth of simulations, and a multitude of painstaking measurements in an MRI machine and the lab. National and international patents have been filed [66], [3]. The technology has been licensed to Sydney medical implant firm, Saluda Medical, to build into the design of their neurostimulation products for MRI compatibility.

6.1 "New MRI-safe Implant Electrode Design"

Steven O. McCabe and Jonathan B. Scott
Department of Engineering, The University of Waikato, Hamilton, New Zealand

Published in the *Proceedings of the International Microwave Symposium (IMS 2016)*, San Francisco, 22–27 May. 2016, pp. 1–3.

The co-authorship form is provided in appendix A.

6.1.1 Abstract

Medical implants often prevent patients having Magnetic Resonance Imaging (MRI) scans because the leads behave as antennas with respect to the RF excitation and cause hazardous heating in neural tissue. This manuscript describes an approach that virtually eliminates the risk of RF heating by means of easily-incorporated, mutually-coupled filars. The resulting leads need be neither physically larger nor significantly more costly than existing designs. Combined with thin insulation and surface roughening techniques, this manuscript represents the first complete release of recently-patented technologies. Both simulations and measurements at 128MHz are presented to confirm performance in 3-Tesla MRI machines.

6.1.2 Introduction

The RF hazard that accompanies MRI scanners for patients whose bodies contain conductive leads is well known. [6] The MRISAFETY.COM web site is used by radiographers the world over to check if an implant is safe or conditionally safe before a patient is scanned. [10] Despite numerous patent filings, only one product claiming to be MRI-safe has appeared, and that product addresses only 64 MHz, 1.5 T machines. [41, 42]

6.1.3 This Work

This manuscript introduces the "decoy" technique. When combined with existing thin-insulation techniques [41] and surface treatments [42, 60, 70], it is expected to achieve unconditional MRI-safe performance. Decoy requires as little as a single extra filar to be incorporated into an implant lead. It operates through mutual coupling to an added filar of selected length and with thin insulation. [41, 66, 70] The approach will be discussed in detail in section 6.1.5.

6.1.4 Ordinary Implant Lead

The distal electrodes at the end of a typical implant lead for SCS is shown in Fig. 6.1. Such leads can range up to several hundred millimeters in length, or 1–2 wavelengths in vivo. [71] When an implanted electrode appears to be just short of half a wavelength, concentrated current around the tip leads to tissue heating. [41] Fig. 6.2 shows agreement between heating predicted by simulation, measured with a torso phantom in a commercial 3 T MRI machine with a whole-body SAR of 1 W/kg as shown in Fig. 6.3, and measured with 128 MHz dipole radiators and a CW power amplifier. [67] The safety threshold of 1–2 °C as endorsed by the International Commission on Non-Ionizing Radiation Protection (ICNIRP) [8], is exceeded by more than ten times at the worst-case length.

Figure 6.1: *Distal end of an "Octrode" lead intended for SCS. Eight platinum electrodes, each* 3 mm *long and* 1.3 mm *in diameter, are separated by* 4 mm *insulating spacers.*

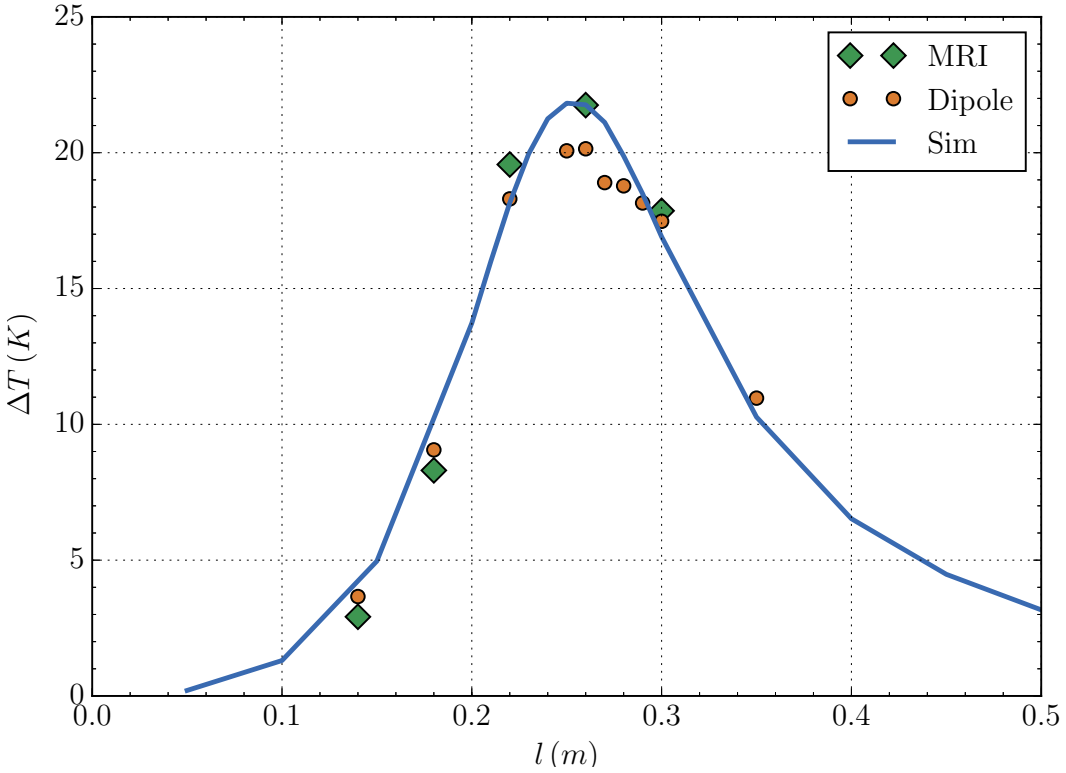

Figure 6.2: *Simulated and measured temperature rise ΔT near the distal electrode of an insulated wire after 5 minutes in a 3T MRI machine. Measurements from the dipole test method yield a similar profile.*

Figure 6.3: *Clear acrylic phantom on the bed of the MRI machine with operators.*

6.1.5 Lead with Mutually-Coupled Decoy

Near-field interaction is essential in the operation of antenna arrays. A Yagi-Uda antenna for example, employs directive and reflective elements mutually coupled to a driven dipole, forming a highly directional antenna. [22] Implant leads may be regarded as "Antennas in matter", a subject that has been dealt with in detail by King. [24] In the case of an implant electrode, an additional and preferably bare conductor, hereinafter referred to as *decoy*, can be attached to the exterior of the lead. The direct contact between the decoy and tissue provides a damping effect in accordance with results reported in the literature. [41, 60] This damping is "felt" by the lead conductors through mutual coupling. Currents induced in the lead conductors by MRI excitation are reduced, leading to abated joule heating at the electrode-to-tissue interfaces.

To confirm this expectation, simulations were performed in COMSOL Multiphysics 4.4 with a phantom model set according to ASTM F2182-11a [19]. We used the same simulation arrangements that have been previously reported in [41]. Referring to Fig. 6.4, simulation predicts that the current induced in a single conductor insulated from the surrounding saline medium after the fashion of an implant lead filar (a) will be significantly reduced when that filar is accompanied by a second, uninsulated filar (b), and even more so in the case of two mutually-coupled filars (c).

Fig. 6.5(a) shows simulated predictions of the distal heating for an assortment of leads with length l, each having a single decoy of specified proportionate length. A decoy of length $0.6l$–$0.7l$ seems to produce the least amount of heating over the range. Heating is virtually eliminated for leads with two decoys as is shown Fig. 6.5(b), when the length of each equivalent decoy is between $0.7l$–$0.9l$.

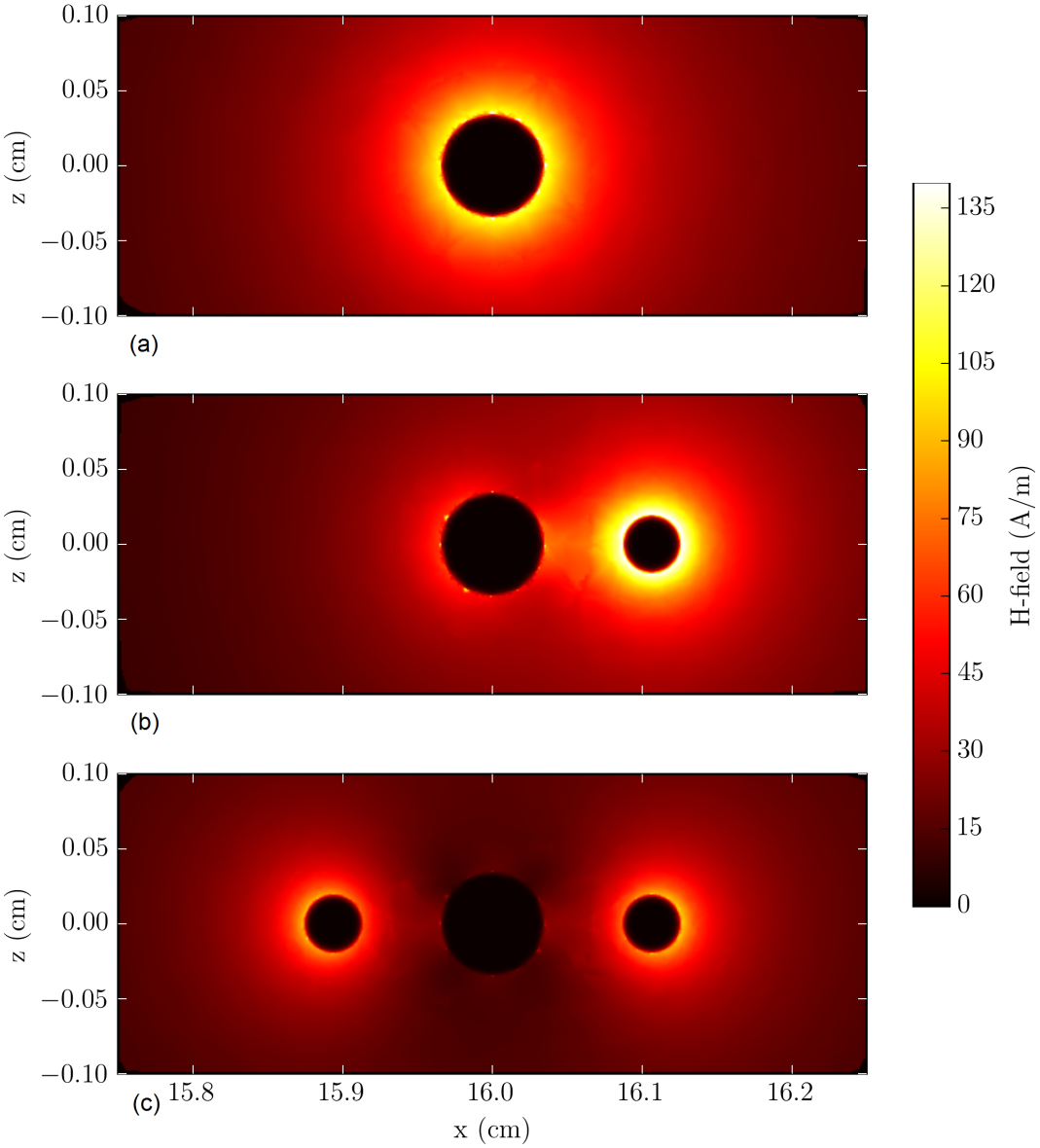

Figure 6.4: *Midpoint cross-section showing the simulated magnitude of the H-field surrounding an (a) ordinary electrode lead (b) electrode lead with single bare* $0.6\,l$ *decoy (rightmost conductor) (c) electrode lead with two bare* $0.9\,l$ *decoys (outermost conductors). The length of the electrode lead is* $25\,\mathrm{cm}$.

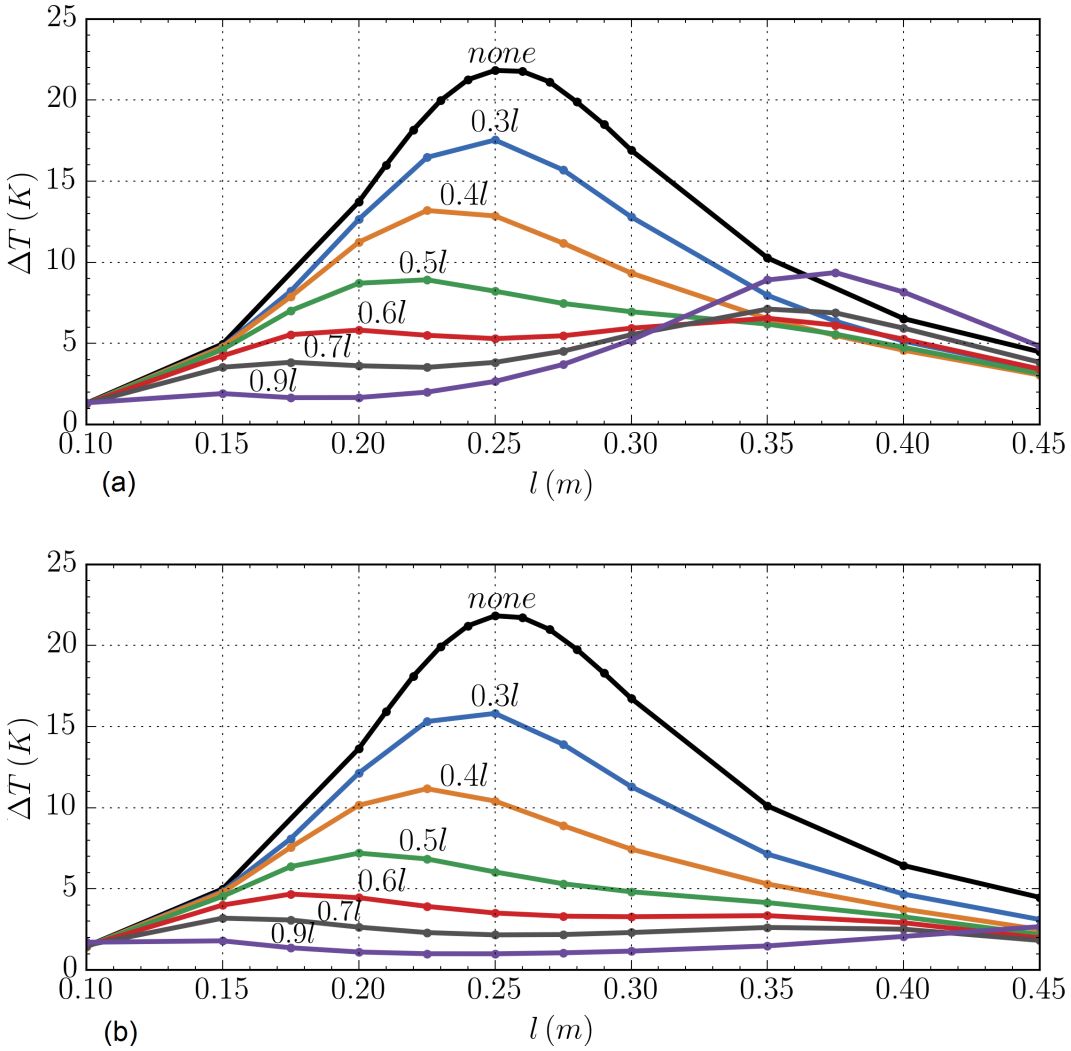

Figure 6.5: *Simulated heating profile ($t = 5\,\mathrm{min}$, $SAR = 1\,\mathrm{W/kg}$) at the distal electrode as a function of lead length, for a range of electrode leads each with (a) a single decoy (b) two decoys. Electrode leads differ by a fixed decoy-to-lead length ratio in the range of 0.3 – $0.9\,l$. An ordinary electrode lead without a decoy has the profile denoted by "none".*

6.1.6 Measured Results

Fig. 6.6 depicts test leads with diameters and insulation thickness identical to ones that have been previously reported in the literature [67, 70], but to which we fitted adjacent, bare, "decoy" filars. These are used to verify simulations against measurements in MRI and in the lab.

The measured heating of leads with a single $0.6\,l$ decoy and a $0.9\,l$ decoy are shown in Figs. 6.7(a) and 6.7(b), respectively. Previously simulated results are overlaid in the same figures. For the lead with the $0.6\,l$ decoy, we measure a temperature rise of less than 6 °C over the entire lead length range. The $0.9\,l$ decoy produces an even smaller temperature rise of just 2 °C when the lead length is short.

Fig. 6.8 shows a further reduction in heating when the same leads have an additional and identical decoy. A rise of just 0.5 °C is measured when the lead is 30 cm long with $0.9\,l$ decoys, corresponding to a 97% reduction when compared to the ordinary implant lead in Fig. 6.2.

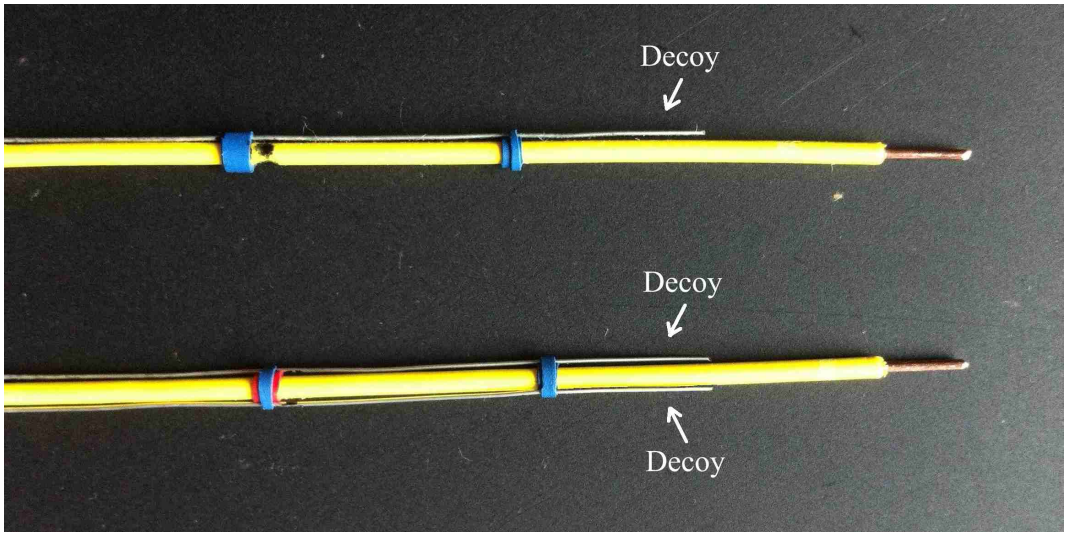

Figure 6.6: *The single decoy (top) and dual decoy (bottom) test leads comprise of* 800 µm *dia. copper wire coated with* 350 µm *worth of insulation covering all but* 6 mm *from one end (the electrode).* 400 µm *dia. bare copper wire adhered alongside the lead forms the decoy(s).*

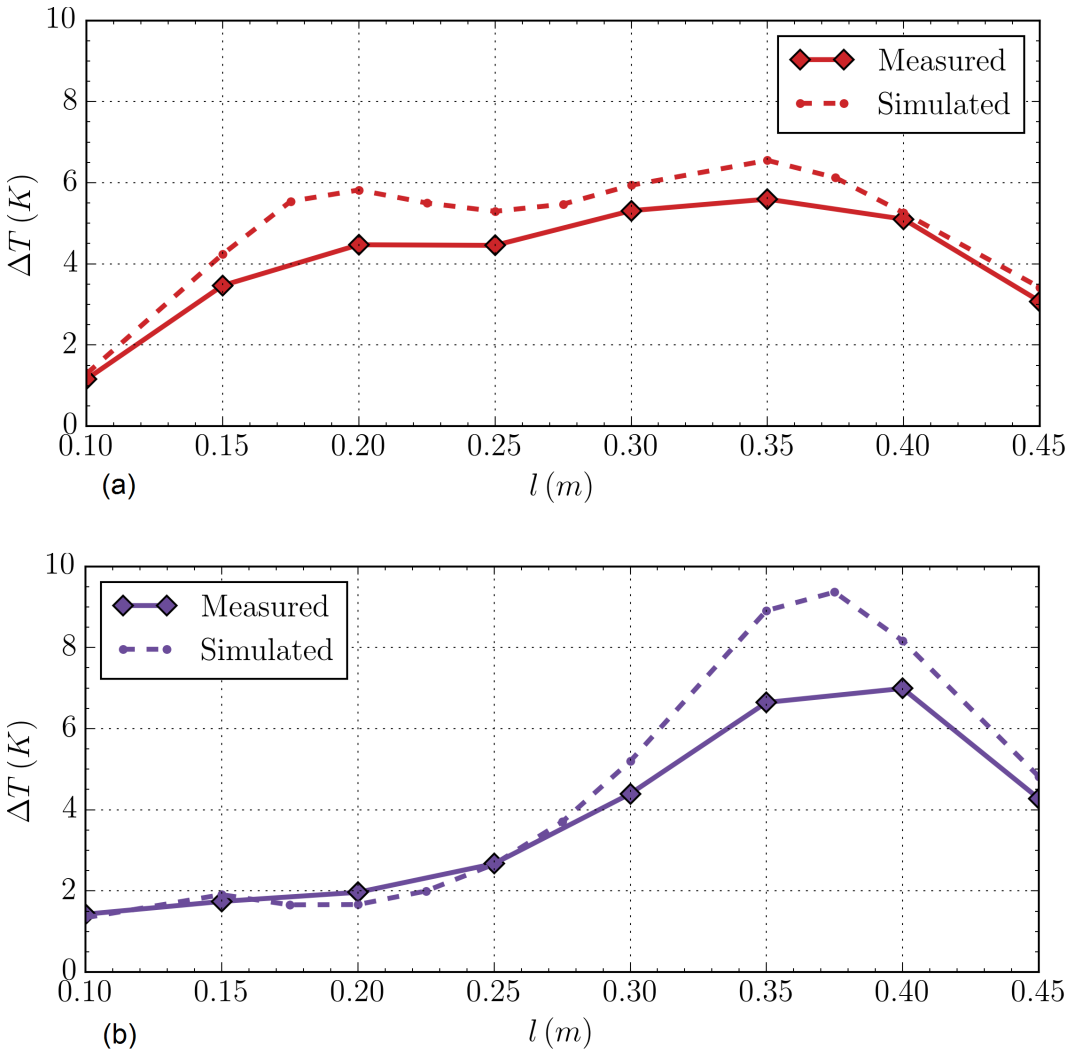

Figure 6.7: *Measured heating profile ($t = 5\,\mathrm{min}$, $SAR = 1\,\mathrm{W/kg}$) of electrode leads attached alongside single decoys with decoy-to-lead length ratios of (a)* $0.6\,l$ *and (b)* $0.9\,l$.

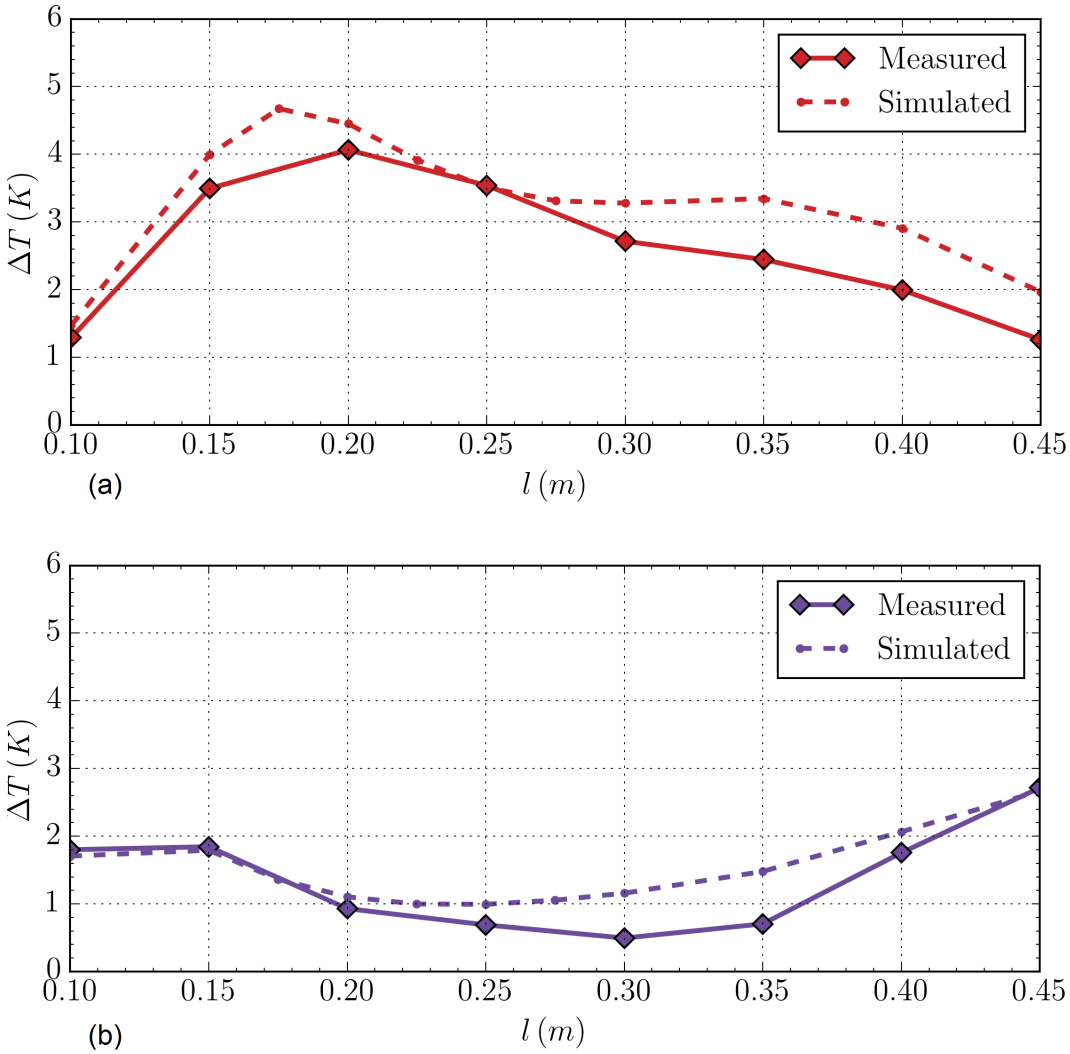

Figure 6.8: *Measured heating profile ($t = 5\,\mathrm{min}$, $SAR = 1\,\mathrm{W/kg}$) of electrode leads attached between two decoys with decoy-to-lead length ratios of (a) $0.6\,l$ and (b) $0.9\,l$.*

6.1.7 Discussion

A cost-effective implant electrode design that meets the ICNIRP standard for safe heating has been achieved through the addition of uninsulated filars of preselected length, to the exterior of the lead. Further improvement to the safety margin may be possible by increasing the ac resistance of the lead conductors to a few hundred ohms per meter. Roughening the surface of lead filars as described in [42] is expected to provide that increased RF impedance without negatively impacting on implant battery life implied by dc resistance. [41], [60]

6.1.8 Conclusion

We introduced a novel technique that will prevent hazardous heating normally mediated by implanted conductors in 3-Tesla MRI machines. The technique relies upon the use of mutual coupling applied simultaneously with techniques that the authors have previously reported elsewhere. Simulation and measurement in a phantom confirm the impact of the technique. Two patents have been filed so far.

6.1.9 Acknowledgement

The authors wish to thank Stephen Butler of Midland MRI for his kind assistance.

6.2 Further Results and Discussion (Unpublished)

6.2.1 More on Decoys

Inclusion of one or more decoy filars into an implant lead design is a simple and cost-effective method for achieving MRI safety. Patent details are provided in section 8.1. Implementation requires little change in the design and complexity of regular leads, and can be achieved with already well-established manufacturing processes. Furthermore, the impact on the normal stimulation operation of the implant is negligible, owing to the electrical isolation between the decoy(s) and the main filars at the kilohertz stimulation frequencies.

Figure 6.9 is an MRI image that was captured during a 3 T scan of the phantom with implanted lead and decoy. Dark circular regions show the magnetic resonance energy is weakest in and around the conductors. The decoy appears to cast a shadow over the insulated wire, effectively reducing the RF energy in this space.

Decoy-protected leads may also deliver RF safety in MRI machines with smaller magnets, such as 1.5 T. At a frequency of 64 MHz, the RF field has a longer wavelength, about 43 cm in tissue. Correspondingly, implant leads will have longer resonant lengths and their electromagnetic response to decoy conductors will differ. Previously presented plots for distal heating will therefore need to be revised at this RF frequency. This is left for future work.

Figure 6.9: *An MRI image showing the midpoint cross section of the phantom and decoy protected lead. Captured with a GE Healthcare Discovery MR750 3.0T machine [72].*

6.2.2 Decoy Heating

Decoy conductors are not immune to RF heating. Similar to the distal lead electrode, current can freely enter tissue surrounding the decoy and give rise to joule heating. In figure 6.10, two dimensional views depict the simulated temperature of single and dual decoy-protected leads when subjected to MRI. Decoy heating is distributed over a larger volume and so generally exhibits less heating than the small distal electrode. This is apparent when comparing figure 6.5 to the plots of decoy heating in figures 6.11 and 6.12. However, for leads shorter than about 20 cm, the $0.9l$ decoys can generate slightly higher levels of heating, exceeding the temperature of the distal electrode by about

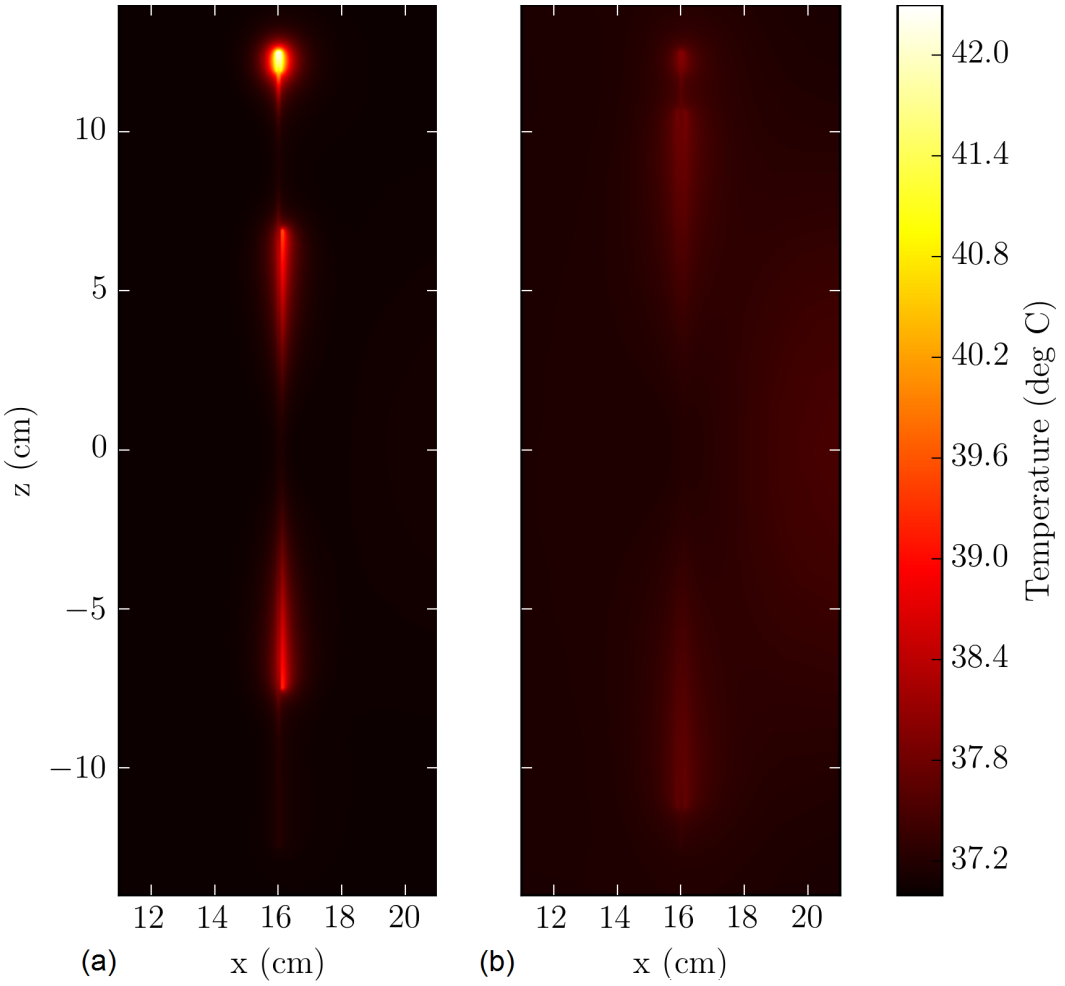

Figure 6.10: *Cross section displaying the simulated temperature of an (a) insulated wire with single bare* $0.6\,l$ *decoy (b) insulated wire with pair of bare* $0.9\,l$ *decoys (outermost conductors), following a 5 minute MRI scan with a whole-body SAR =* 1 W/kg *and an initial temperature of* 37 °C*. The combined length,* l*, of the insulated wire and* 6 mm *bared end is* 25 cm*.*

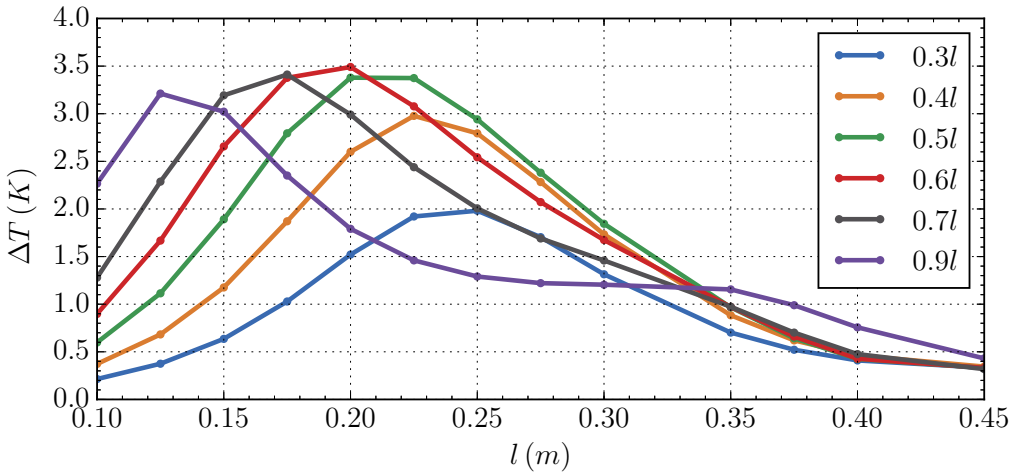

Figure 6.11: *Simulated peak decoy heating ($t_f = 5\,\text{min}$, $\text{SAR}_{wb} = 1\,\text{W/kg}$) as a function of wire length, for a range of leads each with a single decoy.*

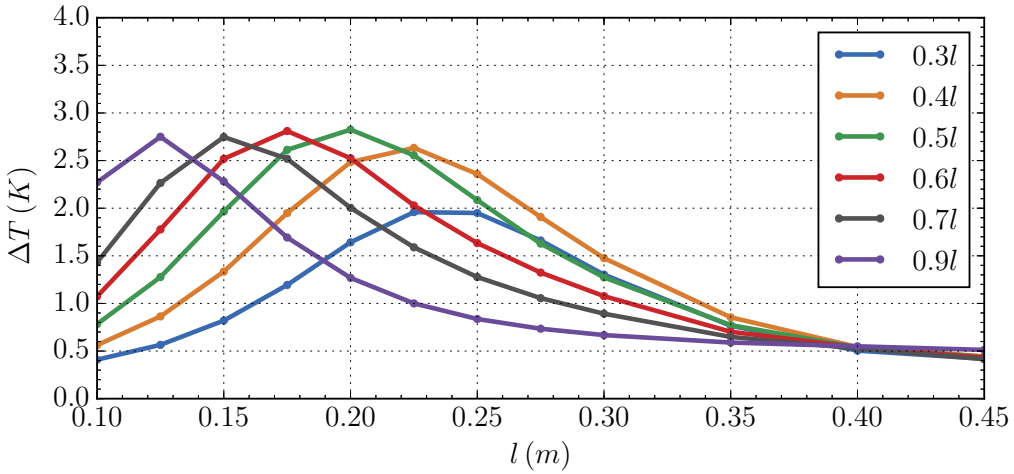

Figure 6.12: *Simulated peak decoy heating ($t_f = 5\,\text{min}$, $\text{SAR}_{wb} = 1\,\text{W/kg}$) as a function of wire length, for a range of leads each with two decoys.*

0.5–1 °C (but still safer than the plain lead equivalent). This is an important finding that needs to be taken into consideration when assessing the safety of decoy leads from heating measurements.

Interestingly, a visible difference in the average phantom temperature can be observed by comparing figures 6.10a and 6.10b. Less of the RF energy from MRI excitation is lost to the implant when two decoys are present, with the temperature of the surrounding phantom resembling the regular background heating that occurs in the absence of an implant.

6.2.3 Decoy Surface Area

A decoy with a larger diameter presents a greater surface area in contact with the surrounding medium ($A = \pi dl$). As such, leads with larger decoys exhibit improved heating characteristics. Figure 6.13 shows the reduction in distal heating achieved when doubling the diameter of the decoy conductor from 400 µm to 800 µm. A plot of decoy heating for the same leads is in figure 6.14. Longer leads in particular, benefit from the additional surface area.

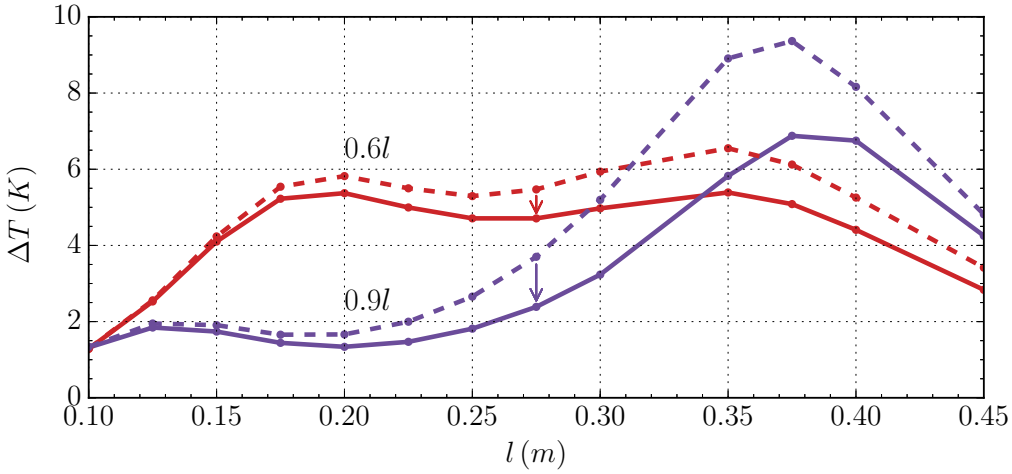

Figure 6.13: *Simulated distal heating for a lead with a* 0.6l *single decoy, and a lead with a* 0.9l *decoy. Dashed lines represent the lead with the* 400 µm *decoy. The solid line represents the* 800 µm *equivalent.*

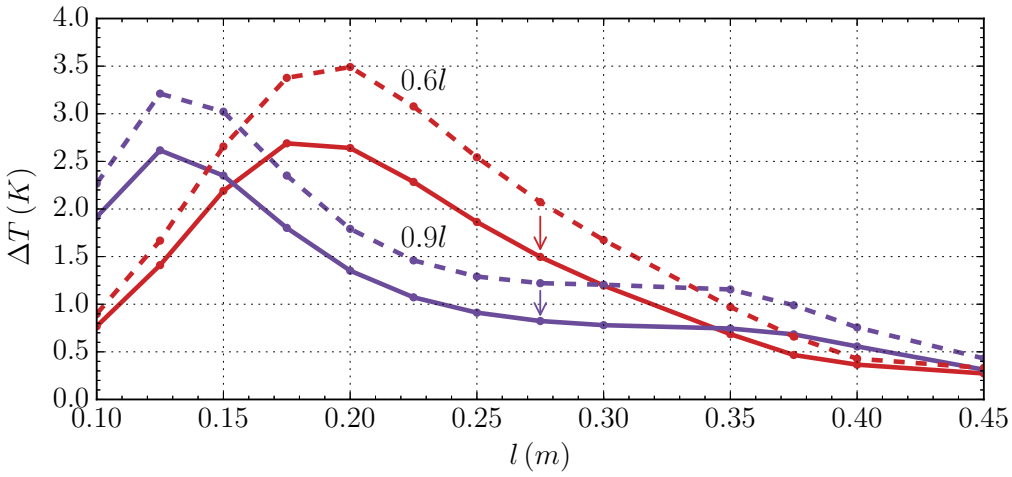

Figure 6.14: *Simulated heating of the decoy conductor. Dashed lines represent the lead with the* 400 µm *decoy. The solid line represents the* 800 µm *equivalent.*

It should also be possible to increase the surface area of a decoy without increasing its diameter. Decoys formed from ribbon, braided, or coil-like conductors could be effective. Connection of the decoy(s) to the conductive impulse generator housing or simply to existing or additional lead electrodes will also help (see section 8.2). Similarly, the surface roughening techniques from section 3.2.4 can easily increase the surface area of a material by double or more. This makes roughened decoys particularly appealing for future research.

Chapter 7

Multi-Electrode Leads with Decoys

The following manuscript concludes the series. In this work, testing is performed on leads that more closely represent commercial implant leads, having multiple filars and electrodes. The impact of decoy filars on these leads is explored.

7.1 "A Novel Implant Electrode Design Safe in the RF Field of MRI Scanners"

Steven McCabe and Jonathan Scott
Department of Engineering, The University of Waikato, Hamilton, New Zealand

Published in the *IEEE Transactions on Microwave Theory and Techniques (MTT) Journal*, vol.65, no.9, pp. 3541–3547, Sept. 2017.

The co-authorship form is provided in appendix A.

7.1.1 Abstract

Patients with medical implants are often unable to receive Magnetic Resonance Imaging (MRI) diagnostic treatment because the conductive leads can concentrate the RF excitation field and generate dangerous heating of nervous tissue. We propose a simple low-cost solution that minimizes RF heating through the addition of one or more mutually-coupled filars to the lead without significant increase in lead diameter. Simulations and measurements at 128 MHz are presented to verify the effect in 3-Tesla MRI machines.

7.1.2 Introduction

The RF field generated by the transmit coils in a Magnetic Resonance Imaging (MRI) machine can lead to hazardous heating of the patient [10]. Machines with 3 Tesla magnets are capable of delivering 128 MHz RF pulses of several tens of kW [40]. Normally the risk of heating is mitigated through active monitoring and control of the Specific Absorption Rate (SAR), defined as the rate of RF power absorption per object mass over a set exposure time [73]. The object mass is specified as either the whole-body, whole-head, or in situations where localized hot spots can occur, 10 g.

This safety measure is greatly inadequate for patients with medical implants,

Figure 7.1: *The distal end of an SCS lead with eight platinum electrodes. Each electrode is* 3 mm *in length,* 1.3 mm *in diameter, and spaced apart by* 4 mm *of insulation. Insulated platinum filars extend through the length of the lead to each individual electrode.*

particularly those comprising long electrode leads as found in Deep Brain Stimulation (DBS) and Spinal Cord Stimulation (SCS) implants. Fig. 7.1 shows the distal end of a typical lead for SCS. Such leads can range up to several hundred millimeters in length, or 0.5–2 wavelengths in vivo [74]. Under the RF field from MRI, the lead conductors can resonate as antennas and transfer RF energy into highly concentrated regions of tissue near the distal electrodes [6],[41]. The absorbed energy can generate significant heating and cause damage to the nervous tissue. Simulations reported in [60] reveal distal heating from MRI can concentrate into tissue mass of less than 1 g.

Radiographers from around the world routinely consult the online database in [10] to check if an implant has been tested and rated "safe" or "conditionally safe" before scanning the patient. Despite a spate of patent filings over the last decade, see [11] through [15] and [7, 17, 75], only one product is available that has been approved for use in MRI machines. The SCS system, developed by Medtronic is rated conditionally safe. It is limited to 1.5 T machines and requires a restrictive scanning protocol. Currently, there are no DBS products available that offer any MRI compatibility.

This manuscript introduces a new technique to improve the RF safety of implants in MRI machines and is an expansion of [65]. The technique, termed "decoy", requires as little as a single extra filar to be incorporated externally along the implant lead. It works by means of mutual coupling to an added filar of selected length and with thin insulation [41, 60, 65, 66]. When combined with resistive materials [41, 60] and surface treatments [42], it is expected to achieve superior MRI-safe performance with minimal scanning restrictions. The approach is explored in detail in section 7.1.4. In section 7.1.5 we expand

upon the single electrode work from [65] to include measurements on leads with multiple electrodes. We explore the impact of increasing the number of electrodes and demonstrate the effectiveness of adding decoy conductors to the lead.

7.1.3 Insulated Wire

Complex multi-electrode structures are generally modelled as simple single-core wire structures [6, 41, 60, 76, 77, 78] to avoid excessively long simulation times and impractical memory and CPU resource requirements. Most experiments are also limited to these simpler structures to help minimize the running time and costs associated with MRI machines. Fig. 7.2 compares the distal heating predicted by simulation with that measured in the commercial 3 T MRI machine in Fig. 7.3, for a whole-body SAR of 1 W/kg. For simulation details refer to section 7.1.4. The International Commission on Non-Ionizing Radiation Protection (ICNIRP) [8] recommends a threshold of 1–2 °C for tis-

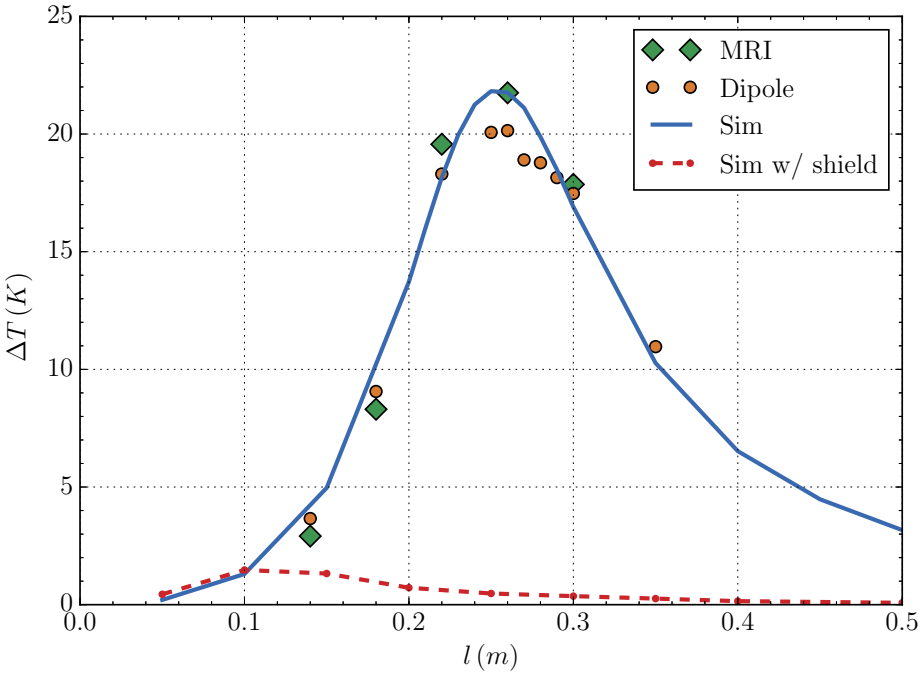

Figure 7.2: *Simulation and measurement of the temperature rise ΔT near the distal electrode of an insulated* 800 µm *dia. copper wire after 5 minutes of scanning in a 3T MRI machine [67]. Plastic insulation* 350 µm *in thickness covers all but the* 6 mm *electrode at one end. Simulation of the same lead but with a* 100 µm *thick platinum shield, is shown by the dashed line.*

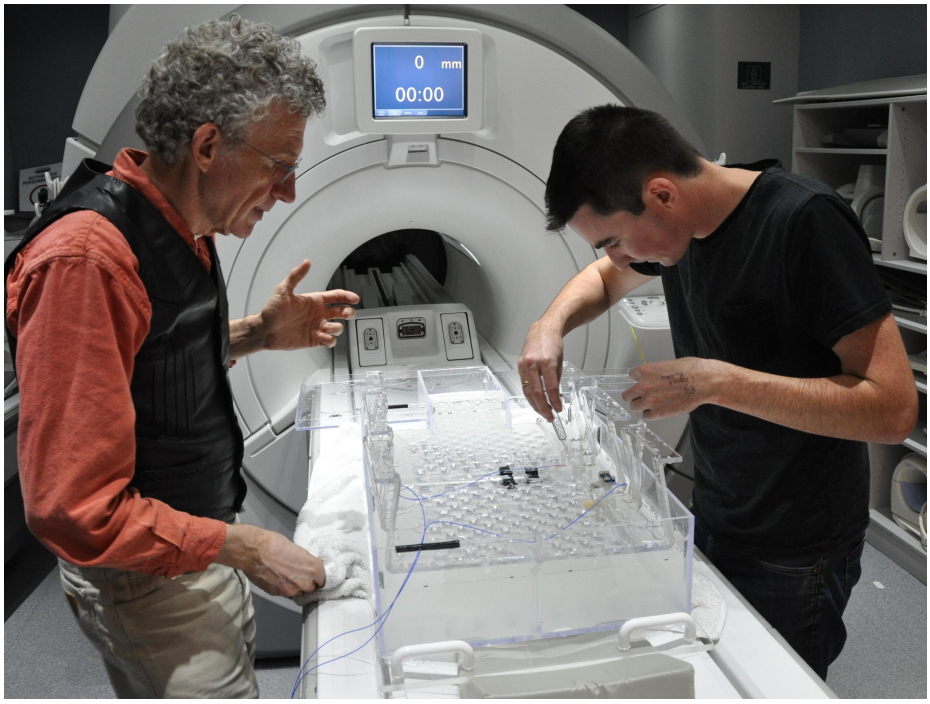

Figure 7.3: *Operators position an implant lead inside of a gelled saline phantom on the bed of a* 3 T *MRI machine. A GaAs-based fiber-optic temperature probe provides measurement of the distal electrode heating.*

sue heating, but this level is exceeded more than ten times in the worst case. Enclosing the lead within a cylindrical metallic shield results in a significant reduction of heating as is shown in the same figure, and is the key mechanism that achieves MRI-compatibility in the commercial leads by Medtronic.

Recent work in [67] and [74] has demonstrated the use of dipole radiators in place of an MRI machine to predict the level of heating induced by implant leads. Included in Fig. 7.2 are measurements made using 128 MHz dipole radiators and a 30 W CW power amplifier. The results are consistent with expectations and provide a handy tool for rapid evaluation of design changes.

7.1.4 Insulated Wire with Mutually-Coupled Decoy

The level of distal heating from an implant is proportional to the magnitude of current induced in the lead filars. Works by [36, 41, 60] have shown that an increase in filar resistance to several hundred per meter can significantly reduce RF currents and heating. Furthermore, the incorporation of series inductance [30, 36, 77], metal sheaths [17, 75], and shunt capacitance [41, 60] can also help impede or divert current flow. Seemingly lacking from the literature, are the effects mutual coupling between adjacent lead filars can have on the induction of RF currents from MRI.

Mutual coupling is an inherent mechanism of antennas, with influence only in the near-field. Yagi-Uda antennas utilize the effect to couple directors and reflectors with a driven dipole to achieve high directionality [22]. Similarly, implant leads can exhibit antenna-like behavior. An electrode is effectively an antenna embedded in matter, a subject that has been dealt with in detail by King [24].

When an additional and preferably bare conductive wire is attached to the exterior of the insulated wire from section 7.1.3, the pair will become mutually coupled at the MRI RF frequency. This ancillary filar is hereinafter referred to as a *decoy*. The intimate contact between the decoy filar and surrounding tissue provides a damping effect, an idea that has been reported in the literature [41, 60], and is mirrored by the insulated wire through mutual coupling [66]. Induced RF currents in the insulated wire are therefore smaller, resulting in abated power dissipation and joule heating at the electrode-to-tissue interface.

Simulation

Simulations were performed in COMSOL Multiphysics 4.4 using a phantom model set according to ASTM F2182-11a [19]. Excitation was provided by a 16 rung 128 MHz birdcage as in [41]. The implant lead was orientated 5.5 cm from the phantom's left side and centered longitudinally and vertically within the torso. With the exception of the lead dimensions, the simulation parameters correspond to those previously reported in [41]. Simulation predicts that the

current induced in a single conductor mostly insulated from the surrounding medium will be significantly reduced if the first filar is coupled to a second, uninsulated filar. The current is also reduced if the second filar is only thinly insulated, and reduced still further if two mutually-coupled uninsulated filars are deployed. See Fig. 7.4.

Fig. 7.5a plots predictions of distal heating along leads of various lengths in the presence of a single uninsulated decoy of specified proportionate length. It is apparent that an uninsulated filar with length 0.6–0.7 times the length of the insulated filar leads to minimal heating over the range. The resonant length is not only dependent on the thickness and permittivity of the insulating material [41, 60], but also varies with decoy length as is shown in the same figure.

Heating problems are almost entirely resolved when leads have two uninsulated decoys of length between 0.7–0.9 times the length of the main filar. See Fig. 7.5b. Although the decoys themselves experience some heating along their length, simulation predicts it will be less than the heating of the distal stimulus electrode, except for short leads with $0.9l$ decoys. This aberration is a result of the combined heating that occurs when the proximity between the decoy and electrode is close and will be highlighted in Figs. 7.9b and 7.10b.

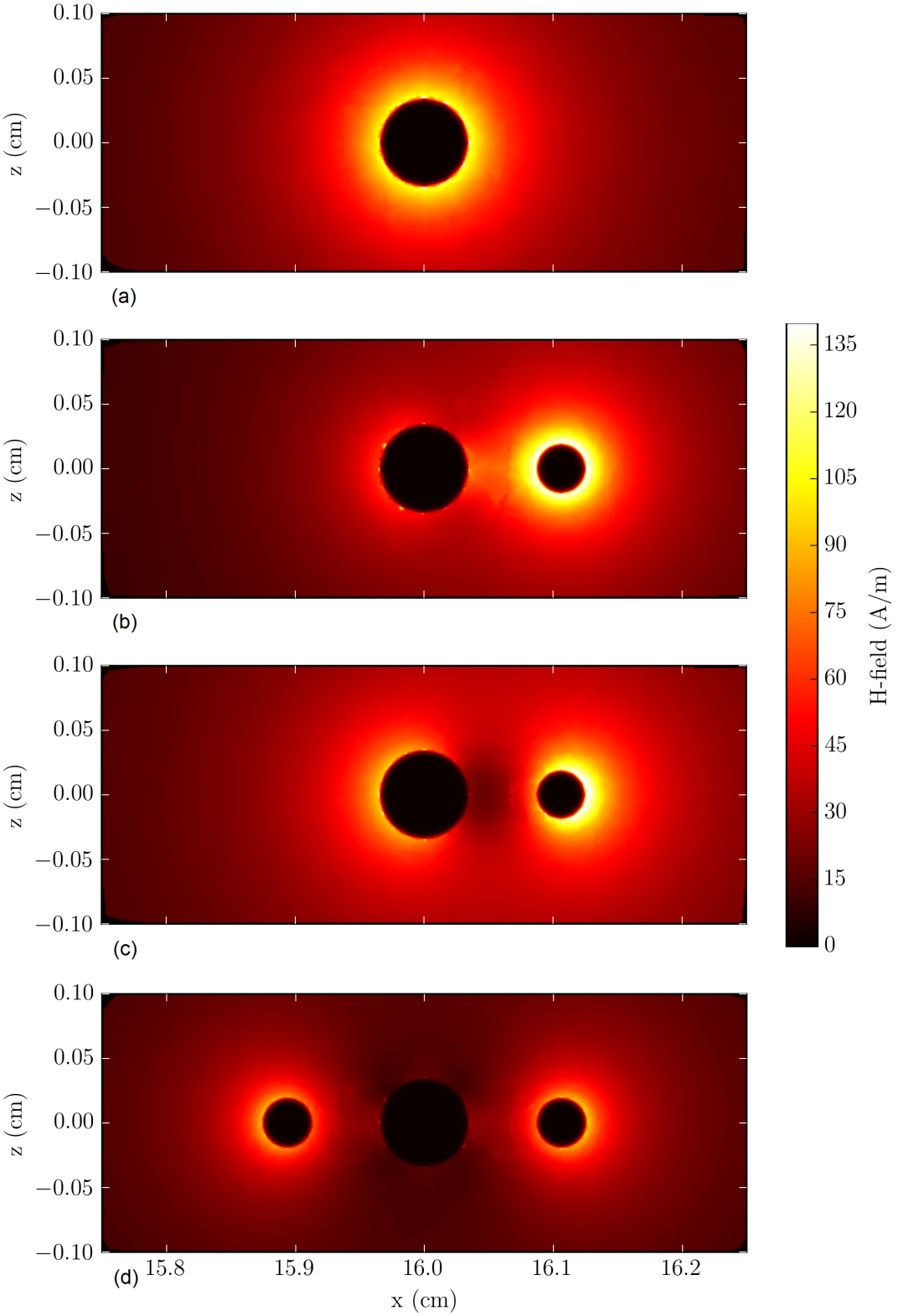

Figure 7.4: *Mid-point cross section displaying the simulated magnitude of the H-field surrounding an (a) insulated wire (b) insulated wire with single bare* $0.6\,l$ *decoy (rightmost conductor) (c) insulated wire with single* $0.6\,l$ *decoy coated with* $21\,\mu\text{m}$ *thick insulation (rightmost conductor) (d) insulated wire with pair of bare* $0.9\,l$ *decoys (outermost conductors). The combined length,* l*, of the insulated wire and* $6\,\text{mm}$ *bared end is* $25\,\text{cm}$*.*

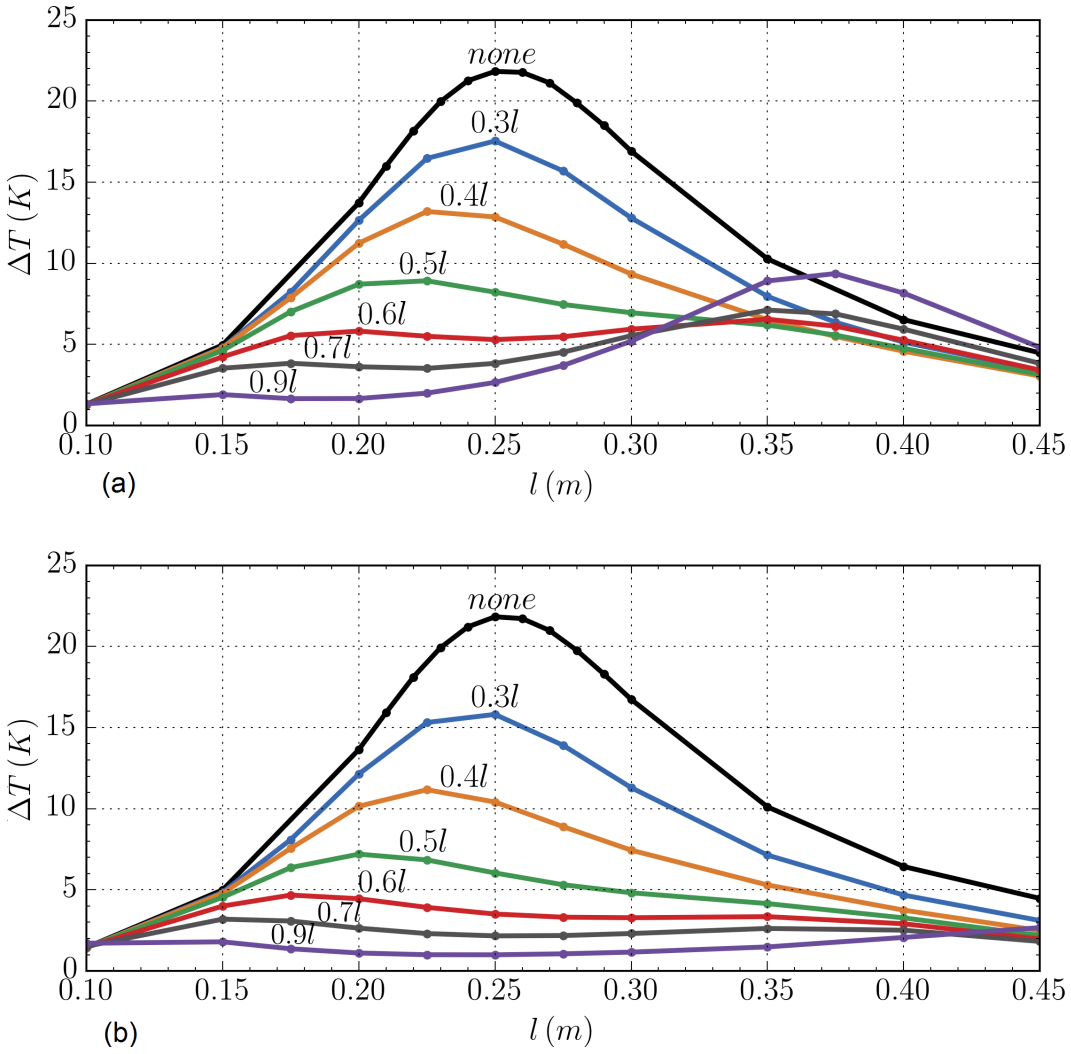

Figure 7.5: *Simulated distal heating ($t_f = 5\,\text{min}$, $\text{SAR}_{wb} = 1\,\text{W/kg}$) as a function of wire length, for a range of leads each with (a) a single decoy (b) two decoys. Leads differ by a fixed decoy-to-lead length ratio in the range of* $0.3 - 0.9\,l$*. The heating of an ordinary insulated wire without decoys is labeled with "none".*

Measurement

The experimental set-up from [67] and [74] was replicated and is shown in Fig. 7.6. Dipole radiators are positioned alongside the lead under test and driven by a 128 MHz CW through a 30 W RF power amplifier. An Optocon FOTEMP thermometer monitors the temperature of the distal electrode using a GaAs-based fiber-optic probe with 0.1℃ resolution. The experiment is calibrated for a whole-body SAR of 1 W/kg.

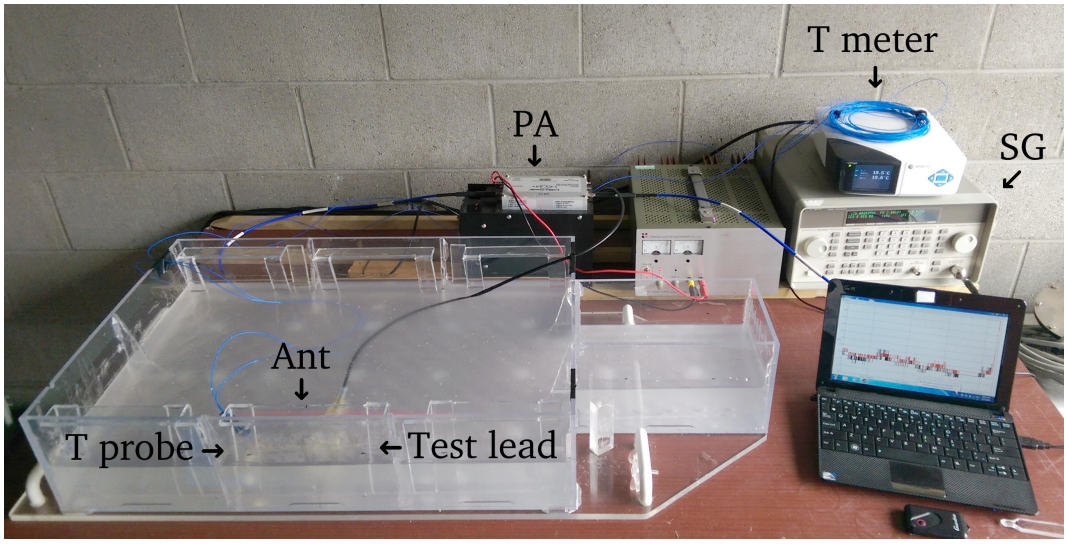

Figure 7.6: *Calibrated experimental set-up to measure RF heating in the lab.*

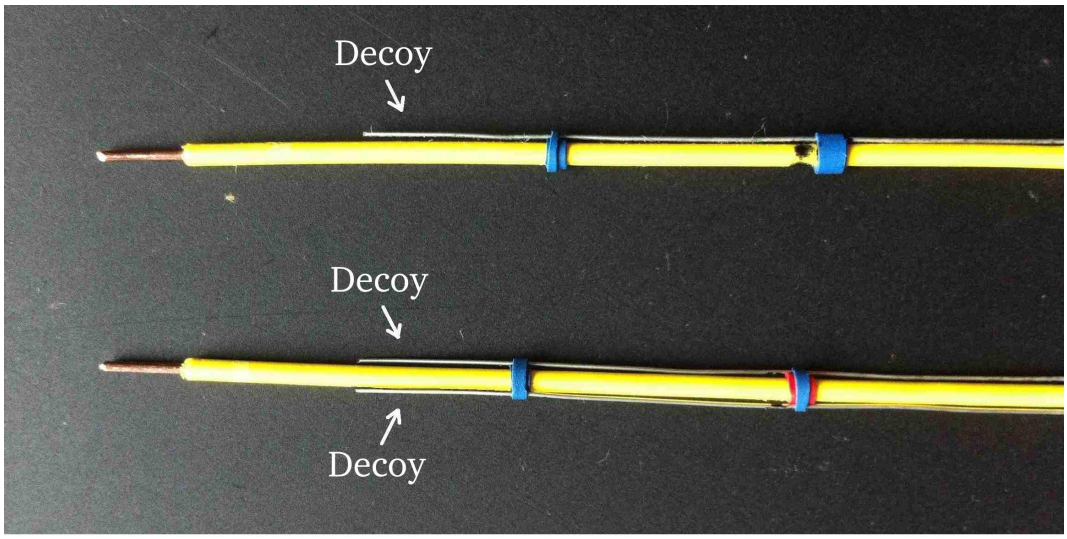

Figure 7.7: *Test leads comprising a single decoy (top) and pair of decoys (bottom) were constructed from* 800 µm *dia. copper wire with plastic insulation* 350 µm *in thickness covering all but* 6 mm *from one end (the electrode). Bare* 400 µm *dia. copper decoy(s) are adhered to the exterior of the lead insulation.*

Referring to Fig. 7.7, example leads with diameters and insulation thickness as previously reported in [60, 67, 74] were fitted with bare decoy filars. This arrangement will be used to compare simulation with measurement in both an MRI machine and in our lab setup. Alignment of the temperature probe to the bared end of the lead under test is shown in Fig. 7.8. This type of probe is standard for monitoring implant heating in MRI machines, and is not expected to have a significant impact on the RF field and level of heating.

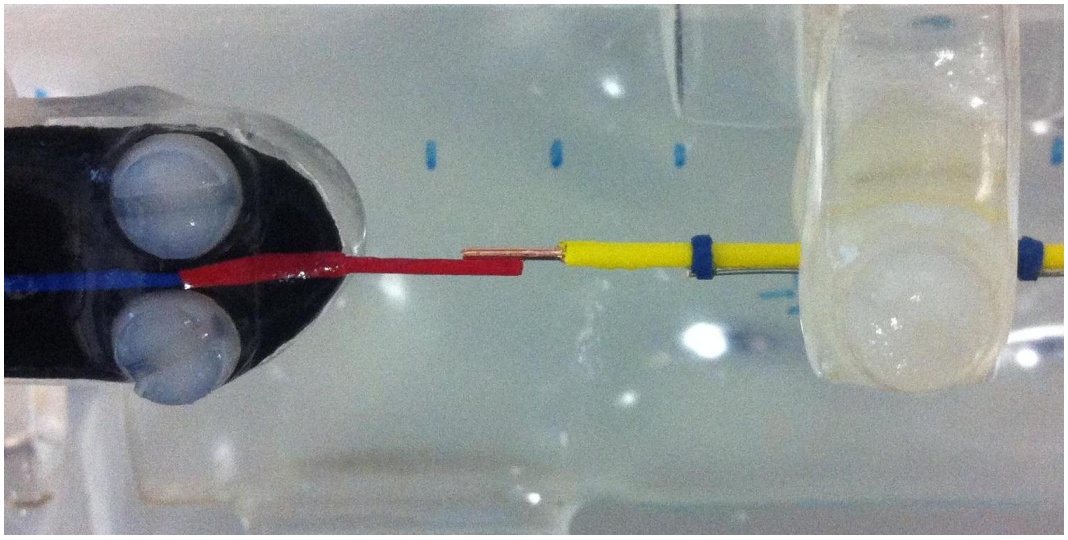

Figure 7.8: *GaAs-based fiber-optic temperature probe aligned with the bared end of the test lead.*

Measurements of peak distal heating were made on wires with a single $0.6\,l$ decoy and a $0.9\,l$ decoy. Results appear in Fig. 7.9. In the case of the shorter decoy, a temperature rise of less than 6℃ over the entire lead is observed. The fractionally-longer decoy produces a smaller temperature rise—just 2℃ when the lead length is short. The simulated predictions taken from above overlay measured data to permit visual comparison. Agreement is excellent.

As stated previously, there is a special case of when the distal electrode is not the source of highest heating. When the length of the $0.9\,l$ lead is short the decoy itself generates slightly higher heating than the distal electrode. This is indicated in the figure by the result labelled "*corrected*" as shown in Fig. 7.9b. A small elevation occurs for lead lengths up to 22.5 cm. Measurement of the decoy was not performed due to difficulty in measuring the temperature of such a large volume.

A second decoy of identical length leads to an even greater reduction in distal heating. Referring to Fig. 7.10, it can be seen that the effectiveness is similar to the shielded, insulated wire in Fig. 7.2. A rise of just 0.5℃ is measured when the lead is 30 cm long with $0.9\,l$ decoys. This represents only 3% of the heating observed in the case of a plain implant lead as presented in Fig. 7.2. Decoy temperatures slightly warmer than the distal electrode are again predicted for the $0.9\,l$ lead, for lead lengths up to 22.5 cm.

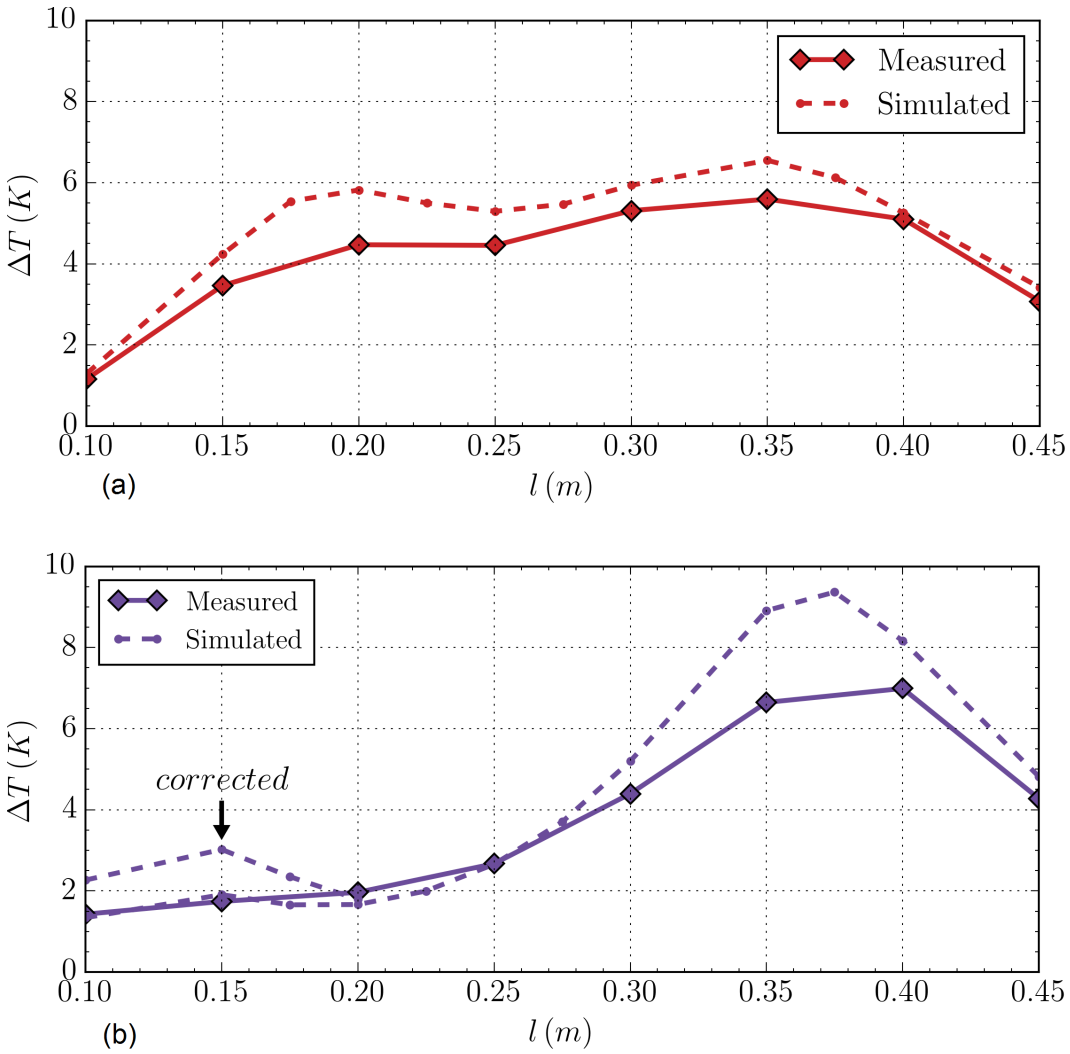

Figure 7.9: *Measured distal heating ($t_f = 5\,\text{min}$, $\text{SAR}_{wb} = 1\,\text{W/kg}$) of single decoy-enhanced test leads, with decoy-to-lead length ratios of (a) $0.6\,l$ and (b) $0.9\,l$.*

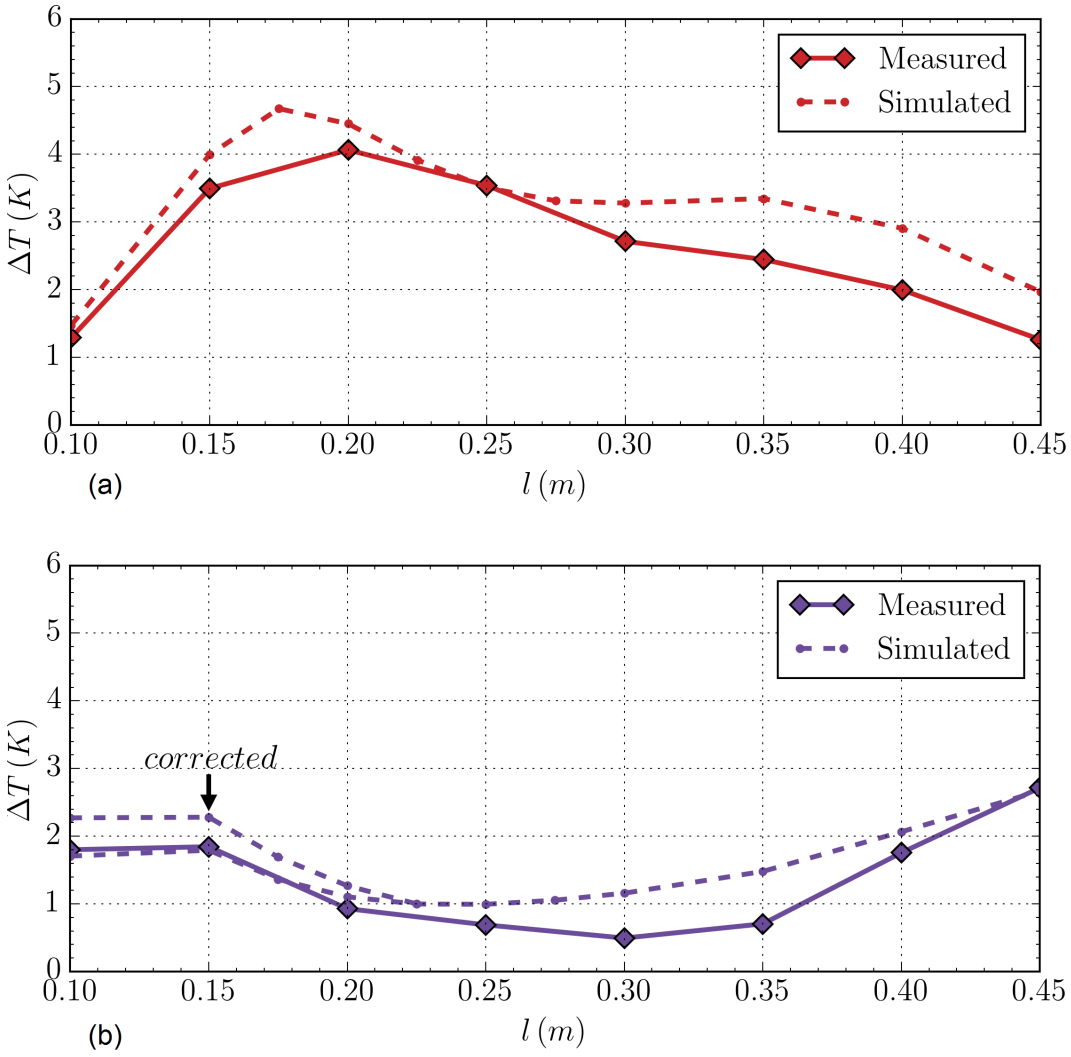

Figure 7.10: *Measured distal heating ($t_f = 5\,\mathrm{min}$, $\mathrm{SAR}_{wb} = 1\,\mathrm{W/kg}$) of dual decoy-enhanced test leads, with decoy-to-lead length ratios of (a) $0.6\,l$ and (b) $0.9\,l$.*

7.1.5 Multi-Electrode Implant Lead

We now expand our analysis to complex lead structures that more closely represent commercial implant electrode leads. Implant leads for neurostimulation like the type shown in Fig. 7.1 typically employ 4–8 electrodes for stimulus. Literature concerning the RF effects of such leads is limited to fixed lengths [30, 32, 34, 79]. With recent development of the lab test method, extensive testing of multi-electrode leads has become feasible. We will now explore the effect of increasing the electrode count and further verify the decoy approach.

Lead Types

Single, four, and eight electrode versions were constructed with dimensions according to the SCS lead in Fig. 7.1, but with slightly larger outer diameters of 1.6 mm. Straight lengths of enamel coated copper wire were soldered to each cylindrical electrode. The bundle of filars was sealed within a plastic sheath 350 µm in thickness. Epoxy resin was applied to seal the opposing end of the sheath.

To avoid any influence on heating from varied insulation thickness or lead diameter, different diameters for the filars were chosen such that the sheath thickness and outside diameter for each lead type was equivalent. Design details for each lead type are summarized in Table 7.1. A second eight electrode lead was also constructed but with the addition of two $0.9\,l$ 400 µm diameter decoys adhered on either side of the lead.

Measurement

Fig. 7.11 depicts the GaAs-based temperature probes aligned to the distal electrodes of the 45 cm eight electrode lead in the lab. Lead length is measured from the mid-point between the electrode set (between electrodes 4 and 5 for the 8-electrode version), to the opposite end of the lead. With the thermometry system supporting only two probes, the heating of just two electrodes could

Table 7.1: *Details of the different lead types.*

No. of electrodes	Cross section	Filar dia. (mm)
1	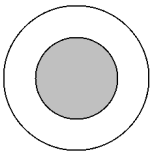	0.80
4	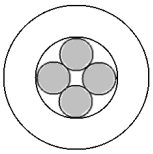	0.45
8	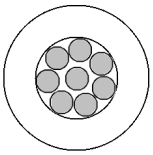	0.30
8	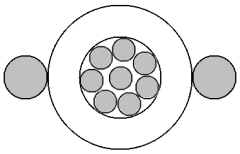	0.30 w/ 0.40 decoys

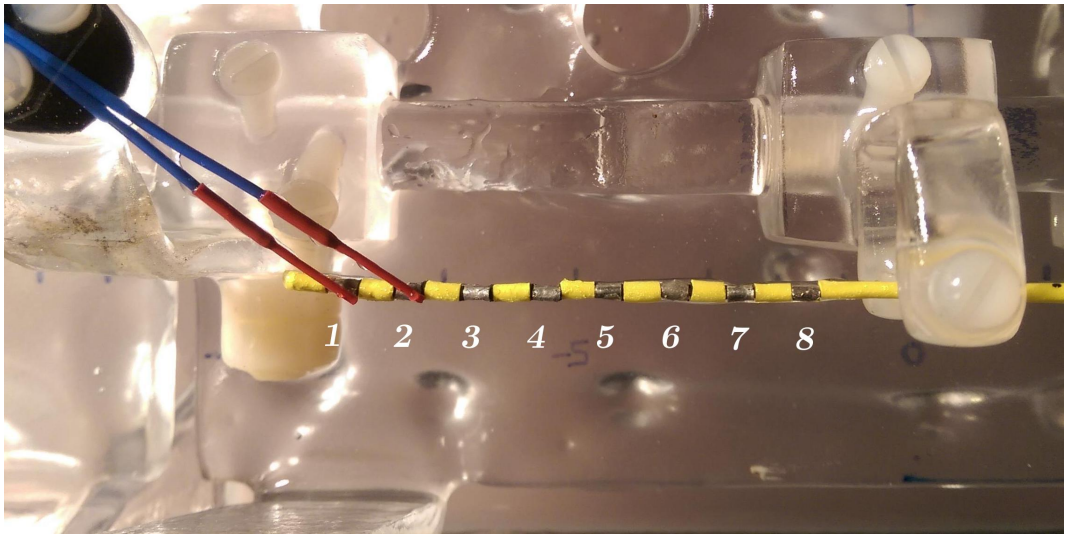

Figure 7.11: *Temperature probes aligned and in direct contact with the first two electrodes of the implant lead. Assigned numbering starts from "1" at the most distal electrode.*

be measured at any one time. Following each complete set of measurements, the end of the lead was cut to form a new length, epoxy resin applied, and the measurement procedure repeated.

The measured heating for the lead with the single electrode is shown in Fig. 7.12a.

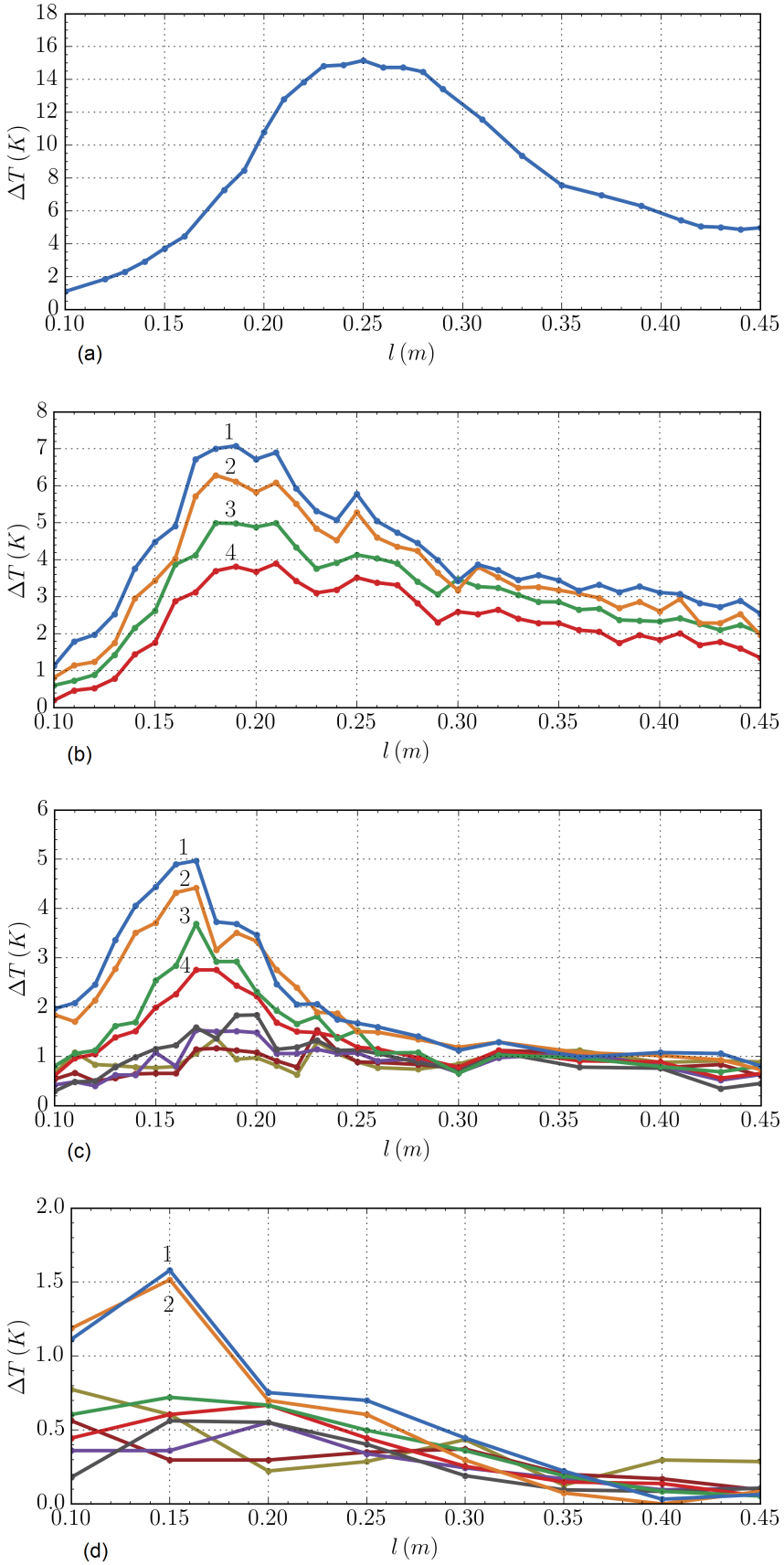

Figure 7.12: *Measured distal heating ($t_f = 5\,\mathrm{min}$, $\mathrm{SAR}_{wb} = 1\,\mathrm{W/kg}$) of an implant lead with (a) a single electrode (b) four electrodes (c) eight electrodes (d) eight electrodes with two $0.9\,l$ decoys.*

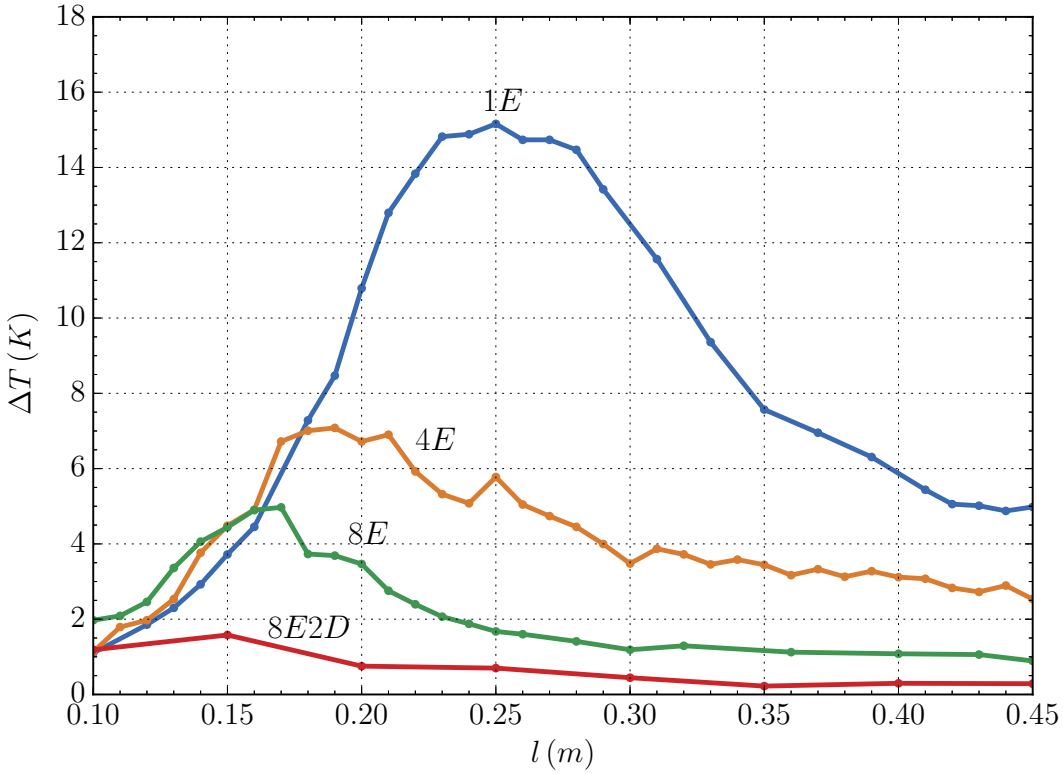

Figure 7.13: *Highest heating for the four and eight electrode versions compared with the single electrode lead.*

The highest temperature occurs when the length is 25 cm, consistent with Fig. 7.2. Figs. 7.12b and 7.12c, show measurements for the four and eight electrode versions, respectively. It is apparent from the figures that increased electrode counts lead to lower peak heating, where the most distal electrodes account for the highest heating. Fig. 7.12d shows the safety gained from adding two $0.9\,l$ decoys to the eight electrode lead. Minimal heating occurs when the lead is short but is still within ICNIRP limits. The results are compiled into Fig. 7.13 to show the differences between maximum heating observed for each lead type.

7.1.6 Discussion

Implant leads with higher electrode counts tend to generate less RF heating. This can be attributed to mutual coupling effects between individual filars and the apparent increase in electrode surface area gained from closely spaced electrodes. Electrodes other than the most distal ones produce the least amount of heating and can effectively be omitted from tests.

To virtually eliminate all heating and achieve MRI safety, leads can be fitted with external decoys to help dampen the induced currents generated in the lead filars. The modification is simple and cost-effective, and has no impact on the normal operation of the neurostimulation device. Extensive testing following [80] with more complex human phantoms is recommended including an assessment on decoy performance versus lead position/configuration.

Further improvement to the safety margin may be possible by increasing the ac resistance and surface area of the lead filars and decoys through the use of resistive materials [41, 60] and surface roughening techniques [4].

7.1.7 Conclusion

We presented a novel technique to ameliorate the potentially-hazardous heating of implanted conductors that can occur in MRI scanners. Simulation of local heating around the distal end of a filar agree with measurements made in a torso phantom. This mechanism of mutual coupling to a damped filar or "decoy" can be deployed in conjunction with other, previously-reported techniques. It is expected the approach will lead to MRI-safe leads for use with spinal cord and deep brain implantable stimulators.

7.1.8 Acknowledgement

The authors would like to acknowledge Saluda Medical for their valuable support and Stephen Butler from Midland MRI for assisting with MRI experiments.

7.2 Further Results and Discussion (Unpublished)

7.2.1 Thinsulation on Decoy Filars

A polymer coating on the decoy filar is desirable for biocompatibility reasons. Application of such material enables the use of less expensive and non-biocompatible materials for the decoy conductor including ferromagnetic or electrically resistive conductors as options. Provided the insulating layer is just a few tens of microns in thickness (Thinsulation), the decoy filar will still provide damping of RF currents in the main filar as was alluded to in figure 7.4c. Thinsulation provides a low impedance layer between the decoy filar and surrounding tissue, allowing RF conduction akin to its bare equivalent. The decoy's effectiveness at damping however, depends on the thickness of the decoy's insulating layer.

The simulations of peak distal and decoy heating for leads with single $0.9l$ decoys from section 7.1.4 were repeated but with varying thicknesses of Thinsulation applied to the decoy filars. The results are in figure 7.14. As shown, the inclusion of Thinsulation alters the behaviour of the decoy slightly and actually enhances RF safety, particularly for longer lead lengths where a reduction in distal heating of up to 86% is possible. Decoy heating is also improved overall, maintaining a lower temperature than the distal electrode at all lead lengths.

Only one measurement was obtained on a test lead having a thinly insulated decoy. In fact it was the first time that the performance of the decoy invention was proven by measurement. Out of all the test leads from chapter 3, the lead that presented the highest measured heating was selected for testing with the decoy. Figure 7.15 shows the result alongside the distal heating produced by the same lead in the absence of a decoy. Despite limited data, the measurements illustrate the effectiveness of the decoy filar, and confirm the viability of a Thinsulation coating.

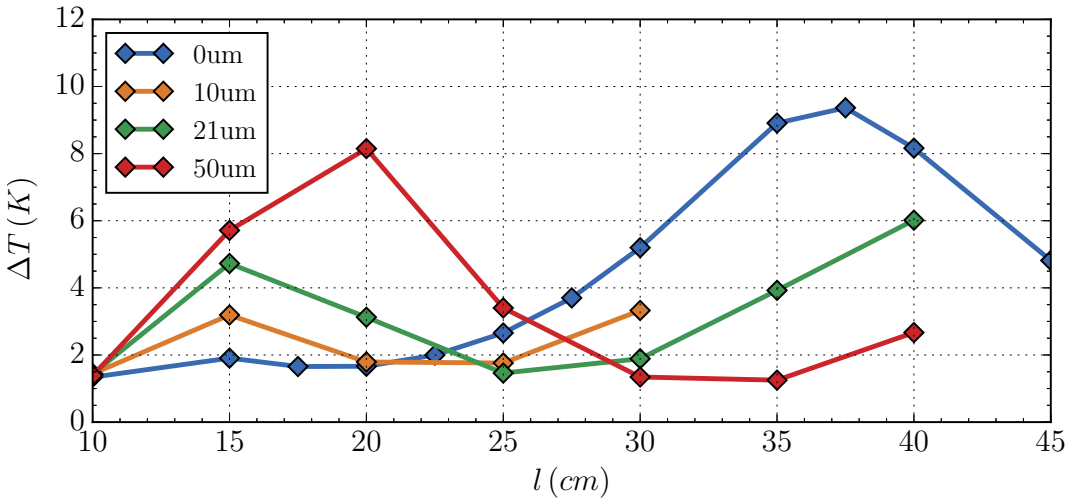

(a)

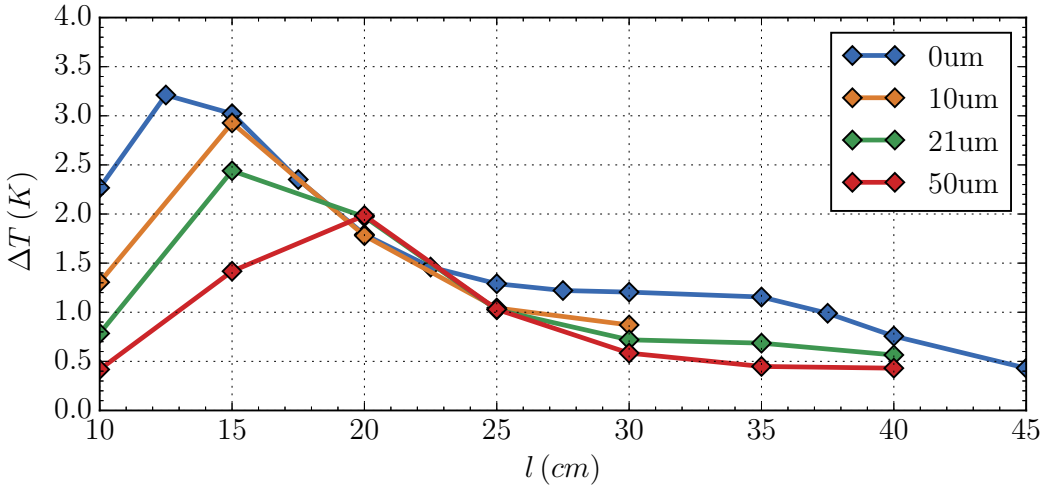

(b)

Figure 7.14: *The distal heating (a) and decoy heating (b) simulated for various leads fitted with single* $0.9l$ *decoys. The decoy insulation thickness ranges from* $10\,\mu m$ *to* $50\,\mu m$*, with a permittivity of* $\epsilon_r = 2.54$*. The heating for a bare decoy is also shown. The insulation thickness on the main filar is fixed to* $350\,\mu m$*.*

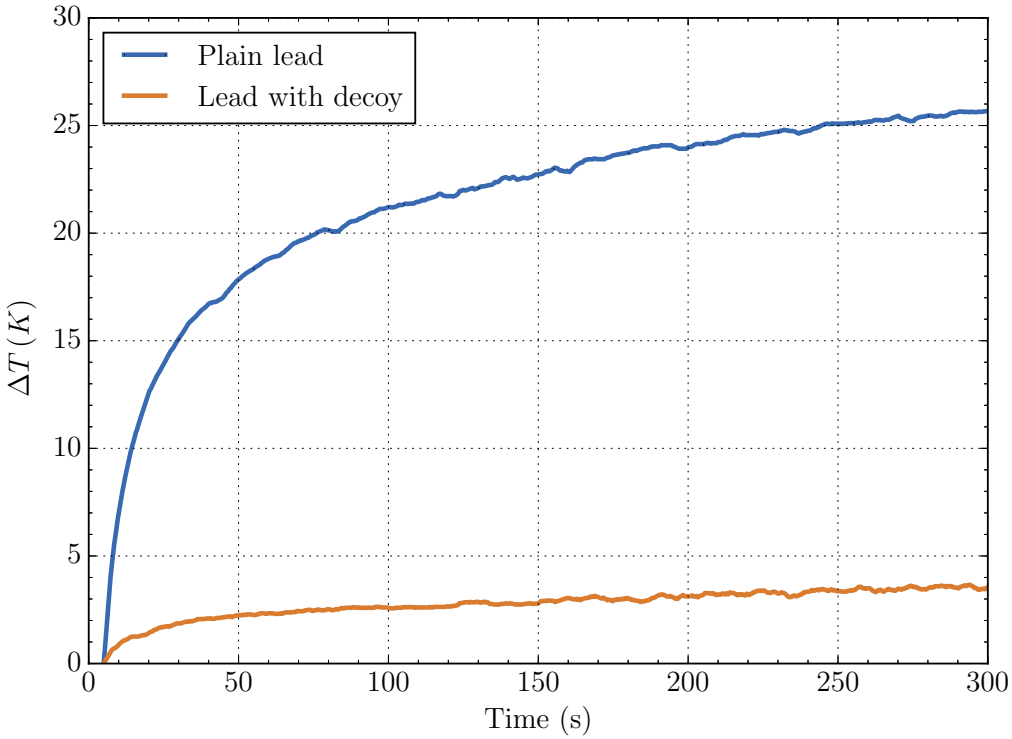

Figure 7.15: *The distal heating measured during a 3T MRI scan for test leads with and without a thinly insulated decoy. The test lead was* 27 cm *in length with* 700 μm *of plastic insulation. The decoy was* 21 cm *long, or* 0.78l*, with an enamel coating approximately* 21 μm *in thickness. Temperature readings were acquired with a sample rate of* 4 Hz *and averaging set to 20 times.*

7.2.2 Resistive Decoy Filars

There was speculation during the early development of the decoy invention that a resistive decoy by way of a uniform resistive conductor or a series of discrete resistors along its length, may offer improved RF damping over ordinary highly conductive types [3, 81]. Nevertheless, recent simulated results suggest that an external resistive decoy is unlikely to offer any improvement in RF safety (figure 7.16). The lossy material impedes the flow of current in the decoy and makes it less effective at dissipating mutually-coupled energy in

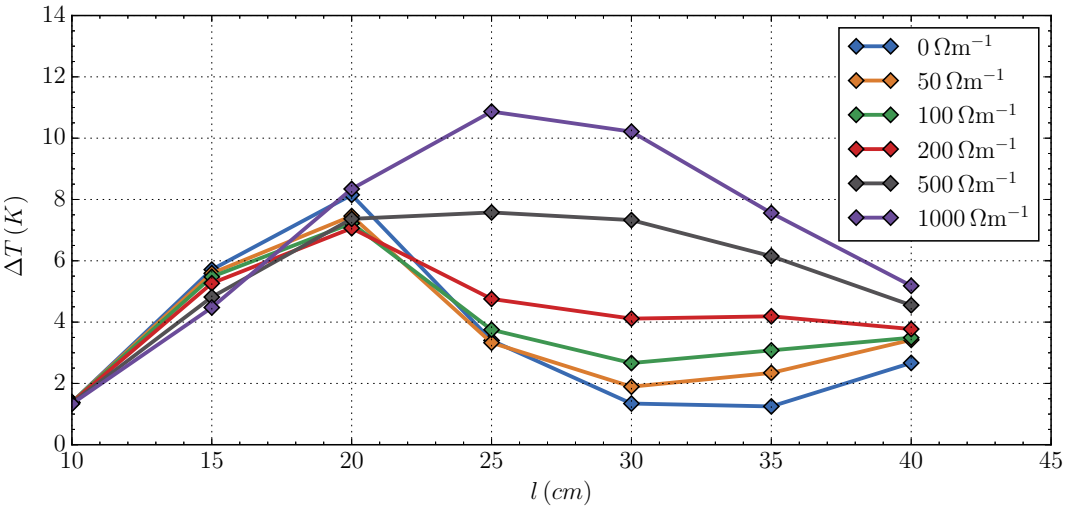

(a)

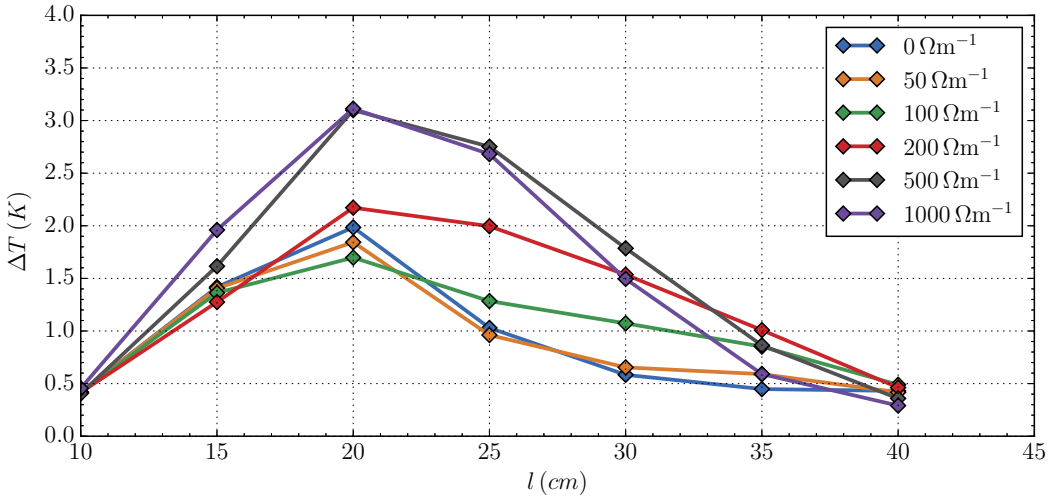

(b)

Figure 7.16: *The distal heating (a) and decoy heating (b) simulated for various leads fitted with single* $0.9l$ *decoys of varying conductivities. The decoy is coated in Thinsulation with a thickness of* $50\,\mu m$.

the surrounding tissue. The only benefit of a resistive decoy may be for one that is covered by thick insulation, as would be the case of a decoy conductor implemented deep within the implant lead jacket (e.g. in place of the surgical stylet). In this instance, energy dissipation in a resistive decoy of a few tens of ohms per meter may sufficiently exceed that of which occurs in the surrounding tissue from RF shunting (see table 3.1), resulting in an overall increase in damping and reduction in distal heating.

7.2.3 Multi-Electrode Lead Model

The single electrode lead is a useful model for proof of concept simulations. However as shown earlier, it has limited accuracy when predicting the peak distal heating of multi-electrode leads. A new approximation is proposed in figure 7.17. The model is similar to the original insulated wire model in chapter 2 but instead incorporates a plurality of separated electrodes in contact with a single insulated filar. The electrode dimensions and spacing are selected according to commercial implant lead specifications, with the wire diameter equivalent to the combined diameters of the filar bundle.

Figure 7.18 compares measurement of the 8-electrode, 8-filar lead from section 7.1.5 to the simulation of an 8-electrode, single-filar approximation. The heating of electrodes 1-4 and 5-8 are shown in separate figures to help reduce ambiguity. The results are encouraging. The model resembles a closer approximation to the multi-electrode lead without significantly increasing the geometric complexity or simulation run time that would normally result from modeling multiple filars. Further validation by measurements in an MRI machine is recommended.

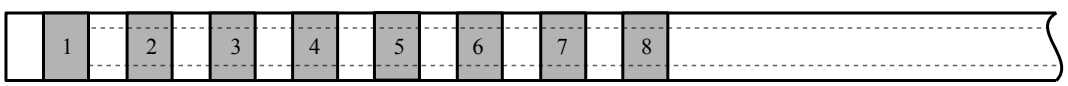

Figure 7.17: *Model for simulating multi-electrode leads. Multiple lead filars are approximated by a single filar that extends and connects to each distal electrode. Insulation covers the filar and provides spacing between each electrode.*

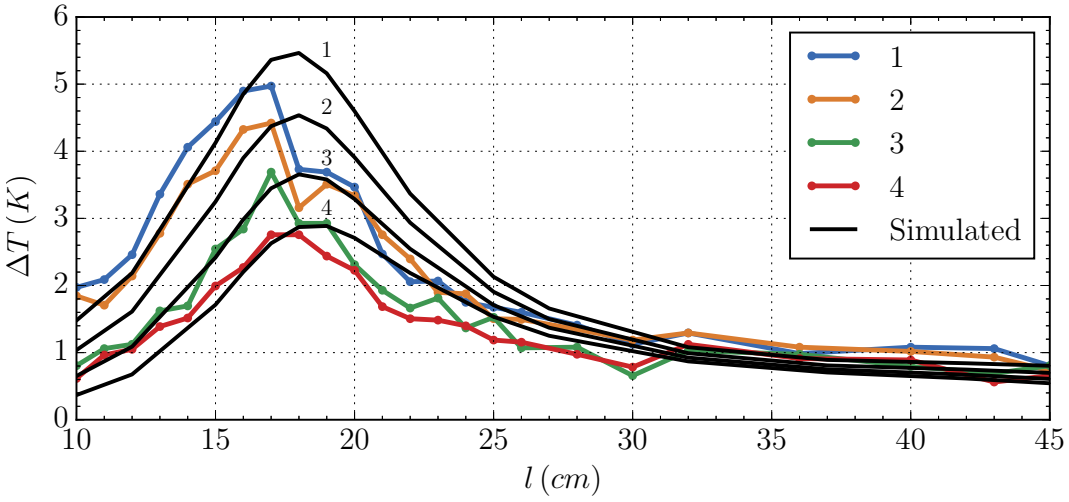

(a)

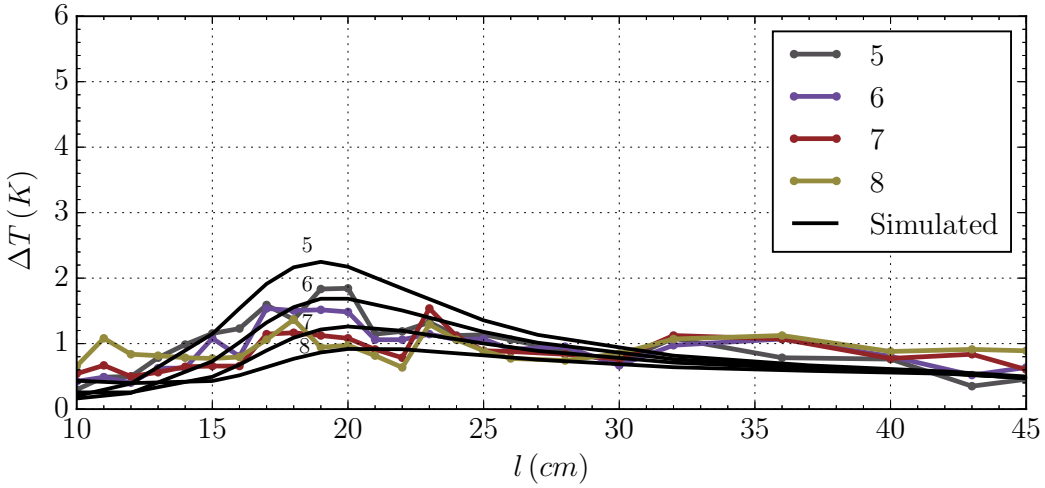

(b)

Figure 7.18: *The simulated heating at the distal electrodes (a) 1-4 and (b) 5-8, of a multi-electrode, single filar lead, compared with measurement of the multi-electrode, multi-filar lead from section 7.1.5. Note that decoy filars were not included.*

7.2.4 Impact of Electrode Length on Distal Heating

With the above multi-electrode lead model, the impact of electrode length on distal heating was explored. Simulations were performed on leads having eight electrodes ranging in equal length from 3–6 mm. Accordingly, equal spacers having lengths ranging from 4–1 mm were chosen, such that the combined length of the electrodes and spacers was invariant and equal to 56 mm for each simulation sequence. The results are in figure 7.19. Unsurprisingly, peak distal heating was less concentrated for the longer electrodes. This is because the larger surface area of tissue in contact with each electrode is more effective at

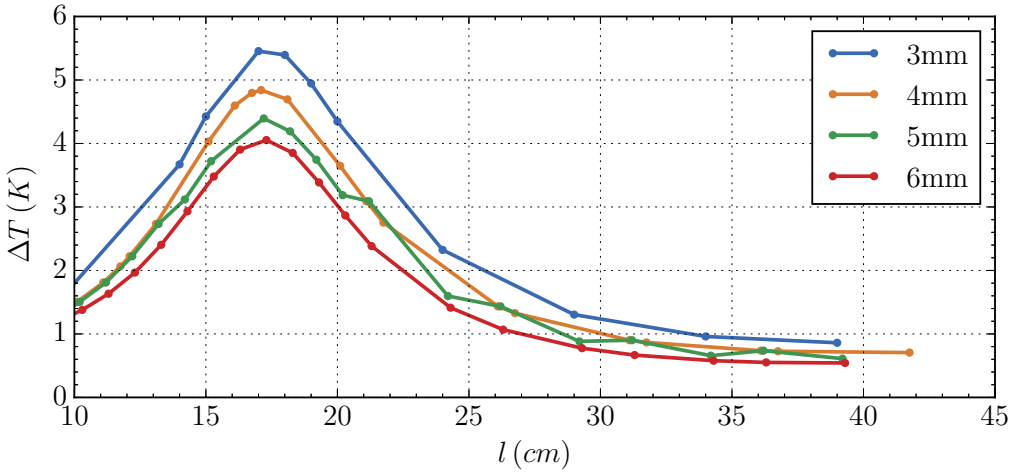

Figure 7.19: *The simulated heating at the most distal electrode when the electrode length is varied. Simulations were performed using the 8-electrode, single filar model.*

dispersing and dissipating the RF currents induced in the filars. Doubling the electrode length from 3mm to 6mm results in a 25% reduction in distal heating at the resonant length. This strategy may be especially useful in designs where only a marginal reduction in RF heating is necessary to meet safety limits. If increasing the length of the electrodes is not possible for neurostimulation functionality reasons, simply including additional dummy electrodes along the lead length may offer a similar improvement.

7.2.5 Thinsulation on Distal Electrodes

While filars with thinner insulation have generally been shown to produce lower distal heating than those with thicker insulation, there is an exception for when the filar is *completely* insulated with no low resistance connections to the surrounding tissue. This is apparent in figure 7.14b where the heating of a decoy filar was improved through the application of a Thinsulation layer. Increasing the thickness of the layer led to a further reduction in heating.

Similarly, coating the distal electrodes of an implant lead with a thin layer of insulation can lower distal heating. The simulation of the multi-electrode lead from section 7.2.3 was repeated but with a 50 μm plastic coating applied over each electrode. The results are shown in figure 7.20. At the resonant length, peak distal heating is reduced by 33% when a Thinsulation layer is

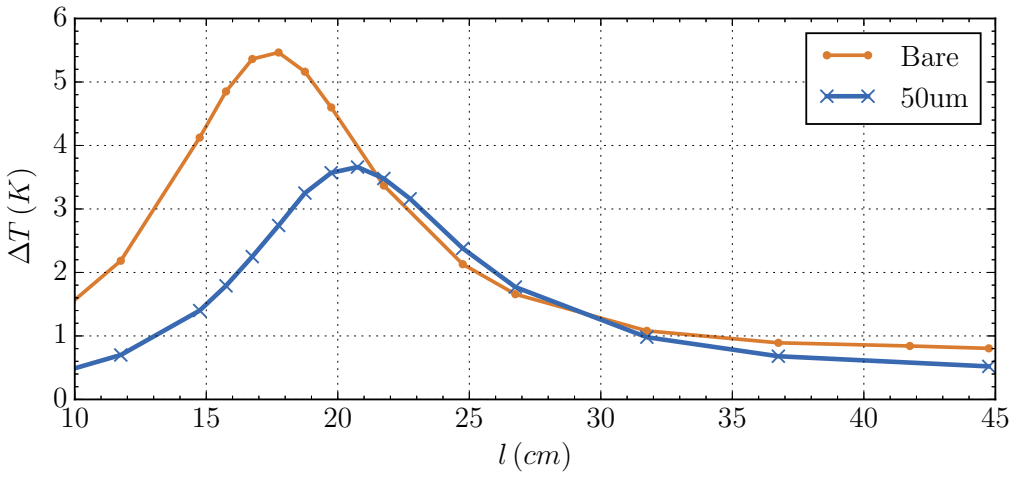

Figure 7.20: *The simulated heating at the most distal electrode when each electrode is coated with* 50 μm *of plastic insulation. The distal heating for the same lead with bare electrodes is also shown. Simulations were performed using the 8-electrode, single filar model.*

present. The insulation helps to reduce the magnitude of the distal currents escaping into the tissue and therefore the level of tissue heating. However, such design changes will likely effect the ability of the neurostimulator to deliver sufficient stimulus to neural tissue. Nevertheless, through modifications of the stimulation signal amplitude and waveform, this may be a viable approach.

Chapter 8

International Patents

8.1 "Implant Conductor Assembly with Improved Radio Frequency Properties"

Steven McCabe and Jonathan Scott
Department of Engineering, The University of Waikato, Hamilton, New Zealand

National filing on 16 Nov. 2015.
International filing on 16 Nov. 2016.

A patent describing the *Decoy Filar* invention. An excerpt is provided below. For the full document please refer to [3].

(12) INTERNATIONAL APPLICATION PUBLISHED UNDER THE PATENT COOPERATION TREATY (PCT)

(19) World Intellectual Property Organization
International Bureau

(43) International Publication Date
26 May 2017 (26.05.2017)

WIPO | PCT

(10) International Publication Number
WO 2017/086805 A1

(51) International Patent Classification:
A61N 1/08 (2006.01)

(21) International Application Number:
PCT/NZ2016/050182

(22) International Filing Date:
16 November 2016 (16.11.2016)

(25) Filing Language: English

(26) Publication Language: English

(30) Priority Data:
714212 16 November 2015 (16.11.2015) NZ

(71) Applicant: **UNIVERSITY OF WAIKATO** [NZ/NZ]; Hillcrest Road, Hamilton, 3216 (NZ).

(72) Inventors: **MCCABE, Steven Owen**; 2a Paremata Crescent, Paremata, Porirua, 5024 (NZ). **SCOTT, Jonathan Brereton**; 26 Cranwell Place, Hillcrest, Hamilton, 3216 (NZ).

(74) Agents: **MURPHY, Simon John** et al.; Level 10, 21 Queen Street, Auckland, 1010 (NZ).

(81) Designated States *(unless otherwise indicated, for every kind of national protection available)*: AE, AG, AL, AM, AO, AT, AU, AZ, BA, BB, BG, BH, BN, BR, BW, BY, BZ, CA, CH, CL, CN, CO, CR, CU, CZ, DE, DJ, DK, DM, DO, DZ, EC, EE, EG, ES, FI, GB, GD, GE, GH, GM, GT, HN, HR, HU, ID, IL, IN, IR, IS, JP, KE, KG, KN, KP, KR, KW, KZ, LA, LC, LK, LR, LS, LU, LY, MA, MD, ME, MG, MK, MN, MW, MX, MY, MZ, NA, NG, NI, NO, NZ, OM, PA, PE, PG, PH, PL, PT, QA, RO, RS, RU, RW, SA, SC, SD, SE, SG, SK, SL, SM, ST, SV, SY, TH, TJ, TM, TN, TR, TT, TZ, UA, UG, US, UZ, VC, VN, ZA, ZM, ZW.

(84) Designated States *(unless otherwise indicated, for every kind of regional protection available)*: ARIPO (BW, GH, GM, KE, LR, LS, MW, MZ, NA, RW, SD, SL, ST, SZ, TZ, UG, ZM, ZW), Eurasian (AM, AZ, BY, KG, KZ, RU, TJ, TM), European (AL, AT, BE, BG, CH, CY, CZ, DE, DK, EE, ES, FI, FR, GB, GR, HR, HU, IE, IS, IT, LT, LU,

[Continued on next page]

WO 2017/086805 A1

(54) Title: IMPLANT CONDUCTOR ASSEMBLY WITH IMPROVED RADIO FREQUENCY PROPERTIES

(57) Abstract: In one aspect the invention provides an implant conductor lead assembly which includes an electrode lead, and at least one field target conductor. The field target conductor(s) is located adjacent to the electrode lead to mutually couple the field target conductor to the electrode lead. The electrode lead acts to concentrate electromagnetic fields in the vicinity of the implant conductor assembly towards the field target conductor or conductors.

Figure 2

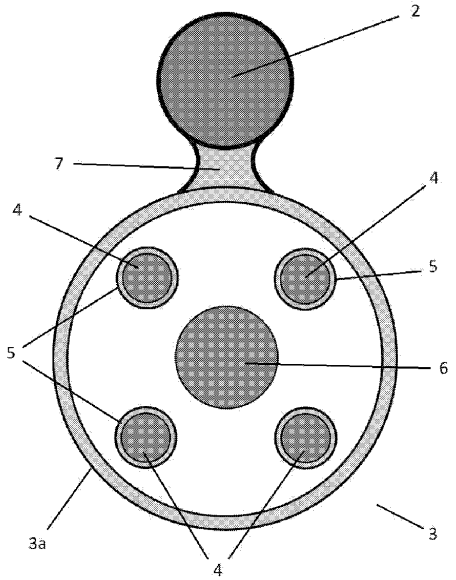

WO 2017/086805 A1

LV, MC, MK, MT, NL, NO, PL, PT, RO, RS, SE, SI, SK, SM, TR), OAPI (BF, BJ, CF, CG, CI, CM, GA, GN, GQ, GW, KM, ML, MR, NE, SN, TD, TG).

Declarations under Rule 4.17:

— *of inventorship (Rule 4.17(iv))*

Published:

— *with international search report (Art. 21(3))*

— *before the expiration of the time limit for amending the claims and to be republished in the event of receipt of amendments (Rule 48.2(h))*

8.2 Original Specifications for the Decoy Invention

Decoy Concept **3-Aug-15**
by S. McCabe & J. Scott

Improved MRI safety is achieved by attaching one or more bare (or thinly insulated) conductors ("decoy(s)") of predetermined length along the outside of the implant lead jacket.

(1) The optimum length of the decoy to achieve the highest level of safety will depend on certain properties of the implant lead wire. Therefore, the decoy may end up being shorter, longer, or the same in length as the implant lead wire.
(2) The decoy could be comprised of uniform length
(3) The decoy may be centred with the implant lead wire or offset by some amount.
(4) The diameter of the decoy(s) may be similar but not limited to that of the implant lead conductors e.g. 150microns.
(5) The decoy may be cylindrical, ribbon-like, braided, etc,
(6) The Decoy may be a straight conductor or coiled (but not wrapped around the lead).

Optional components:
(7) The decoy could be comprised of multiple segments.
(8) Multiple decoys around the insulating jacket may also be included. The lengths may or may not be equivalent.
(9a) A layer of thin insulation could also be included on the decoy(s).
(9b) Contact of the insulated decoy to the tissue (if necessary) could be made with one or more electrodes anywhere along the length.
(10) If multiple decoys are implemented, electrical contact between them may be made at certain locations. For example, connections between the decoys at each end will form a folded-dipole type configuration.
(11) The decoy(s) may make electrical contact with the metal housing of the Impulse Generator (IPG).

8.3 "A Surgical Implant Conductor with Increased Radio Frequency Alternating Current Resistance"

Steven McCabe and Jonathan Scott
Department of Engineering, The University of Waikato, Hamilton, New Zealand

National filing on 29 May. 2015.
International filing on 27 May. 2016.

A patent describing the *Roughened Filar* invention. An excerpt is provided below. For the full document please refer to [4].

(12) INTERNATIONAL APPLICATION PUBLISHED UNDER THE PATENT COOPERATION TREATY (PCT)

(19) World Intellectual Property Organization
International Bureau

(43) International Publication Date
8 December 2016 (08.12.2016)

WIPO | PCT

(10) International Publication Number
WO 2016/195513 A1

(51) International Patent Classification:
A61N 1/08 (2006.01) *A61N 1/05* (2006.01)
A61N 1/16 (2006.01)

(21) International Application Number:
PCT/NZ2016/050089

(22) International Filing Date:
27 May 2016 (27.05.2016)

(25) Filing Language: English

(26) Publication Language: English

(30) Priority Data:
708633 29 May 2015 (29.05.2015) NZ

(71) Applicant: **UNIVERSITY OF WAIKATO** [NZ/NZ]; Hillcrest Road, Hamilton, 3216 (NZ).

(72) Inventors: **MCCABE, Steven Owen**; 2a Paremata Crescent, Paremata, Porirua, 5024 (NZ). **SCOTT, Jonathan Brereton**; 26 Cranwell Place, Hillcrest, Hamilton, 3216 (NZ).

(74) Agents: **MURPHY, Simon John** et al.; Level 10, 21 Queen Street, Auckland, 1010 (NZ).

(81) Designated States *(unless otherwise indicated, for every kind of national protection available)*: AE, AG, AL, AM, AO, AT, AU, AZ, BA, BB, BG, BH, BN, BR, BW, BY, BZ, CA, CH, CL, CN, CO, CR, CU, CZ, DE, DK, DM, DO, DZ, EC, EE, EG, ES, FI, GB, GD, GE, GH, GM, GT, HN, HR, HU, ID, IL, IN, IR, IS, JP, KE, KG, KN, KP, KR, KZ, LA, LC, LK, LR, LS, LU, LY, MA, MD, ME, MG, MK, MN, MW, MX, MY, MZ, NA, NG, NI, NO, NZ, OM, PA, PE, PG, PH, PL, PT, QA, RO, RS, RU, RW, SA, SC, SD, SE, SG, SK, SL, SM, ST, SV, SY, TH, TJ, TM, TN, TR, TT, TZ, UA, UG, US, UZ, VC, VN, ZA, ZM, ZW.

(84) Designated States *(unless otherwise indicated, for every kind of regional protection available)*: ARIPO (BW, GH, GM, KE, LR, LS, MW, MZ, NA, RW, SD, SL, ST, SZ, TZ, UG, ZM, ZW), Eurasian (AM, AZ, BY, KG, KZ, RU, TJ, TM), European (AL, AT, BE, BG, CH, CY, CZ, DE, DK, EE, ES, FI, FR, GB, GR, HR, HU, IE, IS, IT, LT, LU, LV, MC, MK, MT, NL, NO, PL, PT, RO, RS, SE, SI, SK, SM, TR), OAPI (BF, BJ, CF, CG, CI, CM, GA, GN, GQ, GW, KM, ML, MR, NE, SN, TD, TG).

Declarations under Rule 4.17:

— *of inventorship (Rule 4.17(iv))*

Published:

— *with international search report (Art. 21(3))*

WO 2016/195513 A1

(54) Title: A SURGICAL IMPLANT CONDUCTOR WITH INCREASED RADIO FREQUENCY ALTERNATING CURRENT RESISTANCE

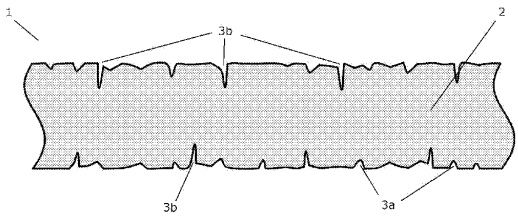

Figure 3a

(57) Abstract: In one aspect the invention provides a surgical implant conductor formed from a length of conductive material which exhibits increased radio frequency alternating current resistance. This conductive material defines an exterior surface where at least a portion of the exterior surface of the conductor defines a region with a roughened surface. Preferably the roughening of the exterior surface increases the area of the exterior surface when compared to a non-roughened surface, resulting in a reduction in the effective cross-section area of the conductor used to transport alternating currents.

Chapter 9

Surface Filar Invention

This chapter introduces an invention that uses the principle of thin insulation to gain implant leads MRI safety. Based on previous findings, further work by experimental measurements is needed to confirm its effectiveness. The work has not been published outside of this thesis.

9.1 Introduction

Typical implant leads for SCS and DBS comprise 4–16 filars extending from end to end, with each filar attached to a distal electrode. Each filar is individually insulated and contained within a thick plastic tube that forms the lead. Within the space where the filars run, room exists for a stylet to be temporarily inserted for surgical implantation. The thick insulation that separates the filar to the surrounding tissue makes the filars particularly susceptible to high RF absorption and distal heating during an MRI scan. A complete redesign of the implant lead is proposed to ameliorate this effect.

9.2 Concept

The proposed lead design incorporates one or more thinly insulated neurostimulation filars along the surface of a plastic tubular core. Within the core, is a hollow region for supporting a surgical stylet and additional neurostimulation

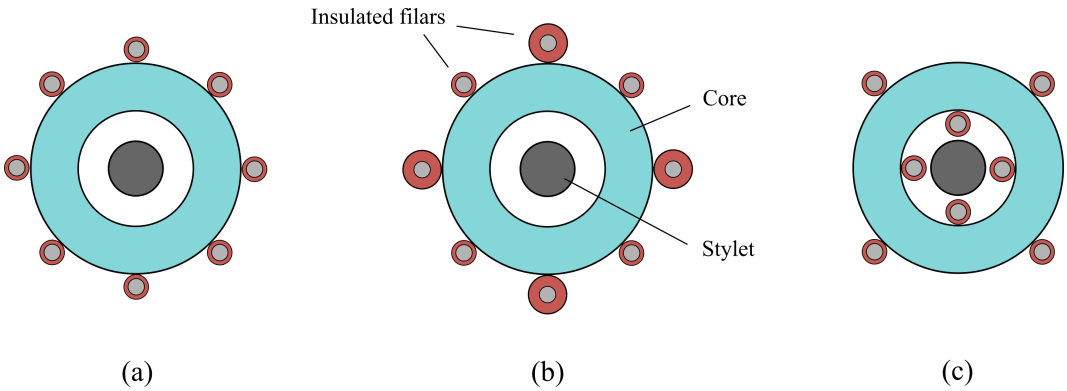

Figure 9.1: *Cross section of various leads with (a) all filars coated in thin insulation and attached to the lead surface, (b) mixture of filars coated in thin and thick insulation and attached to the lead surface, and (c) thinly insulated filars on the surface and others contained within the plastic core.*

filars. The thin insulation coating on the *Surface Filars* helps shunt induced RF currents toward the surrounding tissue over the length of the lead and away from the small distal electrodes, minimising distal heating. Any adjacent filars protected by thicker insulation, for example ones located inside of the plastic core, will also exhibit a similar reduction through the effects of mutual coupling as was shown in chapters 6 and 7.

Ideally, the thin insulation coating will be in the order of several tens of microns. Materials with higher permittivities ($\epsilon_r > 2.5$) will also help. See figures 3.7, 3.9, and 7.14.

The highest level of RF shunting will be gained when all of the lead filars are coated with thin insulation as shown in figure 9.1a. However, this can lead to significant inter-electrode capacitance in the order of several hundred pF/m between stimulus-driven electrode pairs[9]. For implants where such high capacitance could negatively impact an implant's ability to excite normal neurostimulation between electrode pairs, it may be preferable to thinly insulate just one of each electrode pair, i.e. half of the total number of filars. The remaining filars would then be protected by thicker insulation (figure 9.1b) or located in the lead core (figure 9.1c) to reduce the combined capacitance between the electrode pair. The principle is illustrated in figure 9.2.

[9] A rough approximation calculated from two series capacitors each having a capacitance according to equation 3.5.

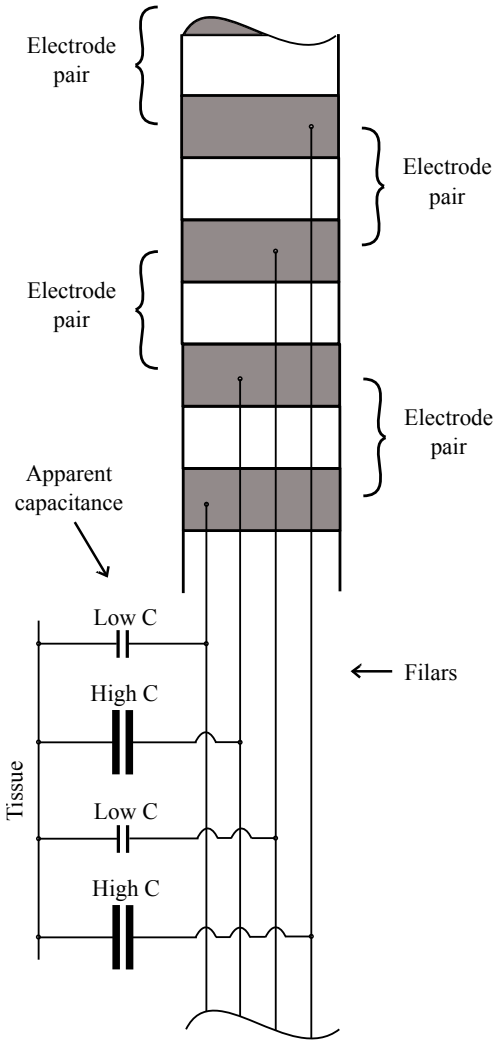

Figure 9.2: *Diagram showing the varying filar-to-tissue capacitances that arise from having alternating filar insulation thicknesses. The filars with a higher capacitance shunt induced RF currents into the tissue more effectively and reduce the magnitude of RF current through the distal electrodes.*

The surface filars can be arranged in various configurations about the plastic core as depicted by the examples in figure 9.3. Wound and woven types should exhibit greater RF shunting and lower distal heating than straight versions since the total length of the filars will be longer. However, this expectation needs to be confirmed by future work since previous studies only considered the effects of straight filars.

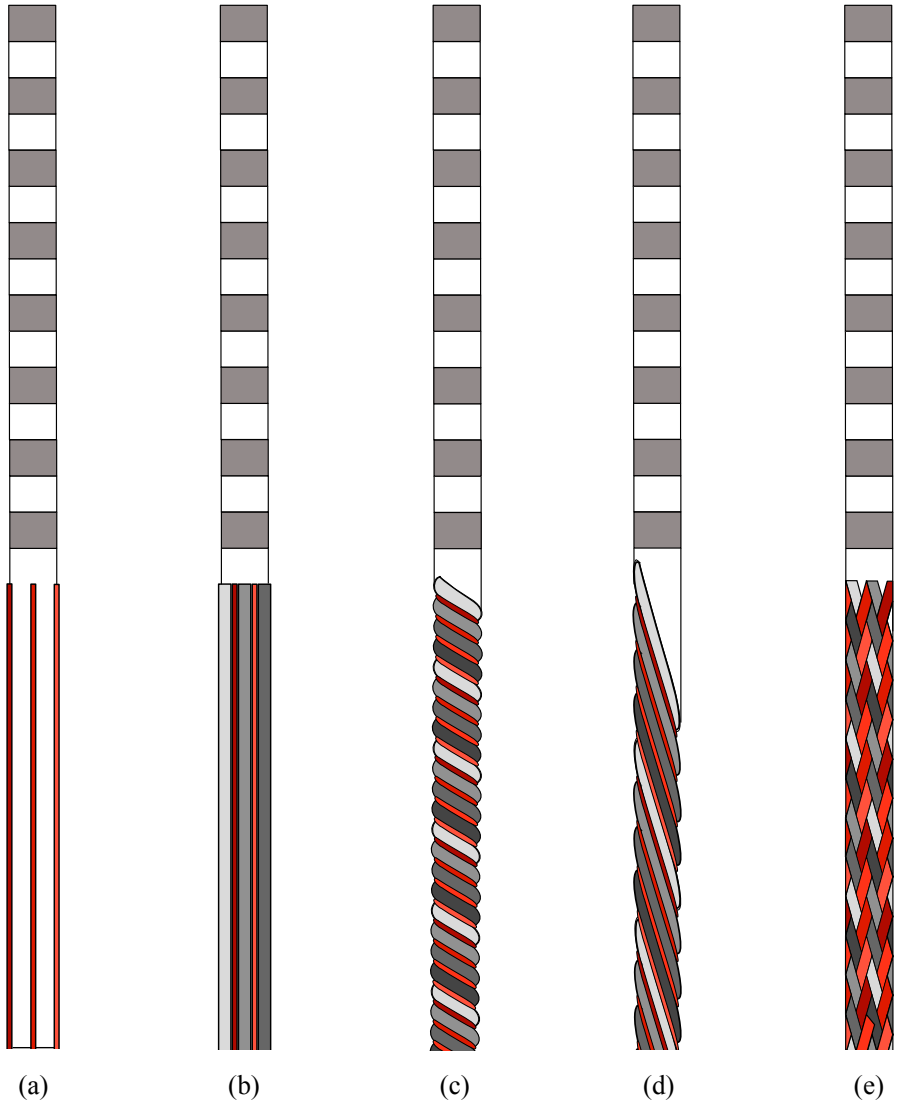

Figure 9.3: *Examples of different configurations for the surface filars: (a) straight, (b) straight with mixture of insulation types, (c) low-pitched winding, (d) high-pitched winding, (e) weave. Every second electrode is attached to a thinly insulated (surface) filar (coloured red to orange). Every other electrode is attached to filars with thick insulation (coloured light to dark grey) or filars contained within the plastic core.*

Chapter 10

RF Hazard Detector

This chapter presents two different methods for verifying the integrity of decoy protective filars on an implanted lead, to be carried out shortly before a patient is due to be scanned. The latter method can also be applied more broadly to other lead designs that do not rely on decoy filars. The work has not been published outside of this thesis.

10.1 Introduction

Implanted leads are susceptible to mechanical stresses from movement, and in some cases, may fail due to breakage of the conductive filars and/or insulation, leading to abnormal and ineffective therapeutic stimulation [82]. These failures have been shown to occur commonly near lead junctions, typically located near the midpoint of the overall lead structure.

The decoy filars presented in chapters 6 and 7 must support resonant currents at the MRI RF frequency in order to provide adequate damping to the main filars. Similarly, the Surface Filar design from chapter 9 relies upon current shunting along the entire length of one or more thinly insulated filars to sufficiently minimise distal currents. Any breakages in these filars may compromise their ability to provide effective protection from RF heating. To demonstrate this, the simulations from section 6.1.5 were repeated but with the bare decoy having a 1 mm break at its center. The results are shown in figure 10.1. While

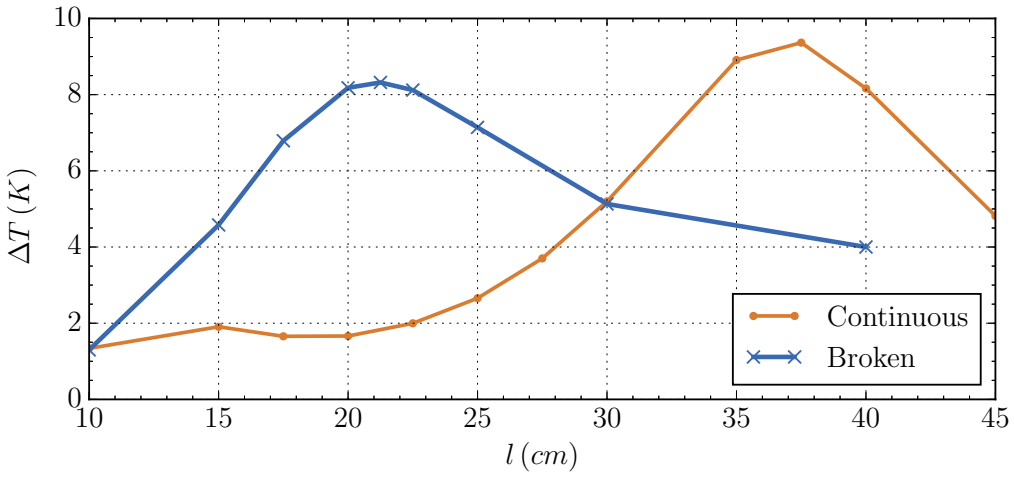

Figure 10.1: *Simulated distal heating for a lead with a* $0.9l$ *single decoy versus the same lead with a decoy having a* 1 mm *break in the middle of its length. Seemingly counterintuitive, the break can actually improve safety when the lead length is long!*

the break causes little change in the magnitude of peak heating, it clearly alters the expected profile of distal heating. The size, location, and number of decoy breakages, are expected to have further impact. Characterisation of these parameters are beyond the scope of this work. Nevertheless, measurement methods have been devised to detect filar breakage, and could be undertaken just prior to scanning a patient with MRI, to help guarantee predictable RF protection. The concepts are described below.

10.2 Concept 1: Continuity Tester

The proposed design incorporates an impedance/continuity (Z) meter within the impulse generator housing, to provide measurement of the DC impedance that exists between filar conductors. The result is then relayed to the MRI radiologist through a near-field wireless communications device, providing an assessment of the implant lead's decoy integrity. The simplest implementation is shown in figure 10.2a. In this arrangement, a Z meter is connected between the proximal ends of two individual decoys, with each distal end shorted to one another. A broken decoy would be indicated by a DC impedance exceeding

$$Z_{dc} = \frac{2\rho_d l_d}{\pi r_d^2} \tag{10.1}$$

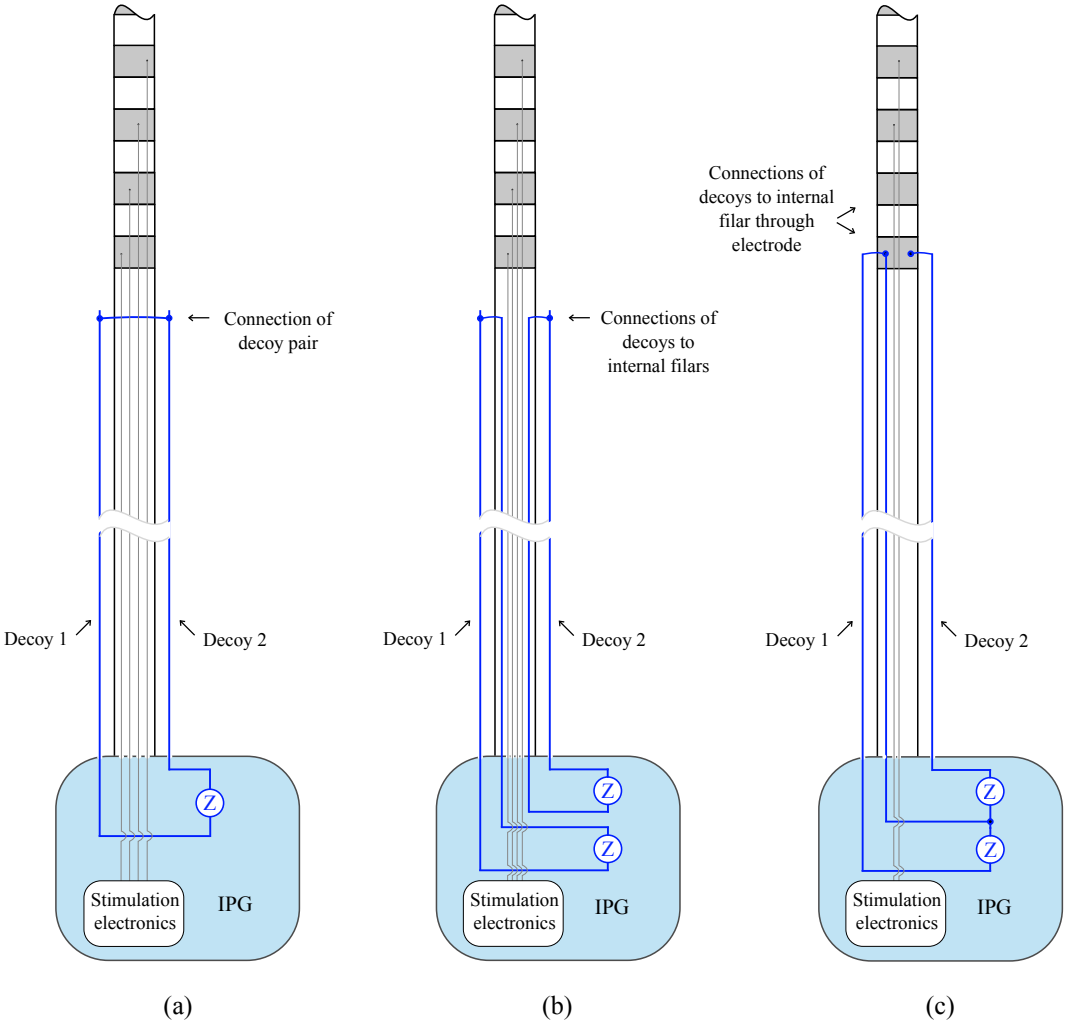

Figure 10.2: *Examples of different implementations for decoy breakage detection. The conductive paths under test are indicated by the blue lines. The Z meter is incorporated within the impulse generator (IPG) housing along with the electronics that administer neurostimulation.*

where ρ_d is the resistivity of the decoy metal, l_d is the length of one decoy, and r_d is radius of the decoy conductor. However, if any parasitic shorts were to exist between the decoy pair before the distal end, a breakage may go undetected.

An improved design is shown in figure 10.2b. In this arrangement, one or more Z meters are employed to measure the impedance between decoys and internal lead filars. The internal lead filars may be the same filars that are used for neurostimulation, or alternatively, additional filars dedicated for these tests.

A break in the decoy would be indicated by a DC impedance greater than

$$Z_{dc} = \frac{\rho_d l_d}{\pi r_d^2} + \frac{\rho_w l_w}{\pi r_w^2} \tag{10.2}$$

where ρ_w is the resistivity of the internal filar metal, and l_w and r_w are its length and radius, respectively.

For manufacturing reasons it may be more practical to form the necessary junctions between the decoys and internal filars through one or more electrodes as is shown in figure 10.2c. Similarly, equation 10.2 applies. If these electrodes are not intended for neurostimulus, a layer of insulation applied overtop may be preferable, especially if the decoys are incorporating Thinsulation.

10.3 Concept 2: RF Impedance Tester

As discussed in earlier chapters, the RF impedance that exists between the implant filars and surrounding tissue at the MRI frequency, has a direct influence on the level of distal heating produced during MRI. Therefore, through measurement of this parameter, the MRI safety of an implanted lead could be assessed while in situ, and potentially, evaluated against multiple MRI RF frequencies. This is important since the level of peak heating can vary with changes in the position, location, and configuration of the implanted device. It may also prove to be a useful technique in the lab, for quickly assessing the RF safety of prototype leads without the need for thermometry-based methods.

Figure 10.3 shows an example of how an RF impedance analyser[10] might be incorporated. Connections from the analyser are made to the metal housing of the impulse generator and to the lead filar which, *preferably*, extends to the most distal electrode where highest heating is expected to occur (refer to section 7.1.5). The RF impedance between these points can be evaluated and compared against the RF impedance of leads with known heating values. A prediction can then be made about the RF safety of the implanted device.

[10]Substitution of a TDR would offer a time-domain based approach following chapter 5.

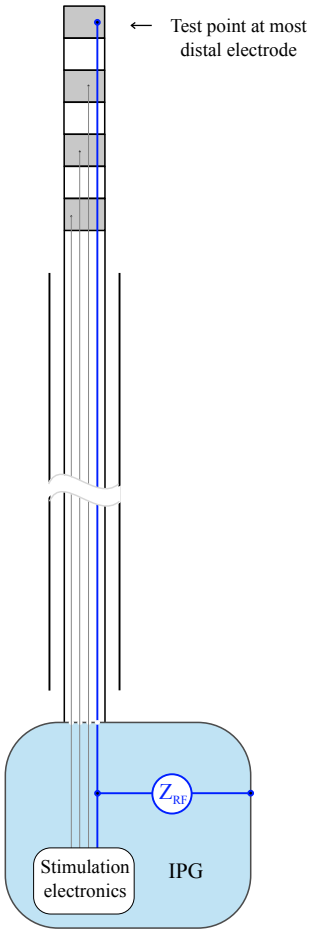

Figure 10.3: *Example of a testing scheme for predicting the RF safety of an implanted lead. An RF impedance analyser is connected between a filar and the impulse generator (IPG) housing. Decoys are shown, but the technique lends itself to implant leads of any type. Like with the continuity tester method, impedance measurements are relayed to the radiologist through a type of near-field communications method (not shown).*

Chapter 11

Conclusion

Neurostimulation devices have become increasingly common in recent years. Around 34,000 units for SCS are implanted in patients each year [83], more than double the amount reported previously at the time of [41]. Implants for DBS are also becoming more prevalent with a leading implant manufacturer reporting over 150,000 of their devices in service around the world today [84]. The vast majority of these implanted devices have MRI contraindications and unless surgically removed, prevent the patient from undergoing future MRI scans. Fortunately, manufacturers have recently started offering some options for SCS devices that have conditional compatibility with 1.5 T MRI [1], [2], but their use is limited and requires very restrictive scanning protocols and procedures to guarantee patient safety.

The main challenge in designing a neurostimulator that is MRI-safe is being able to mitigate the heating effect that can occur at the distal end of the electrode lead during scanning. Lead lengths of several hundred millimeters are necessary for transferring electrical stimulus from the bulky impulse generator to very localised neural regions via millimeter-sized distal electrodes. Such lengths make them susceptible to RF induction, with the distal electrodes providing a path for induced currents to escape and dissipate in concentrated regions of tissue. The most distal electrode contributes the highest level of heating with an SAR concentration virtually undetectable to the MRI machine.

While numerous strategies for mitigating this effect have been proposed in the literature, few have actually appeared in commercial products. Many require the addition of components with dimensions unsuitable for neurostimulator leads, or the incorporation of so much filar resistance that it would impair the normal operation of the implant. Others claim safety of their designs but give consideration to single lead lengths only.

This thesis introduced a variety of new techniques for ameliorating the RF hazard associated with implanted leads of arbitrary length, focusing on safety in 3 T MRI machines. The most noteworthy was the Decoy technique, which proved to be particularly effective at reducing distal heating through the addition of bare or thinly insulated auxiliary filars. The modification is simple and can be applied to already well-established lead designs. Application of surface roughening to the decoy filars may offer further improvement, by increasing the ability of the decoys to sink RF current into the surrounding tissue through the gain in apparent surface area.

Other methods use the principle of the skin effect to impede the flow of RF current in the stimulation filars. While only limited effectiveness is possible with filars formed from metals such as copper or platinum, slightly magnetic metals on the other hand may offer significantly higher RF-to-DC resistance ratios and eliminate distal heating. However, magnetic saturation and mechanical forces imposed by the MRI magnet may deter from the use of such materials. As such, in conjunction with this approach, it may be advantageous to increase the AC resistance of the filars through surface roughening, such that metals with only low magnetic permeabilities are necessary.

Leads incorporating thin insulation on the filars have also been shown to exhibit improved MRI safety. The thin dielectric layer helps shunt induced currents from the filars into the surrounding tissue, thus reducing the total stored energy in the filars and the amount of RF current delivered to the distal electrodes. Any adjacent filars with thicker insulation present a similar improvement thanks to mutual coupling and damping. Accordingly, lead designs with filars having a combination of both thin and thick insulation types can effectively mitigate RF heating.

Good design can greatly improve the MRI safety of an implant lead, even without implementing any of the above techniques. Simply increasing the number of distal electrodes and/or their dimensions will increase the total apparent surface area of the electrode metal at the distal end and diffuse heating more effectively. The incorporation of additional capacitance between electrodes may also improve the sharing of RF currents. Furthermore, selection of lead lengths that have the ability to support only weak resonance will help.

While the original objectives of this research have been met there exists a range of other areas that entail further investigation. These include:

1. What impacts do bends or loops have on the RF safety of the proposed lead designs?

2. How do the proposed lead designs perform at the RF frequency of a 1.5 T MRI machine? Can a lead be optimised to work safely in both 1.5 T and 3 T machine environments?

3. Resistance in the lead filars helps to impede the flow of induced currents. Would a resistive plating on the lead filars help to enhance the skin effect and hence maximise their RF-to-DC resistance ratio?

4. Can decoy filars offer better protection when in higher numbers, if their surfaces are roughened, if they are constructed from magnetic materials, or if they are electrically connected to the impulse generator housing? Would decoys having non-equal lengths or breaks in their lengths improve MRI safety?

5. Can the decoy filar be replaced by a small helical inductor with shorted ends, positioned adjacent to the lead filars? Its length needs only to be several centimeters long and could be accompanied by other inductors placed about the lead axis.

6. The distribution of RF currents flowing through implant lead filars is similar to that of a half-wave dipole antenna. Can the insulation thickness along the length of a lead and its filars be tapered or staggered in

such a way to maximise shunting of RF currents to the surrounding tissue?

7. MRI safety can be improved by simply insulating the distal electrodes with a thin plastic coating. Can a neurostimulator be designed to deliver sufficient stimulus to tissue through such electrodes?

8. Variations in the location and configuration of the implanted lead can have a considerable impact on peak RF heating. The depth of the implanted lead from the tissue surface is particularly influential. A lead which is MRI-safe in one implanted location may be unsafe in another. Can a simple impedance analyser be temporarily attached to the lead following surgical implantation or even built into the neurostimulator housing such that the MRI safety of an implanted lead can be checked and certified following implantation?

Overall, the manuscripts and various other work presented in this thesis have demonstrated that MRI-safe implant leads for neurostimulators are possible through simple techniques and design modifications. This work will allow patients fitted with these implants to undergo MRI scans in future, with great potential benefits to their long-term health.

Appendix A

Co-Authorship Forms

THE UNIVERSITY OF WAIKATO
Te Whare Wānanga o Waikato

Co-Authorship Form

Postgraduate Studies Office
Student and Academic Services Division
Wahanga Ratonga Matauranga Akonga
The University of Waikato
Private Bag 3105
Hamilton 3240, New Zealand
Phone +64 7 838 4439
Website: http://www.waikato.ac.nz/sasd/postgraduate/

This form is to accompany the submission of any PhD that contains research reported in published or unpublished co-authored work. **Please include one copy of this form for each co-authored work.** Completed forms should be included in your appendices for all the copies of your thesis submitted for examination and library deposit (including digital deposit).

Please indicate the chapter/section/pages of this thesis that are extracted from a co-authored work and give the title and publication details or details of submission of the co-authored work.

"Cause and Amelioration of MRI-Induced Heating Through Medical Implant Lead Wires"
Published in the Proceedings of the 21st Electronics New Zealand Conference (ENZCON 2014), Hamilton, 20-21 Nov. 2014, pp. 34–40

Nature of contribution by PhD candidate	Writing of manuscript, established EM model, performed data analysis, prepared figures and tables, developed ideas.
Extent of contribution by PhD candidate (%)	60

CO-AUTHORS

Name	Nature of Contribution
Jonathan Scott	Planning, assistance with theory, supervision, help with writing of ms.

Certification by Co-Authors

The undersigned hereby certify that:

- the above statement correctly reflects the nature and extent of the PhD candidate's contribution to this work, and the nature of the contribution of each of the co-authors; and

Name	Signature	Date
Jonathan Scott		25 Jun 2018
Steven McCabe		26 Jun 2018

THE UNIVERSITY OF WAIKATO
Te Whare Wānanga o Waikato

Co-Authorship Form

Postgraduate Studies Office
Student and Academic Services Division
Wahanga Ratonga Matauranga Akonga
The University of Waikato
Private Bag 3105
Hamilton 3240, New Zealand
Phone +64 7 838 4439
Website: http://www.waikato.ac.nz/sasd/postgraduate/

This form is to accompany the submission of any PhD that contains research reported in published or unpublished co-authored work. **Please include one copy of this form for each co-authored work.** Completed forms should be included in your appendices for all the copies of your thesis submitted for examination and library deposit (including digital deposit).

Please indicate the chapter/section/pages of this thesis that are extracted from a co-authored work and give the title and publication details or details of submission of the co-authored work.

"Electromagnetic Techniques to Minimize the Risk of Hazardous Local Heating around Medical Implant Electrodes during MRI Scanning"
Published in the Proceedings of the European Microwave Conference (EUMC 2015), Paris, 7--10 Sep. 2015, pp. 702--705.

Nature of contribution by PhD candidate	Writing of manuscript, performed measurements and data analysis, prepared figures and tables, developed ideas.
Extent of contribution by PhD candidate (%)	50

CO-AUTHORS

Name	Nature of Contribution
Jonathan Scott	**Planning & management, supervision, help with measurements & writing.**
Stephen Butler	MRI machine operator, assisted with measurements.

Certification by Co-Authors

The undersigned hereby certify that:

- the above statement correctly reflects the nature and extent of the PhD candidate's contribution to this work, and the nature of the contribution of each of the co-authors; and

Name	Signature	Date
Jonathan Scott		**25 Jun 2018**
Stephen Butler		26 JUN 2018
Steven McCabe		26 Jun 2018

THE UNIVERSITY OF WAIKATO
Te Whare Wānanga o Waikato

Co-Authorship Form

Postgraduate Studies Office
Student and Academic Services Division
Wahanga Ratonga Matauranga Akonga
The University of Waikato
Private Bag 3105
Hamilton 3240, New Zealand
Phone +64 7 838 4439
Website: http://www.waikato.ac.nz/sasd/postgraduate/

This form is to accompany the submission of any PhD that contains research reported in published or unpublished co-authored work. **Please include one copy of this form for each co-authored work.** Completed forms should be included in your appendices for all the copies of your thesis submitted for examination and library deposit (including digital deposit).

Please indicate the chapter/section/pages of this thesis that are extracted from a co-authored work and give the title and publication details or details of submission of the co-authored work.

"Technique to Assess the Compatibility of Medical Implants to the RF Field in MRI"
Published in the Proceedings of the Asia-Pacific Microwave Conference (APMC 2015). Nanjing, 6--9 Dec. 2015, pp. 1--3.

Nature of contribution by PhD candidate	Writing of manuscript, performed measurements and data analysis, prepared figures and tables, developed ideas.
Extent of contribution by PhD candidate (%)	60

CO-AUTHORS

Name	Nature of Contribution
Jonathan Scott	Planning, assistance with theory & measurements, supervision, help with writing of ms.

Certification by Co-Authors

The undersigned hereby certify that:

- the above statement correctly reflects the nature and extent of the PhD candidate's contribution to this work, and the nature of the contribution of each of the co-authors; and

Name	Signature	Date
Jonathan Scott		25 Jun 2018
Steven McCabe	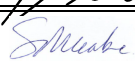	26 Jun 2018

THE UNIVERSITY OF WAIKATO
Te Whare Wānanga o Waikato

Co-Authorship Form

Postgraduate Studies Office
Student and Academic Services Division
Wahanga Ratonga Matauranga Akonga
The University of Waikato
Private Bag 3105
Hamilton 3240, New Zealand
Phone +64 7 838 4439
Website: http://www.waikato.ac.nz/sasd/postgraduate/

This form is to accompany the submission of any PhD that contains research reported in published or unpublished co-authored work. **Please include one copy of this form for each co-authored work.** Completed forms should be included in your appendices for all the copies of your thesis submitted for examination and library deposit (including digital deposit).

Please indicate the chapter/section/pages of this thesis that are extracted from a co-authored work and give the title and publication details or details of submission of the co-authored work.

"Measurement of Implant Electrode Leads using Time-Domain Reflectometry to Predict the Resonant Length for MRI Heating"
Published in the Proceedings of the 22nd Electronics New Zealand Conference (ENZCON 2016), Wellington, 17-18 Nov. 2016, pp. 90–94.

Nature of contribution by PhD candidate	Writing of manuscript, performed measurements and data analysis, prepared figures and tables, developed ideas.
Extent of contribution by PhD candidate (%)	70

CO-AUTHORS

Name	Nature of Contribution
Jonathan Scott	Planning, assistance with theory, supervision, help with writing of ms.

Certification by Co-Authors

The undersigned hereby certify that:

- the above statement correctly reflects the nature and extent of the PhD candidate's contribution to this work, and the nature of the contribution of each of the co-authors; and

Name	Signature	Date
Jonathan Scott	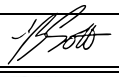	25 Jun 2018
Steven McCabe		26 Jun 2018

THE UNIVERSITY OF WAIKATO
Te Whare Wānanga o Waikato

Co-Authorship Form

Postgraduate Studies Office
Student and Academic Services Division
Wahanga Ratonga Matauranga Akonga
The University of Waikato
Private Bag 3105
Hamilton 3240, New Zealand
Phone +64 7 838 4439
Website: http://www.waikato.ac.nz/sasd/postgraduate/

This form is to accompany the submission of any PhD that contains research reported in published or unpublished co-authored work. **Please include one copy of this form for each co-authored work.** Completed forms should be included in your appendices for all the copies of your thesis submitted for examination and library deposit (including digital deposit).

Please indicate the chapter/section/pages of this thesis that are extracted from a co-authored work and give the title and publication details or details of submission of the co-authored work.

"New MRI-safe Implant Electrode Design"
Published in the Proceedings of the International Microwave Symposium (IMS 2016), San Francisco, 22--27 May. 2016, pp. 1–3.

Nature of contribution by PhD candidate	Writing of manuscript, performed measurements and data analysis, prepared figures and tables, developed ideas.
Extent of contribution by PhD candidate (%)	65

CO-AUTHORS

Name	Nature of Contribution
Jonathan Scott	Planning, assistance with theory, supervision, help with writing of ms.

Certification by Co-Authors

The undersigned hereby certify that:

- the above statement correctly reflects the nature and extent of the PhD candidate's contribution to this work, and the nature of the contribution of each of the co-authors; and

Name	Signature	Date
Jonathan Scott	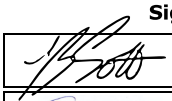	25 Jun 2018
Steven McCabe		26 Jun 2018

THE UNIVERSITY OF WAIKATO
Te Whare Wānanga o Waikato

Co-Authorship Form

Postgraduate Studies Office
Student and Academic Services Division
Wahanga Ratonga Matauranga Akonga
The University of Waikato
Private Bag 3105
Hamilton 3240, New Zealand
Phone +64 7 838 4439
Website: http://www.waikato.ac.nz/sasd/postgraduate/

This form is to accompany the submission of any PhD that contains research reported in published or unpublished co-authored work. **Please include one copy of this form for each co-authored work.** Completed forms should be included in your appendices for all the copies of your thesis submitted for examination and library deposit (including digital deposit).

Please indicate the chapter/section/pages of this thesis that are extracted from a co-authored work and give the title and publication details or details of submission of the co-authored work.

"A Novel Implant Electrode Design Safe in the RF Field of MRI Scanners"
Published in the IEEE Transactions on Microwave Theory and Techniques (MTT) Journal, vol.65, no.9, pp. 3541--3547, Sept. 2017.

Nature of contribution by PhD candidate	Writing of manuscript, performed measurements and data analysis, prepared figures and tables, developed ideas.
Extent of contribution by PhD candidate (%)	70

CO-AUTHORS

Name	Nature of Contribution
Jonathan Scott	Planning, assistance with theory, supervision, help with measurement & writing.

Certification by Co-Authors

The undersigned hereby certify that:

- the above statement correctly reflects the nature and extent of the PhD candidate's contribution to this work, and the nature of the contribution of each of the co-authors; and

Name	Signature	Date
Jonathan Scott		25 Jun 2018
Steven McCabe		26 Jun 2018

Appendix B

Equipment Datasheets

Excerpts from various datasheets are provided. Complete versions can be found online [62]–[64], [72].

GE Healthcare

Discovery™ MR750, a 3.0T system

Technical data

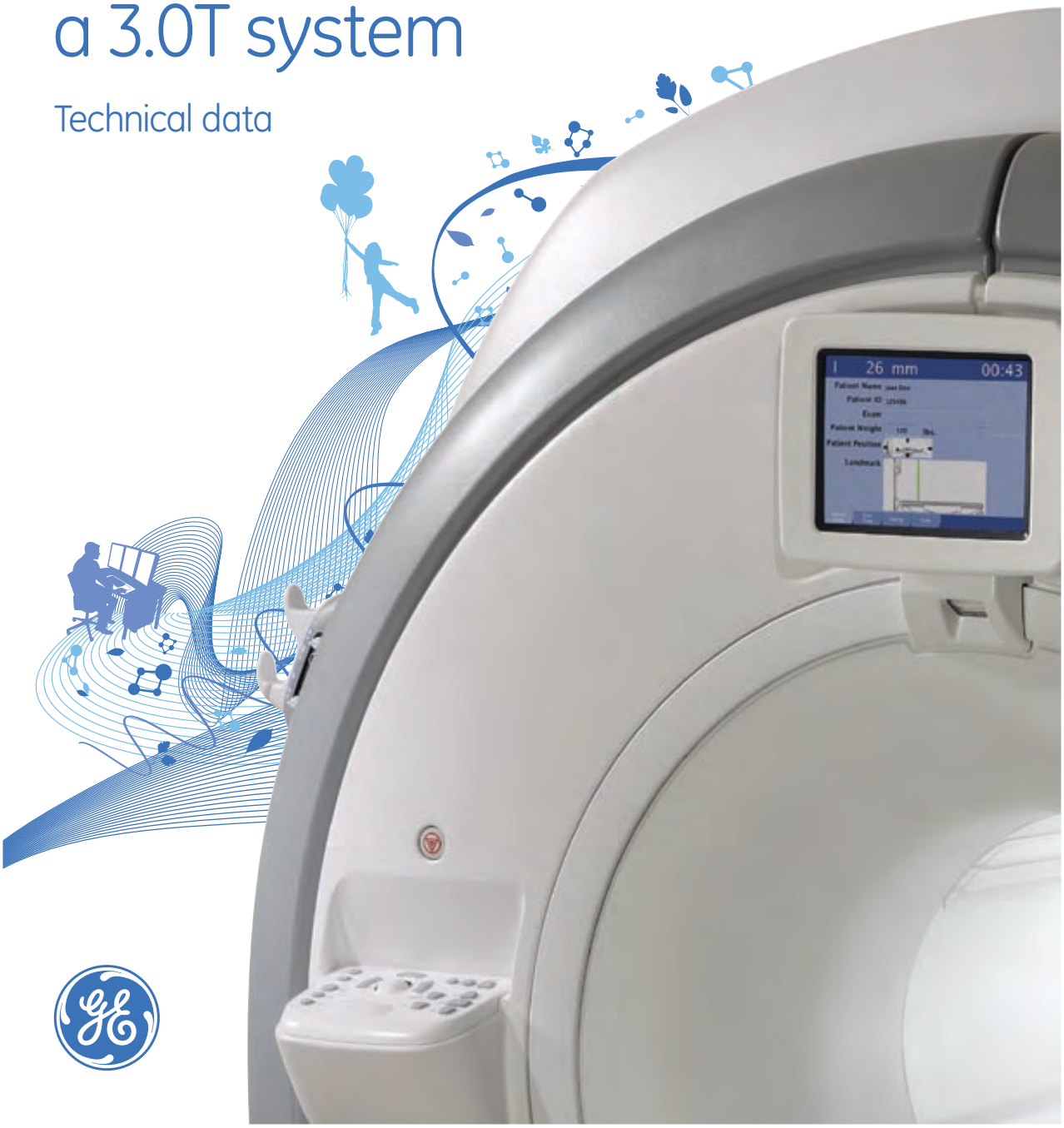

3.0T Magnet technology

The foundation for quality and flexibility

When it comes to image quality and applications flexibility, no other component of an MRI system has greater impact than the magnet architecture.

The Discovery™ MR750 3.0T MR system features GE's 3rd generation 3.0T magnet design, and features a high-homogeneity short-bore superconducting magnet for excellent image quality. The open appearance of the magnet helps ease patient anxiety while the zero-boil-off technology effectively eliminates helium refills, reducing operating costs and maximizing uptime.

Easy siting, affordable operation

The Discovery MR750 3.0T magnet is one of the most compact systems available. Complemented by GE's active shielding technology, the Discovery MR750 3.0T can be installed almost anywhere.

Magnet enclosures

This magnet enclosure system is designed to provide several benefits for the patient and technologist:

- Patient anxiety is eased, resulting in reduced exam time for uncooperative patients
- Technologists have easy access to the patient
- Dual-sided controls streamline patient setup

Patient bore	
Patient Bore (L x W x H)	70 cm x 60 cm x 60 cm
Patient positioning features	Laser alignment guides for patient positioning 32-channel configurations offer dual-sided table, landmarking and control panel
Patient comfort controls and interface	Head or feet first entry Dual-flared patient bore 2 way in-bore intercom system Adjustable in-bore lighting system Adjustable in-bore patient ventilation system
Other	In-room operator console with track ball control

Magnet specifications	
Operating field strength	3.0T (127.8 MHz)
Shim coils	18 superconducting
Magnet shielding	Active
EMI shielding factor	97%
Magnet size (without enclosures) (L x W)	<173 cm x 206 cm
Magnet length with enclosures	194 cm
Magnet weight with cryogens	9,750 kg
Long-term stability	< 0.1 ppm/hr over 24-hour period
Cryogen refill period	Zero-boil off*
Fringe field (axial x radial)	5 Gauss = 5.0 m x 2.8 m 1 Gauss = 7.4 m x 4.4 m
Manufacturer	GE Healthcare

*Under normal operating conditions

Fringe Field: 3.0T vs. 1.5T

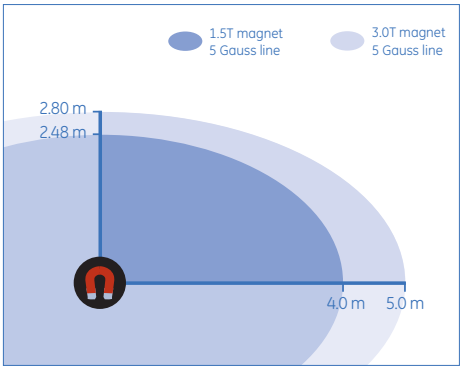

Magnet high-order shim

To fully optimize the magnet homogeneity for your facility, the Discovery™ MR750 3.0T system uses 18 superconducting high-order shim coils to ensure optimum performance for each site's unique environment.

High homogeneity is assured – our Discovery MR750 3.0T magnet provides excellent results for:

- Large FOV imaging up to 48 cm x 48 cm x 48 cm
- Off-center FOV imaging such as knee, shoulder and wrist imaging
- Robust fat saturation techniques required for abdominal, breast and musculoskeletal imaging
- High-performance applications, such as cardiac, fMRI, diffusion tensor and spectroscopy

GE measures the raw homogeneity of a magnet using the Volume Root Mean Square (V-RMS) method that utilizes both measured data on a sphere plus synthesized data using a spherical harmonic expansion of the field.

Diameter of spherical volume-DSV	Typical ppm	Guaranteed ppm
10 cm	0.03	
20 cm	0.05	<0.05
30 cm	0.1	<0.15
40 cm	0.25	<0.50

Volume Root-Mean-Square (V-RMS) method is based on 24 measurements in each of 24 planes with linear terms set to zero.

In addition, GE utilizes a Large Volume RMS (LV-RMS) procedure to determine the field homogeneity after integrating the gradients, RF body coil, and system electronics. LV-RMS measurements utilize a large phantom placed within the bore, and because the data is obtained using the entire imaging chain, it reflects the results that clinicians and researchers will experience with day-to-day scanning.

Diameter of spherical volume-DSV	Typical ppm
10 cm	0.02
20 cm	0.03
30 cm	0.08
40 cm	0.27
45 cm	0.53

Large Volume Root-Mean-Square (LV-RMS) method is an imaging-based method with over 173,000 measurements collected over a spherical volume after linear and higher order shims have been adjusted.

Gradient technology

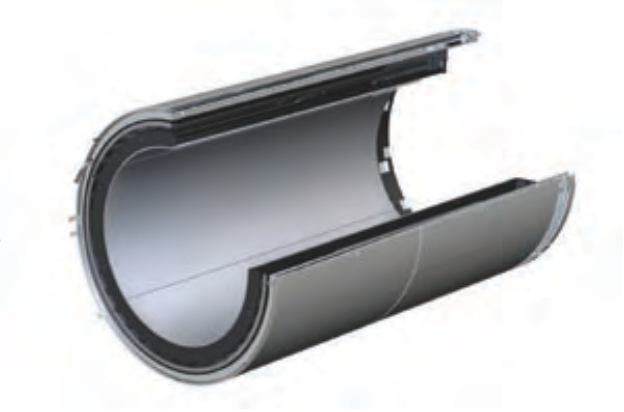

Gradient performance

Premium clinical and research performance is assured with the Discovery™ MR750 3.0T eXtreme gradient Resonance Module (XRM) and eXtreme Gradient Driver (XGD) systems. Gradient speed, accuracy and reproducibility are critical for all acquisitions, but the performance is especially critical in challenging acquisitions and research development.

The gradients are non-resonant and actively shielded to minimize eddy currents. The gradient coil and the RF body coil are integrated into a single module, which are both water- and air-cooled for maximum duty-cycle performance and patient comfort.

Amplitude per axis	50 mT/m
Slew rate per axis	200 T/m/s
Maximum effective amplitude	87 mT/m
Maximum effective slew rate	346 T/m/s
Maximum FOV on X, Y, Z axis	48 cm
Rise time to maximum amplitude	250 µs
Gradient duty cycle	100%

Quiet technology

State-of-the-art clinical imaging demands the routine use of ultra-fast imaging techniques. At 3.0T, the strong gradients interact with the magnetic field to create mechanical forces resulting in acoustic noise. GE's enhanced quiet technology takes a passive approach by employing an acoustic barrier material that reduces acoustic noise without compromising performance. This technology reduces acoustic noise levels by up to 50% when compared with previous designs.

Resistive high-order shim

The Discovery MR750 3.0T gradient is available with five high-order shims to minimize the effect of patient-induced magnet inhomogeneity. In addition to the three linear terms (X, Y, Z), this set includes the five 2nd-order terms (listed below) to shim the field to account for each patient's anatomy and position in the bore.

Higher-order shimming results in improved image quality for all applications, but especially in Spectroscopy, Diffusion Tensor (DT) and Diffusion-Weighted Echo Planar Imaging (DW-EPI), Fat Saturation, VIBRANT breast and MR Echo cardiac applications.

Linear and 2nd-order shim terms	X, Y, Z XY, ZX, ZY, Z^2 $X^2 - Y^2$

Fidelity, accuracy, and reproducibility

Gradient systems have historically been defined in terms of peak amplitude (mT/m) and slew rate of the generated field (T/m/s). While these parameters are important in achieving high temporal resolution parameters, such as TRs and TEs, applications such as fMRI, PROPELLER 2.0, TRICKS, and spectroscopy rely more heavily on gradient fidelity, accuracy, and reproducibility.

Fidelity is defined as the degree to which an electronics system accurately and reproducibly amplifies an input signal. Applied to MR gradient systems, gradient fidelity refers to the system's ability to generate requested waveforms. The high fidelity of the Discovery MR750 3.0T gradients is achieved through the use of innovative design of the digital control architecture within the gradient amplifier. This architecture has two digital control paths.

- Dedicated active feedback loop to regulate current errors.
- Unique feed-forward model to match amplifier output to gradient coil.

Gradient subsystem fidelity, accuracy, and reproducibility parameters	
Gradient integral precision*	0.47ppmFS-s
Shot-to-shot repeatability*	0.16ppmFS-s
Symmetry*	0.32ppmFS-s

* Typical gradient fidelity expressed in a relative scale is derived from the following measurements of integrated errors in micro-Amperes-second (µAs). Gradient integral precision is the maximum integrated current error over a full-scale, echo-planar gradient waveform. Shot-to-shot repeatability is the largest difference between integrated errors across waveforms. Symmetry is the largest difference in integrated current error when comparing positive and negative gradient waveforms.

Gradient system optimization

PERFORM 2.0 incorporates a new proprietary gradient waveform algorithm that manages limitations due to peripheral nerve stimulation (PNS) and therefore enables full use of slew rate for shorter TEs and TRs.

RF technology

The RF technology of the Discovery™ MR750 3.0T system integrates the three major components of the information pipeline: (1) Transmit, (2) Receive and (3) Processing. This close integration enables excellent clinical performance and image quality, especially for data-intensive applications.

RF transmit technology

The RF transmit architecture technology consists of a liquid-cooled 35kW solid-state RF power amplifier combined with an integrated, bandpass, 16-rung quadrature body coil designed to improve RF and signal homogeneity at 3.0T.

RF system optimization

At 3.0T, staying within FDA- and IEEC-mandated guidelines for Specific Absorption Rate (SAR) can potentially limit the ability to scan efficiently.

Leveraging over a dozen years' 3.0T experience, GE has overcome these limitations on the Discovery MR750 with an exclusive new synergistic SAR management system called PERFORM 2.0. Combining RF body coil design, optimized pulse sequences, detailed predictive SAR modeling during prescription, and real-time SAR feedback and correction during scanning helps ensure high system performance across all applications, tailored for each patient.

The results include fast exams, productivity, patient comfort and improved diagnostic results, scan after scan, patient after patient.

Standard RF transmit architecture	
RF amplifier	Water cooled, small footprint
Maximum output power	35 kW Body 4.5 kW Head
Maximum RF field with integrated body coil	>24 μT
Transmit gain	40 dB coarse/>84 dB instantaneous
RF exciter frequency range	127.72 ± 0.625 MHz
Frequency resolution	<0.6 Hz/step
Frequency stability	14 part per billion (0 to 50C)
Phase resolution	0.005 degree/step
Amplitude control	16 bit with 12.5 ns resolution
Amplitude stability	< 0.1 dB over one min. at rated power
Digital RF pulse control	2 amplitude modulators, 2 frequency/phase modulators
Continuous wave power	100W
RF Coil Transmit drive ports	4 ports
Transmit/Receive Body Coil	Fully integrated 16-rung quadrature birdcage bandpass 60 cm inner diameter Up to 48 cm FOV All anatomy and general applications

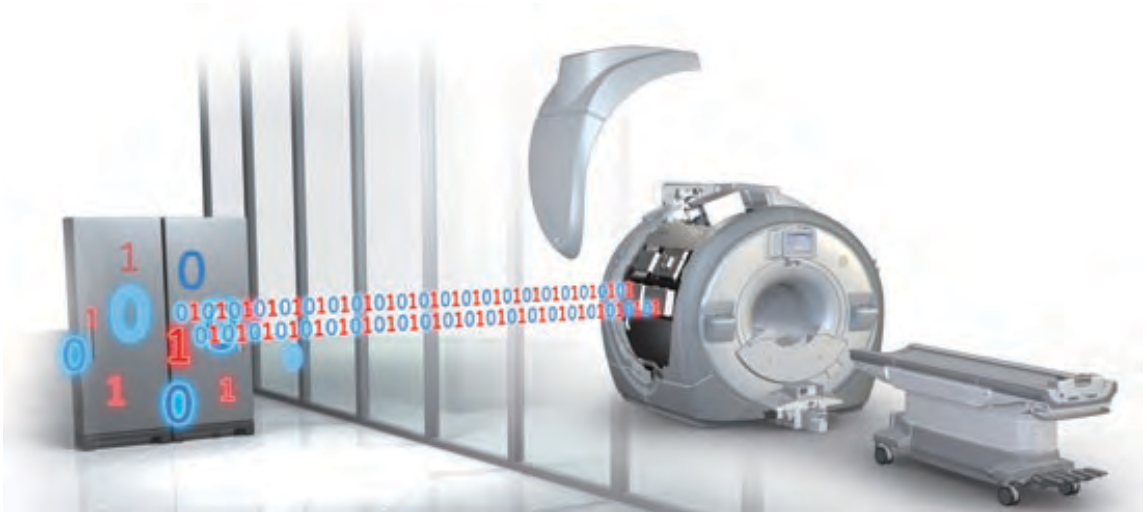

OpTix (Optical RF Receive technology)

The OpTix RF system enables high-bandwidth, 16- or 32-channel reception with improved SNR over conventional MR receiver designs. Conventional MR scanner designs place the RF receivers in the electronics room where the MR signal is subject to significant electrical noise prior to being digitized. The OpTix optical RF receivers are located on the magnet system inside the shielded scan room, completely isolated from external noise sources. The MR signal is digitized within the scan room and then optically transmitted to the reconstruction engine in the electronics room. Since losses are inherent with conventional wire designs, the close proximity of the receivers to the patient reduces noise and improves image quality.

Optical RF architecture	
Simultaneous RF receivers	16 or 32
Coil input ports	40 or 136
Quadrature demodulation	Digital
Receiver sampling frequency per channel	80 MHz
Receiver dynamic range at 1Hz BW	>165 dB
Receiver resolution	Up to 32 bits

The OpTix acquisition technology enables high image quality especially for data-intensive (3D) applications. When combined with GE's use of high-density surface coils, the optical receive chain is a critical path for ensuring clear signal reception and data analysis. To ensure that the high-density approach will always be maintained, the scalable Discovery™ MR750 3.0T architecture is designed to expand to 128 channels of simultaneous data acquisition in the future.

Reconstruction processing

Reconstruction performance today is challenged by explosive growth in data, and increased computational complexity. The amount of data to be stored and processed continues to increase with the advances in MR system technology. The Discovery MR750 meets that challenge head-on with innovations in reconstruction to take full advantage of computing power by leveraging both software and hardware technology.

The Discovery MR750 3.0T features a powerful volume reconstruction engine (VRE 2.0) that enables real-time image generation, even when massive parallel-imaging datasets are involved. The reconstruction engine features onboard memory and local raw data storage to support and maintain simultaneous data acquisition and reconstruction under the most demanding applications.

VRE 2.0 uses 64-bit computing, delivering larger acquisition memory and faster performance. Parallel processing and dedicated network cards provide scalable memory and throughput. The acquisition-to-disk feature automatically expands the memory capacity per the demands of the application.

Reconstruction engine - 16 channels configuration	
Peak 2D FFT/second (256 x 256 full FOV)	2700 2D FFTs/second (256 x 256 full FOV)
CPU	Two Dual Core AMD Opteron 2218 CPUs (four 2.6 GHz cores)
Memory	16 GB ECC DDR2 667 RAM
Hard disk storage	2 x 73 Gbytes

Reconstruction engine - 32 channels configuration	
Peak 2D FFT/second (256 x 256 full FOV)	5400 2D FFTs/second (256 x 256 full FOV)
CPU	Four Dual Core AMD Opteron 2218 CPUs (eight 2.6 GHz cores)
Memory	32 GB ECC DDR2 667 RAM
Hard disk storage	4 x 73 Gbytes

RF coils and arrays

High-density arrays that focus coil elements around the anatomy of interest, while providing extended coverage where needed, help to ensure optimal image quality for every procedure. The open and flexible RF architecture of the Discovery™ 3.0T MR750 system also facilitates access to coils developed by other vendors. These attributes lead to the optimal coil for each clinical application and a system that is ready for coils in the future.

Standard coils with each MR system

Transmit/Receive Body Coil

- Fully integrated
- 16-rung quadrature birdcage bandpass
- 60 cm inner diameter
- Up to 48 cm FOV
- All anatomy and general applications

Transmit/Receive Head Coil

- 16-rung quadrature birdcage
- Patient-friendly, split-top design
- 28 cm diameter x 38 cm length
- Head and brain
- Extremities
- Pediatric imaging

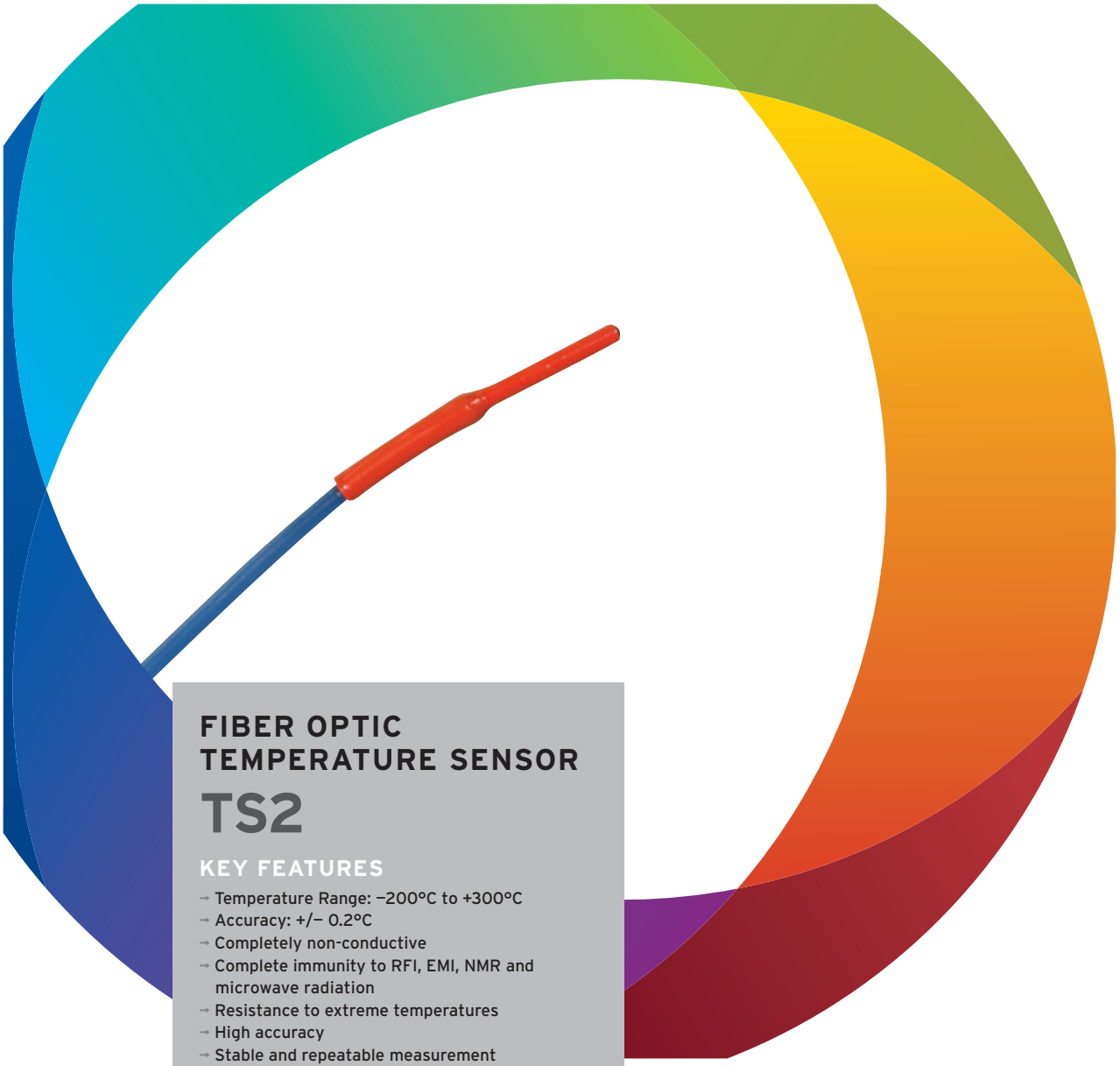

FIBER OPTIC TEMPERATURE SENSOR

TS2

KEY FEATURES

- Temperature Range: −200°C to +300°C
- Accuracy: +/− 0.2°C
- Completely non-conductive
- Complete immunity to RFI, EMI, NMR and microwave radiation
- Resistance to extreme temperatures
- High accuracy
- Stable and repeatable measurement
- GaAs-based temperature sensor

APPLICATIONS

- High voltage distribution powerlines, e.g. electric trains
- Gas translated power breakers
- Power bars, bus-bars

OPTOCON®
OPTICAL SENSORS AND SYSTEMS

FIBER OPTIC TEMPERATURE SENSOR
TS2

DESCRIPTION

The fiber optic temperature probe TS2 was designed for a wide range of applications, especially for the use inside of generators, power transformers as well as bus bars, R&D and industrial applications and offers complete immunity to RFI, EMI, NMR and microwave radiation – the best choice for all challenges.

The standard temperature sensor TS2 has a response time of 2s. With an accuracy of +/-0.2°C it allows precise and repeatable measurements. The coating of TS2 temperature sensor is made of PTFE, the fiber tip has a diameter of 1.0mm and has a serial ST-connector. For mechanical stability and applications e.g. in oil special protective coatings and hoses are available.

The fiber optic probe TS2 consists of a PTFE protected glass fiber and a GaAs-crystal (Galliumarsenid) at the sensor tip.

It is totally free of metal and immune to RFI, EMI, NMR and microwave radiation – therefore TS2 probes are explicit suitable for the use in high temperature ranges (-200°C to +300°C) as well as in aggressive and rough test environments.

All fiber optical temperature sensors can be connected to the fiber optic temperature measurement devices (FOTEMP), delivers accurate and complete reliable, stable and repeatable values. Starting at a light wave length of 850nm GaAs becomes optical translucent. Since the position of the band gap is temperature dependent, it shifts about 0.4nm/Kelvin.

The sensor cable can be up to several meters and kilometers long without influencing the accuracy of the measurement result. Other sensor lengths and connector types are available upon request.

We are always anxious to adjust our offer to your special needs. In case of any further questions about individual measurement problems, lengths of sensors or connector types, please contact us.

TECHNICAL SPECIFICATIONS

Name of sensor	TS2, The comprehensive
Temperature range	– 200°C to + 300°C
Accuracy	+/– 0.2°C
Response time	≤ 2,0s
Fiber Ø	200µm

Sensor length	2m standard (Other lengths on customer request)
Connector type	ST
Signal conditioner	Compatible with all Optocon AG fiber optic thermometers

DIMENSIONS

All dimensions in mm.

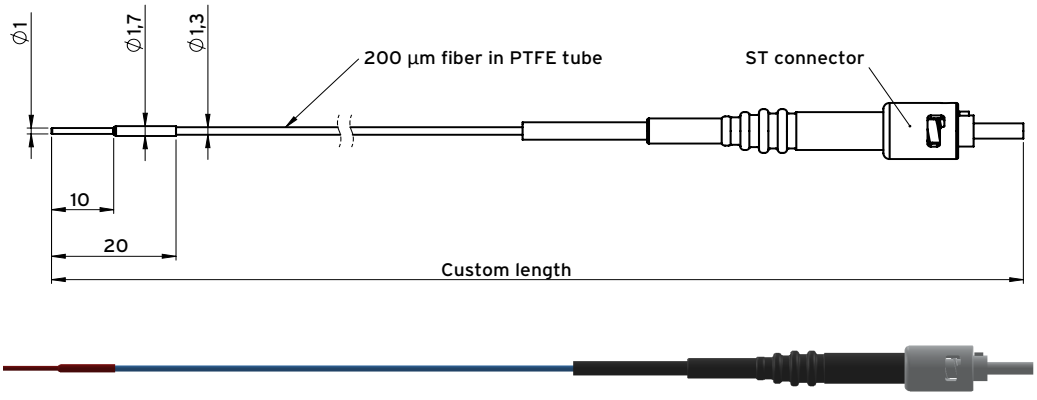

OPTOCON®
OPTICAL SENSORS AND SYSTEMS

OPTOCON AG
OPTICAL SENSORS AND SYSTEMS

POHLANDSTRASSE 17
D-01309 DRESDEN

PHONE +49 351 3101957
FAX +49 351 3111951

INFO@OPTOCON.DE
WWW.OPTOCON.DE

FIBER OPTIC THERMOMETER
FOTEMP1-4

KEY FEATURES

- Modern design
- 1-4 measuring channels
- 1-4 relay outputs freely assignable to any channel
- Temperature display in °C, F or K
- Integrated fold out stand
- Measuring range: −200°C to +300°C
- Standard deviation*: +/−0.2°C
- Large 7,1cm (2,8") LCD-TFT color display
- Easy and intuitive user interface
- Quick and easy temperature measurement
- Choice between 0-10V or 4-20mA analog output
- Status LED

APPLICATIONS

- EMI, RFI and microwave environments
- High voltage environments
- Harsh and hazardous environments
- Nuclear environments
- Aerospace applications
- Process monitoring
- Medical applications (MRT)

OPTOCON®
OPTICAL SENSORS AND SYSTEMS

FIBER OPTIC THERMOMETER
FOTEMP1-4

DESCRIPTION

The new fiber-optic thermometer FOTEMP1-4 combines innovative design with user-friendly functionality. The modern design makes the temperature measurement even easier and offers complete immunity to RFI, EMI, NMR and microwave radiation.

The FOTEMP1-4 has an innovative appearance: It has a larger screen and a modern keyboard which makes the data acquisition and control of the device even easier. The user-friendly display supports high-precision measurements, while the color LCD display offers excellent readout of the measurement values even in low light conditions. The menu supports two languages, German and English. With its compact design, it fits perfectly into any environments. Various interfaces, analog and relay outputs make the device very versatile. The extensive software "FOTEMP Assistant" allows a detailed evaluation via PC with direct export of data to a spreadsheet application.

The FOTEMP1-4 has a measuring range from -200°C to +300°C. It measures with a standard deviation* of ±0.2°C. The fiber optic thermometer offers complete immunity to RFI, EMI and microwave radiation, making it ideal for environments where the use of conventional temperature measuring instruments is excluded due to extreme conditions. It is compatible with all our fiber optic temperature sensors and is ideal for any applications in the laboratory and in industry.

The outer jacket of the fiber optic temperature sensors is made out of teflon, at the sensor tip a GaAs crystal (gallium arsenide) is attached. The probe sensor is completely non-conductive. Optocon's fiber optic sensors offer complete immunity to RF and microwave radiation with high temperature operating capability, intrinsic safety, and non-invasive use. The probes are also designed to withstand harsh and corrosive environments.

Starting at a light wave length of 850nm GaAs becomes optical translucent. Since the position of the band gap is temperature dependent, it shifts about 0.4nm/Kelvin. The measurement device contains a light source and a device for the spectral detection of the band gap. This guaranties fast, repeatable and reproducible measurements.

Over the entire life of the system calibration is not required to remain within the specifications.

DIMENSIONS

FRONT VIEW

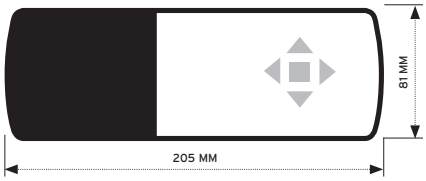

BACK VIEW

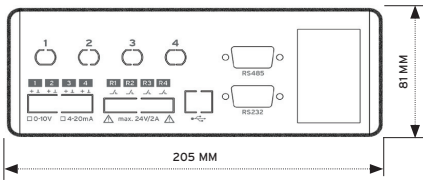

TECHNICAL SPECIFICATONS

Number of channels	1-4
Power supply	100-240VAC / 50-60Hz
Power consumption	> 10VA
Measuring range	– 200 °C to + 300 °C
Standard deviation*	+/– 0.2 °C
Resolution	0,1 °C
Measuring time/ Channel**	250ms
Analog output	0-10V or 4–20mA
Interface	RS-232 or RS-485 or USB
Relay output	4
Datalogging	Log sequenz via Software
Display	7,1cm (2,8") LCD-TFT color display
Connector type	ST
Form factor	IP50
Storage temperature	-20°C to +70°C
Operating temperature	-20°C to +60°C
Weight	1,2 kg
Dimensions	205 x 267 x 81 mm
Material	ABS/PC in RAL9003
Software	e.g. FOTEMP Assistant 2 or ASCII-Protocol-Description
Data export	Via interfaces
Warranty	2 years
Probes	All fiber optic temperature probes from Optocon AG can be connected.

*The "expanded uncertainty of measurement" is the product of the reported standard deviation and the coverage factor k=2. It corresponds to a normal distribution to a coverage probability of approximately 95%.

**Mean value. This value depends on the used sensor and its enviromental temperature.

OPTOCON®
OPTICAL SENSORS AND SYSTEMS

OPTOCON AG
OPTICAL SENSORS AND SYSTEMS

WASHINGTONSTR. 16/16A
01139 DRESDEN, GERMANY

PHONE +493518435990
FAX +49 351843599111

INFO@OPTOCON.DE
WWW.OPTOCON.DE

Coaxial

High Power Amplifier

LZY-22+

50Ω 30W 0.1 to 200 MHz

The Big Deal

- High Power Output, 30W typ., from 100 KHz to 200 MHz
- Digitally controlled blanking, isolation 70 dB typ.
- Designed to withstand open or short output load at full rated power

LZY-22+

LZY-22X+

Product Overview

This ruggedized High Power Amplifier is capable of delivering 30W output signals across its entire operating bandwidth, from 0.1-200 MHz. Extensive safety features to prevent amplifier damage include over-temperature protection and the ability to handle short and open loads. The LZY-22+, including heat-sink and cooling fan, is designed for a 24V/5.5A DC power supply.

Key Features

Feature	Advantages
30 W Output Power @ 3 dB compression across 0.1-200 MHz bandwidth	High power output across broad frequency range supports a wide array of applications, from avionics, broadcasting, medical, and high-power lab testing to marine band, public safety, and aircraft communications
High Gain, 43 dB typ.	High, consistent gain across entire operating range (flatness ±1.36 dB) for predictable performance and signal level strength
Blanking Isolation 70dB	Manual or TTL-controlled signal blanking (OFF 0.4 ms; ON 64 ms)
Internal open/short Protection Circuitry	Antenna mismatches or damaged output cables will not cause amplifier damage
Overheat Protection	Automatic shutdown at baseplate temperature of +85 ± 5°C prevents thermal runaway, even during remote, unmonitored operation in difficult thermal environments. Whenever shutdown is triggered, a TTL output is provided for automated system control.
Unconditionally Stable	No risk of damage to other components from impedance mismatch or internal oscillations

Coaxial

High Power Amplifier

LZY-22+

50Ω 30W 0.1 to 200 MHz

Features

- Saturated Output Power, 30 W typ.
- High Gain, 43 dB typ.
- Excellent IP3, +52 dBm typ.
- Blanking isolation, 70 dB typ.
- Unconditionally stable
- Overheat-protection automatic shuts off when base plate temperature exceeds 85±5°C

Applications

- Avionics
- Broadcast radio and TV
- Medical-MRI
- Lab Use - High Power Test

Model No.	LZY-22+	LZY-22X+▲
Case Style	BT1598	
Connectors	SMA Female	
Price (Qty.)	$1495.00 ea. (1-9)	$1470.00 ea. (1-9)

+RoHS Compliant

The +Suffix identifies RoHS Compliance. See our web site for RoHS Compliance methodologies and qualifications

Electrical Specifications[1] at 25°C

Parameter	Frequency (MHz)	LZY-22+ LZY-22X+▲ Min	Typ.	Max.	Units
Frequency Range		0.1	—	200	MHz
Gain	0.1 - 200	40	43	—	dB
Gain Flatness			±1.36	±1.6	dB
Output Power at 1dB compression	0.1	40	42	—	dBm
	100	40	42	—	
	200	40	41.5	—	
Saturated Output Power at 3dB compression (Pin=8 dBm)	0.1	42	44	—	dBm
	100	44	45	—	
	200	44	45	—	
Noise Figure	10 - 200	—	8.9	10	dB
Output third order intercept point[2]	0.1 - 200	—	+52	—	dBm
Input VSWR	0.1 - 200	—	1.4	2.0	:1
Output VSWR	0.1 - 200	—	4.0	—	:1
Blanking Isolation	0.1 - 50	—	60	—	dB
	50 - 200	—	70	—	
DC Supply Voltage	0.1 - 200		24	25	V
Supply Current[3]	0.1 - 200	—	5.3	6.0	A

1. All specifications are for a single input CW signal. At nominal output load, 24V nominal supply voltage.
2. 2 Tones, 0.5W/tone, 1MHz spacing
3. Addition of heat sink and fan to the LZY-22+ results in 0.2A additional current.

▲ Heat sink and fan not included. Alternative heat sinking and heat removal must be provided by the user to limit maximum base-plate temperature to 50°C, in order to ensure proper performance. For reference, this requires thermal resistance of user's external heat sink to be 0.08°C/W max.

Outline Drawing

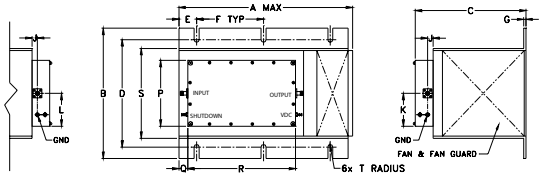

MOUNTING INFORMATION FOR MODELS WITHOUT HEATSINK.

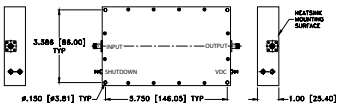

Outline Dimensions (inch / mm)

A	B	C	D	E	F	G	J	K	L	P	Q	R	S	T	wt
9.85	7.3	6.3	6.00	.98	3.75	.13	.31	1.84	1.84	3.68	.5	6.05	5.1	.135	grams*
250.19	185.42	160.02	152.40	24.89	95.25	3.30	7.87	46.74	46.74	93.47	12.70	153.67	129.54	3.43	4185

*500 grams without heatsink

Maximum Ratings

Parameter	Ratings
Operating Temperature	-10°C to 50°C
Storage Temperature	-30°C to 100°C
Base Plate Temperature	50°C
Input RF Power (no damage)	20 dBm
DC Supply Voltage	30V

Permanent damage may occur if any of these limits are exceeded.

Blanking Shutdown / Turn On	Min.	Typ.	Max.	Units
ON Voltage	0	—	0.8	V
OFF Voltage	4	—	5	V
Shutdown (90 to 10%)	—	0.4	—	ms
Turn ON (10 to 90%)	—	64	—	ms

Notes

A. Performance and quality attributes and conditions not expressly stated in this specification document are intended to be excluded and do not form a part of this specification document.
B. Electrical specifications and performance data contained in this specification document are based on Mini-Circuit's applicable established test performance criteria and measurement instructions.
C. The parts covered by this specification document are subject to Mini-Circuits standard limited warranty and terms and conditions (collectively, "Standard Terms"); Purchasers of this part are entitled to the rights and benefits contained therein. For a full statement of the Standard Terms and the exclusive rights and remedies thereunder, please visit Mini-Circuits' website at www.minicircuits.com/MCLStore/terms.jsp

Typical Performance Data/Curves at 24V **LZY-22+**

FREQUENCY (MHz)	GAIN (dB)	DIRECTIVITY (dB)	VSWR (:1)		ISOLATION (dB)	NOISE FIGURE (dB)	POUT at 1 dB COMPR. (dBm)	OUTPUT IP3 (dBm)
			IN	OUT				
0.10	45.61	22.22	1.26	3.36	64.0	--	41.93	53.37
0.70	45.30	21.72	1.20	3.72	62.6	--	42.38	55.84
1.00	45.34	21.74	1.21	3.72	62.5	--	42.45	55.89
2.00	45.28	22.68	1.20	3.71	62.5	--	42.47	55.96
5.00	45.06	25.54	1.20	3.75	63.6	--	42.55	56.00
10.00	44.81	23.79	1.21	3.80	66.7	8.78	42.36	56.03
30.00	44.37	24.74	1.33	3.58	70.2	8.31	43.21	55.23
50.00	43.78	25.79	1.38	3.05	72.3	8.07	43.25	53.09
70.00	44.40	24.81	1.37	1.91	72.5	8.26	42.41	51.20
90.00	44.59	24.14	1.31	1.22	70.8	8.33	41.60	50.17
100.00	44.73	24.08	1.28	1.05	69.9	8.31	41.98	50.22
120.00	44.36	25.25	1.22	1.56	69.2	8.18	43.38	51.61
160.00	44.20	26.43	1.07	1.81	75.2	8.18	43.96	52.27
180.00	44.32	26.07	1.08	1.55	79.0	8.27	42.83	51.66
200.00	43.86	28.10	1.10	1.33	82.5	8.30	41.39	50.36

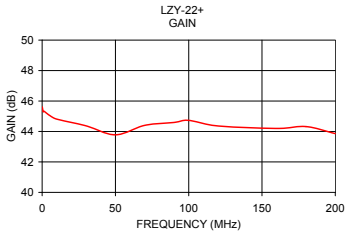

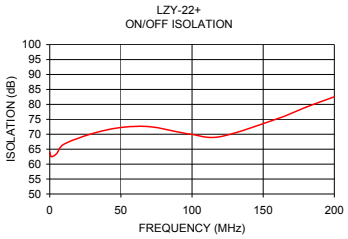

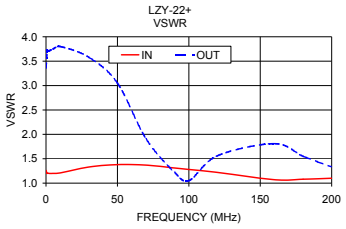

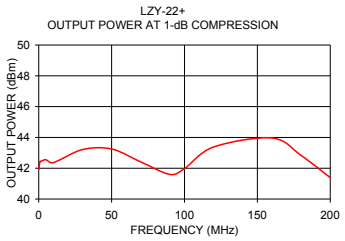

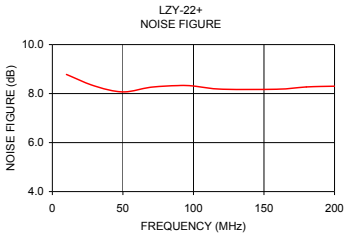

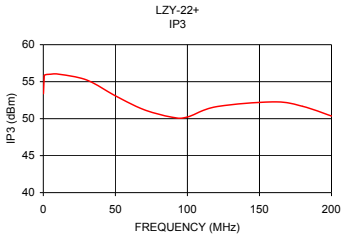

Notes
A. Performance and quality attributes and conditions not expressly stated in this specification document are intended to be excluded and do not form a part of this specification document.
B. Electrical specifications and performance data contained in this specification document are based on Mini-Circuit's applicable established test performance criteria and measurement instructions.
C. The parts covered by this specification document are subject to Mini-Circuits standard limited warranty and terms and conditions (collectively, "Standard Terms"); Purchasers of this part are entitled to the rights and benefits contained therein. For a full statement of the Standard Terms and the exclusive rights and remedies thereunder, please visit Mini-Circuits' website at www.minicircuits.com/MCLStore/terms.jsp

References

[1] "MRI SureScan pacing system: step-by-step instructions for a successful MRI scan," Physicians manual, Medtronic, 2014, http://www.medtronic.com/mrisurescan-us/pdf/MRI-Scanning-Protocol.pdf retrieved June 2018.

[2] "ImageReady MRI full body guidelines for Precision Montage MRI spinal cord stimulator system," Physicians manual, Boston Scientific, 2016, http://www.bostonscientific.com/content/dam/Manuals/us/current-rev-en/91035972-02_RevA_ImageReady_MRI_Full_Body_Guidelines_for_Precision_Montage_MRI_Spinal_Cord_Stimulator_System_MRI_en-US_S.pdf, retrieved June 2018.

[3] S. O. McCabe and J. B. Scott, "Implant conductor assembly with improved radio frequency properties," International patent for Decoy Filars *WO 2017/086805 A1*, May 2017. https://patents.google.com/patent/WO2017086805A1/en?oq=WO+2017%2f086805+A1 retrieved June 2018.

[4] S. O. McCabe and J. B. Scott, "A surgical implant conductor with increased radio frequency alternating current resistance," International patent for Roughened Filars *WO 2016/195513 A1*, Dec. 2016. https://patents.google.com/patent/WO2016195513A1/en?oq=WO+2016%2f195513+A1 retrieved June 2018.

[5] "Medtronic deep brain stimulation (DBS): the road to the 100,000th implant," Poster, Medtronic, Inc. 2012. http://multimediacapsule.thomsonone.com/file/download/1616/RelatedDocuments/673

retrieved Sept. 2014.

[6] J. A. Nyenhuis, P. Sung-Min, R. Kamondetdacha, A. Amjad, F. G. Shellock, and A. R. Rezai, "MRI and implanted medical devices: basic interactions with an emphasis on heating," *IEEE Trans. Device and Mater. Rel.*, vol. 5, no. 3, pp. 467–480, Sept. 2005.

[7] J. M. Olsen, S. L. Bolea, G. A. Hrdlicka, C. D. Wahlstrand, and T. B. Hoegh, "Lead electrode for use in an MRI-safe implantable medical device," International patent number *WO 2006/093685 A1*, Sept. 2006.

[8] "ICNIRP statement on: medical magnetic resonance (MR) procedures: protection of patients," International Commission on Non-Ionizing Radiation Protection (ICNIRP), *Health Phys.*, vol. 87, no. 2, pp. 197–216, Aug. 2004.

[9] L. M. Angelone, J. Ahveninen, J. W. Belliveau and G. Bonmassar, "Analysis of the role of lead resistivity in specific absorption rate for deep brain stimulator leads at 3T MRI", *IEEE Trans. Med. Imag.*, vol. 29, no. 4, pp. 1029–1038, Apr. 2010.

[10] "MRIsafety.com, your information resource for MRI safety, bioeffects, & patient management," `http://www.mrisafety.com/` retrieved May 2018.

[11] C. D. Wahlstrand and T. B. Hoegh, "Electrode for use in an MRI-safe implantable medical device," European patent number *EP 1 742 701 B1*, Aug. 2010.

[12] C. D. Wahlstrand, G. A. Hrdlicka, R. M. Skime, P. Przybszewski, and T. E. Cross, "Energy shunt for producing an MRI-safe implantable medical device," International patent number *WO 2005/030322 A1*, Apr. 2005.

[13] B. A. Tranchina, "Method for fabricating a stimulation lead to reduce MRI heating," US patent number *8,601,672 B2*, Dec. 2013.

[14] G. Bonmassar and E. Eskandar, "MRI compatible leads for a deep brain stimulation system," International patent number *WO2014055737 A1*,

Apr. 2014.

[15] C. D. Wahlstrand, R. M. Skime, G. A. Hrdlicka, J. M. Olsen, and S. L. Bolea, "MRI-safe implantable medical device," US patent number *8,620,453 B2*, Dec. 2013.

[16] *MRI and SCS, SureScan system* Medtronic, USA, Implant Manual, 2013. `http://www.mrisurescan.com/au/for-radiologists/spinal-cord-stimulators/mri-and-scs/index.htm#tab2` retrieved Aug. 2014.

[17] T. B. Hoegh, S. L. Bolea, C. D. Wahlstrand, G. A. Hrdlicka, and J. M. Olsen, "Lead electrode for use in an MRI-safe implantable medical device," European patent number *EP 1 740 260 B1*, Aug. 2010.

[18] O. Talcoth, T. Rylander, "Electromagnetic modeling of pacemaker lead heating during MRI", Technical Report, Chalmers University of Technology, Sweden, 2011.

[19] *F2182-11a standard test method for measurement of radio frequency induced heating on or near passive implants during magnetic resonance imaging,* ASTM International, West Conshohocken, PA, USA, 2010.

[20] R. K. Shevgaonkar, *Electromagnetic waves*, Tata McGraw-Hill, pp. 175, 2006.

[21] J. E. Brown, "Radiofrequency heating near medical devices in magnetic resonance imaging", PhD dissertation, Univ. of Florida, May 2012.

[22] S. Ramo, J. R. Whinnery, and T. Van Duzer, *Fields and waves in communication electronics, second edition*, John Wiley & Sons, Inc, pp. 147–150, 1984.

[23] D. W. Knight, "Practical continuous functions for the internal impedance of solid cylindrical conductors", Apr. 2013.

[24] R. W. P. King and G. S. Smith, *Antennas in matter: fundamentals, the-*

ory, and applications, The MIT Press, Cambridge, MA, 1981.

[25] S. A. Mohsin, N. M. Sheikh, and U. Saeed, "MRI induced heating of deep brain stimulation leads: effect of the air-tissue interface", Progress in Electromagnetics Research, PIER 83 pp. 81–91, 2008.

[26] "Hepatic Tumor Ablation", Comsol multiphysics model example, model ID: 497. `http://www.comsol.com/model/hepatic-tumor-ablation-497` retrieved Sept. 2014.

[27] N. Gallagher, C. E. Fear, I. A. Byrd, and E. J. Vigmond, "Contact geometry affects lesion formation in radio-frequency cardiac catheter ablation", PLOS ONE Journal, vol. 8, no. 9, pp. 1–10, Sept. 2013.

[28] "Modeling a dipole antenna", Comsol multiphysics model example, model ID: 8715. `http://www.comsol.com/model/modeling-a-dipole-antenna-8715` retrieved Sept. 2014.

[29] P. Serano, L. M. Angelone, H. Katnani, E. Eskandar, and G. Bonmassar, "A novel brain stimulation technology provides compatibility with MRI," Sci Rep, vol. 5, pp. 1–10, Apr. 2015.

[30] C. Jiang, X. Mo, J. Ding, Y. Dong, F. Zhang, H. Hao, and L. Li, "Deep brain stimulation lead design to reduce radio frequency heating in MRI", *Electronics Letters*, vol. 50, no. 25, pp. 1898–1900, Dec. 2014.

[31] B. Stevenson, W. Dabney and C. Frysz, "Issues and design solutions associated with performing MRI scans on patients with active implantable medical devices", *29th Annual International Conference of the IEEE Engineering in Medicine and Biology Society*, Aug. 2007, pp. 6166–6169.

[32] A. R. Rezai, D. Finelli, J. A. Nyenhuis, G. Hrdlicka, J. A. Tkach, A. Sharan, P. Rugieri, P. H. Stypulkowski, and F. G. Shellock, "Neurostimulation systems for deep brain stimulation: in vitro evaluation of magnetic resonance imaging-related heating at 1.5 Tesla," *J. Magn. Resonance Imaging*, pp. 241–250, 2002.

[33] C. Chou, J. A. McDougall, and K. W. Chan, "RF heating of implanted spinal fusion stimulator during magnetic resonance imaging," *IEEE Transactions on Biomedical Engineering*, vol. 44, no. 5, pp. 367–373, May 1997.

[34] K. R. Gorny, M. F. Presti, S. J. Goerss, S. C. Hwang, D. Jang, I. Kim, H. Min, Y. Shu, C. P. Favazza, K. H. Lee, and M. A. Bernstein, "Measurements of RF heating during 3.0-T MRI of a pig implanted with deep brain stimulator," *Magn. Reson. Imag.*, vol. 31, no. 5, pp. 783–788, June 2013.

[35] Y. Liu, J. Chen, F. G. Shellock, and W. Kainz, "Computational and experimental studies of an orthopedic implant: MRI-related heating at 1.5T/64MHz and 3T/128MHz," *Journal of Magnetic Resonance Imaging*, pp. 1–7 2012.

[36] P. A. Bottomley, A. Kumar, W. A. Edelstein, J. M. Allen, and P. V. Karmarkar, "Designing passive MRI-safe implantable conducting leads with electrodes," *Med. Phys.*, vol. 37, no. 7, pp. 3828–3843, June 2010.

[37] E. Mattei, G. Calcagnini, F. Censi, M. Triventi and P. Bartolini, "Numerical model for estimating RF-induced heating on a pacemaker implant during MRI: experimental validation", IEEE Transactions on Biomedical Engineering, vol. 57, no. 8, pp. 2045–2052, Aug. 2010.

[38] S. Feng, R. Qiang, W. Kainz, and J. Chen, "A technique to evaluate MRI-induced electric fields at the ends of practical implanted lead," *IEEE Transactions on Microwave Theory and Techniques*, vol. 63, no. 1, pp. 305–313, Jan. 2015.

[39] F. G. Shellock and A. J. Audet-Griffin, "Evaluation of magnetic resonance imaging issues for a wirelessly powered lead used for epidural, spinal cord stimulation," *International Neuromodulation Society*, pp. 1–6, 2013.

[40] R. Caverly, G. Breed, W. Cantrell, M. Eron, J. Garcia, N. Kondrath, D. Myer, M. Ruiz, and J. Walker, "Advancements at the lower end: advances in HF, VHF, and UHF systems and technology," *IEEE Microw.*

Mag., vol. 16, no. 1, pp. 28–49, Feb. 2015.

[41] S. McCabe and J. Scott, "Cause and amelioration of MRI-induced heating through medical implant lead wires," *Proceedings of the 21st Electronics New Zealand Conference*, Hamilton, 20-21 Nov. 2014, pp. 34–40.

[42] J. B. Scott and S. O. McCabe, "Implant conductor with improved radio frequency properties", New Zealand provisional patent for Roughened Filars *708633*, Filed on May 29, 2015.

[43] Y. Seo and Z. J. Wang, "MRI scanner-independent specific absorption rate measurements using diffusion coefficients," *Journal of Applied Clinical Medical Physics.*, pp. 224–229, 2017.

[44] D. Qian, A. M. El-Sharkawy, P. Bottomley, and W. A. Edelstein, "An RF dosimeter for independent SAR measurement in MRI scanners," *Medical Physics*, vol. 40 no. 12, pp. 1–11, Dec. 2013.

[45] P. Bottomley, "Turning up the heat on MRI," *Journal of the American College of Radiology*, pp. 1–4, July 2008.

[46] "Criteria for significant risk investigations of magnetic resonance diagnostic devices", *United States Food and Drug Administration (FDA)*, 2014.

[47] "Medical electrical equipment - Part 2-33: particular requirements for the basic safety and essential performance of magnetic resonance equipment for medical diagnosis", International standard, *International Electrotechnical Commission (IEC)*, IEC 60601-2-33:2010, 2010.

[48] "Freedom spinal cord stimulator (SCS) system", *United States Food and Drug Administration (FDA)* test data, 2014, `https://www.accessdata.fda.gov/cdrh_docs/pdf14/K141399.pdf` retrieved May 2018.

[49] Y. Shlepnev, "Modeling frequency-dependent conductor losses and dispersion in serial data channel interconnects," *Simberian Inc.*, pp. 1–12, 2007.

[50] G. Gold and K. Helmreich, "A physical surface roughness model and its applications," *IEEE Trans. Microw. Theory Techn*, vol. 65, no. 10, pp. 3720–3732, Oct. 2017.

[51] P. G. Huray, O. Oluwafemi, J. Loyer, E. Bogatin, and X. Ye, "Impact of copper surface texture on loss: a model that works," *DesignCon 2010 proceedings*, Santa Clara, CA, 2010. retrieved May 2018. `http://www.oldfriend.url.tw/article/IEEE_paper/roughness/5_TA2_Paul_Huray.pdf`

[52] "Abrasive grinding paper," Datasheet, Pace Technologies, USA. retrieved May 2018. `http://www.metallographic.com/Brochures/SiCpaper.pdf`

[53] M. H. Azarian, D. Kwon, and M. Pecht, "Use of the skin effect for detection of interconnect degradation," *International Symposium on Microelectronics*, Jan. 2009, pp. 1–5.

[54] "Chemically roughened solid silver: a simple, robust and broadband SERS substrate," S. Wijesuriya, K. Burugapalli, R. Mackay, G. Chukwuebuka Ajaezi, and W. Balachandran, *Sensors*, vol. 16, no. 10, pp. 1–20, Oct. 2016.

[55] "Gold etching," Application notes, MicroChemicals, Germany, 2013. retrieved June 2018. `https://www.microchemicals.eu/technical_information/gold_etching.pdf`

[56] J. M. Otten, "Method for reducing the polarization of bioelectrical stimulation leads using surface enhancement, and product made thereby," US patent number *5,326,448*, July 1994.

[57] J. Weibler, "Properties of metals used for RF shielding," *EMC Test & Design*, pp. 1–5, Dec. 1993.

[58] S. Seshadri and J. Scott, "Enhancing skin-effect using surface roughening and its potential to reduce RF heating from implant leads," *Proceedings of the 23rd Electronics New Zealand Conference*, Christchurch, 4–6 Dec.

2017, pp. 1–6.

[59] S. M. Gygax, "Surface roughening of platinum wire: an electrochemical and mechanical approach," M. Eng. thesis, The University of Waikato, 2017.

[60] S. McCabe, J. Scott, and S. Butler, "Electromagnetic techniques to minimize the risk of hazardous local heating around medical implant electrodes during MRI scanning," *European Microwave Conference*, Paris, 7–10 Sept. 2015, pp. 702–705.

[61] J. Thomas Vaughan and J. R. Griffiths, *RF coils for MRI*, John Wiley & Sons, Inc, 2012.

[62] "Fiber optic temperature sensor, TS2", Technical datasheet, Optocon, 2012, `http://www.optocon.de/en/products/fiber-optic-temperature-sensors/ts2/`, retrieved May 2018.

[63] "Fiber optic thermometer, FOTEMP 1-4", Technical datasheet, Optocon, 2015, `http://www.optocon.de/en/products/fiber-optic-temperature-signal-conditioners/fotemp1-4-fiber-optic-single-channel-thermometer/`, retrieved May 2018.

[64] "High power amplifier, LZY-22+", Technical datasheet, Mini-Circuits, `http://https://www.minicircuits.com/pdfs/LZY-22+.pdf`, retrieved May 2018.

[65] S. McCabe and J. Scott, "New MRI-safe implant electrode design," *International Microwave Symposium*, San Francisco, 22–27 May 2016, pp. 1–3.

[66] S. O. McCabe and J. B. Scott, "Implant conductor assembly with improved radio frequency properties," New Zealand provisional patent for Decoy Filars *714212*, Filed on Nov. 16, 2015.

[67] S. McCabe and J. Scott, "Technique to assess the compatibility of medical

implants to the RF field in MRI," *Asia-Pacific Microwave Conference*. Nanjing, 6–9 Dec. 2015, pp. 1–3.

[68] A. T. Mobashsher and A. M. Abbosh, "Artificial human phantoms: human proxy in testing microwave apparatuses that have electromagnetic interaction with the human body", IEEE Microwave Magazine, vol. 16, no. 6, pp. 42–62, July 2015.

[69] S. O. McCabe, "Impulse TDR and its application to characterisation of antennas", MPhil thesis, The University of Waikato, 2011.

[70] S. O. McCabe, "Implantable electrode structures and their RF effects in MRI machines", PhD thesis, The University of Waikato, 2019.

[71] St. Jude Medical, "Percutaneous leads for SCS", `http://professional.sjm.com/products/neuro/scs/percutaneous-leads/percutaneous-leads-for-scs`, retrieved Nov. 2015.

[72] "GE Healthcare Discovery MR750, a 3.0T system", Technical datasheet, General Electric Company, MR-0347-06.09-EN-US, 2009.

[73] R. H. Caverly, "MRI fundamentals," *IEEE Microw. Mag.*, vol. 16, no. 6, pp. 20–33, July 2015.

[74] S. McCabe and J. Scott, "Measurement of implant electrode leads using time-domain reflectometry to predict the resonant length for MRI heating," *Proceedings of the 22nd Electronics New Zealand Conference*, Wellington, 17-18 Nov. 2016, pp. 90–94.

[75] T. B. Hoegh, S. L. Bolea, C. D. Wahlstrand, G. A. Hrdlicka, and J. M. Olsen, "Lead electrode for use in an MRI-safe implantable medical device," US patent number *US 8,364,286 B2*, Jan. 2013.

[76] C. D. Smith, A. V. Kildshev, J. A. Nyenhuis, and K. S. Foster, "Interactions of magnetic resonance imaging radio frequency magnetic fields with elongated medical implants," *J. Appl. Phys.*, vol. 87, no. 9, pp. 6188–6190, May 2000.

[77] E. Cabot, T. Lloyd, A. Christ, W. Kainz, M. Douglas, G. Stenzel, S. Wedan, and N. Kuster, "Evaluation of the RF heating of a generic deep brain stimulator exposed in 1.5T magnetic resonance scanners," *Bioelectromagnetics*, vol. 34, no. 2, pp. 104–113, Feb. 2013.

[78] J. E. Brown and C. S. Lee, "Radiofrequency resonance heating near medical devices in magnetic resonance imaging," *Microw. Opt. Technol. Lett.*, vol. 55, no. 2, pp. 299–302, Feb. 2013.

[79] K. B. Baker, J. A. Tkach, J. A. Nyenhuis, M. Phillips, F. G. Shellock, J. Gonzalez-Martinez, and A. R. Rezai, "Evaluation of specific absorption rate as a dosimeter of MRI-related implant heating," *J. Magn. Resonance Imaging*, pp. 315–320, Aug. 2004.

[80] *Assessment of the safety of magnetic resonance imaging for patients with an active implantable medical device*, Technical specification ISO/TS 10974, 2012.

[81] S. McCabe and J. Scott, "A novel implant electrode design safe in the RF field of MRI scanners," *IEEE Trans. Microw. Theory Techn*, vol. 65, no. 9, pp. 3541–3547, Sept. 2017.

[82] F. S. Fernandez, M. A. Vega, A. A. Ramos, F. F. Gonzalez, and B. L. Aragoneses, "Lead fractures in deep brain stimulation during long-term follow-up," *Parkinsons Disease*, vol. 2010, no. 409356, pp. 1–4, 2010.

[83] S. Thomson, "Spinal cord stimulation," International Neuromodulation Society, T-SCS 11.16, Nov. 2016. `http://www.neuromodulation.com/spinal-cord-stimulation`, retrieved June 2018.

[84] "Medtronic SureTune3 receives health Canada licence for deep brain stimulation therapy," Press release, Medtronic, June 2017. `http://newsroom.medtronic.com/phoenix.zhtml?c=251324&p=RssLanding&cat=news&id=2279215`, retrieved June 2018.